

# **Time-resolved emission spectra of intrinsic Tyrosine during the early stages of $\beta$ -amyloid aggregation**

Abeer Ahmed M. Alghamdi

A thesis presented in partial fulfilment of the requirements  
for the degree of Doctor of Philosophy



Department of Physics, Photophysics Research Group  
University of Strathclyde, Glasgow, UK

**September 2021**

‘This Thesis is the result of the author’s original research. It has been composed by the author and has not been previously submitted for examination which has led to the award of a degree.’

‘The copyright of this Thesis belongs to the author under the terms of the United Kingdom Copyright Acts as qualified by University of Strathclyde Regulation 3.50. Due acknowledgment must always be made of the use of any material contained in, or derived from, this Thesis.’

Signed:

Date:

## **Acknowledgments**

I would like to thank my supervisor Dr. Olaf Rolinski for his guidance, support and patience throughout this project. Also, I greatly appreciate my second supervisor, Professor David Birch for his great feedback, encouragement and guidance.

I would like to thank Princess Nourah University, not only for granting me a PhD scholarship, but for their keenness to keep in touch and provide moral support and guidance.

I am also grateful to my colleagues and all members of the Photophysics group, for all have helped me in many ways throughout the course of my study

I also express my deepest gratitude to my family and friends for their unfailing support and continuous encouragement.

## Abstract

The aggregation of beta-amyloids ( $A\beta$ ) is one of the key processes responsible for the development of Alzheimer's disease (AD). Early molecular-level detection of beta-amyloid oligomers may help in early diagnosis and in the development of new intervention therapies. Previous studies on the changes in beta-amyloid's single tyrosine intrinsic fluorescence response during aggregation can be efficiently used to indicate the extent of the aggregation at its earliest stages before the beta-sheets are formed. To better understand the underlying kinetics of  $A\beta$  aggregation we present a complementary approach based on the time-resolved emission spectra (TRES) of amyloid's tyrosine. TRES can sufficiently demonstrate structural changes on the nanosecond time scale after excitation.  $A\beta$  monomers can be distinguished from oligomers by means of the position of their emission spectra. Further spectral shift caused by dielectric relaxation can be useful for determining the size of the oligomers since their spectral shift gradually decreases as the aggregates grow larger.

$A\beta_{1-40}$  self-assembly was also studied in the presence of additional compounds affecting the progress of aggregation such as copper ions and glucose or factors that can potentially prevent aggregation like quercetin. In the presence of copper ions, time-resolved fluorescence techniques demonstrated the formation of beta amyloid-copper complexes and the accelerated peptide aggregation. The shifts in the emission spectral peaks indicated that the peptides exhibit different aggregation pathways than in the absence of copper. In the presence of high glucose concentrations TRES exhibit multiple peaks, their position and shifts reveal the impact of glycation on  $A\beta_{1-40}$  oligomerisation. The results show that formation of the advanced glycation end products (AGEs) alters the aggregation pathway. These changes are highly relevant to our understanding of the pathophysiology of AD and the implication of AGE and diabetes in these pathways. In the presence of quercetin, TRES exhibit multiple peaks with

characteristic spectral shifts, indicating a different aggregation pathway. At a molar ratio of 1:1 ( $A\beta_{1-40}$  : Quercetin), TRES results showed early formation of  $A\beta$ -Quercetin complexes, which seem to inhibit further  $A\beta$  aggregation. This makes it a potential nutrient that may help prevent or delay the development of Alzheimer's disease.

Other techniques like fluorescence anisotropy decay and nanoparticle tracking analysis (NTA) were investigated in order to study  $A\beta$  aggregation and to explore synergy resulting from combining different experimental techniques.

## Publications

A. Alghamdi, V. Vyshemirsky, D. J. Birch & O. J. Rolinski, "Detecting beta-amyloid aggregation from time-resolved emission spectra", *Methods and applications in fluorescence*, 2018, 6(2), 024002.

A. Alghamdi, T. Wellbrock, D. J. Birch, V. Vyshemirsky & O. J. Rolinski, "Cu<sup>2+</sup> effects on beta-amyloid oligomerisation monitored by fluorescence of intrinsic tyrosine", *ChemPhysChem*, 2019, 20(23), 3181-3185.

A. Alghamdi, S. Forbes, D. J. Birch, V. Vyshemirsky & O. J. Rolinski, "Detecting beta-amyloid glycation by intrinsic fluorescence-Understanding the link between diabetes and Alzheimer's disease" *Archives of Biochemistry and Biophysics*, 2021, 704, 108886.

A. Alghamdi, L. H. C. Chung & O. J. Rolinski, "Monitoring the Assembly and Aggregation of Polypeptide Materials by Time-Resolved Emission Spectra" In *Polypeptide Materials*, Humana, New York, NY, 2021, 167-177.

## Conference proceedings

A. Alghamdi, D. J. S. Birch, V. Vyshemirsky, O. J. Rolinski, "Dielectric relaxation detection of beta-amyloid aggregation", Poster Presentation: Fluorofest, Glasgow, UK, 24-26th April 2017

A. Alghamdi, D. J. S. Birch, V. Vyshemirsky, O. J. Rolinski, "Determining beta-amyloid aggregation from the time-resolved emission spectra", Poster Presentation: 7th EuCheMS Chemistry Congress, Liverpool, UK, 26-30th August 2018

## List of Abbreviations

<b>A<math>\beta</math><sub>1-11</sub></b>	11 amino acid long $\beta$ -amyloid peptide variant
<b>A<math>\beta</math><sub>1-16</sub></b>	16 amino acid long $\beta$ -amyloid peptide variant
<b>AD</b>	Alzheimer's disease
<b>AFM</b>	Atomic force microscopy
<b>AGE</b>	Advanced glycation end products
<b>Ala</b>	Alanine
<b>ANS</b>	1-anilino-8-naphthalenesulfonate
<b>APP</b>	Amyloid precursor protein
<b>Asp</b>	Aspartic acid
<b>A<math>\beta</math></b>	$\beta$ -Amyloid peptide
<b>A<math>\beta</math><sub>1-40</sub></b>	40 amino acid long $\beta$ -amyloid peptide variant
<b>A<math>\beta</math><sub>1-42</sub></b>	42 amino acid long $\beta$ -amyloid peptide variant
<b>Bis-ANS</b>	4,4'-dianilino-1,1'-binaphthyl-5,5'-disulfonic acid dipotassium salt
<b>CD</b>	Circular dichroism technique
<b>CSF</b>	Cerebrospinal fluid
<b>Cu<sup>2+</sup></b>	Copper ion
<b>DLS</b>	Dynamic light scattering
<b>EM</b>	Electron microscopy
<b>FCS</b>	Fluorescence correlation spectroscopy
<b>FRET</b>	Fluorescence resonance energy transfer
<b>FTIR</b>	Fourier transform infrared spectroscopy
<b>HEPES</b>	N-2-hydroxyethylpiperazine-N'-2-ethanesulfonic acid
<b>HFIP</b>	1,1,1,3,3,3- Hexafluoro-2-Propanol

<b>His</b>	Histidine
<b>LED</b>	Light-emitting diode
<b>MAPK</b>	Mitogen-activated protein kinases
<b>MCA</b>	Multichannel analyser
<b>NAYA</b>	N-Acetyltyrosinamide
<b>NDD</b>	Neurodegenerative disease
<b>NMR</b>	Nuclear magnetic resonance spectroscopy
<b>NTA</b>	Nano tracking analysis
<b>p3</b>	peptide resulting from the $\alpha$ - and $\gamma$ -secretase cleavage from the amyloid precursor protein
<b>PBS</b>	Phosphate-Buffered Saline
<b>PD</b>	Parkinson's disease
<b>Phe</b>	Phenylalanine
<b>PMT</b>	Photomultiplier tube
<b>RET</b>	Resonance energy transfer
<b>sAPP<math>\alpha</math></b>	soluble (or secreted) amyloid precursor protein- $\alpha$
<b>sAPP<math>\beta</math></b>	soluble (or secreted) amyloid precursor protein- $\beta$
<b>SPAD</b>	Single photon avalanche diode
<b>TAC</b>	Time to amplitude converter
<b>TCSPC</b>	Time-correlated single-photon counting
<b>TEM</b>	Transmission electron microscopy,
<b>ThT</b>	Thioflavin T
<b>TRES</b>	Time resolved emission spectra
<b>Tyr</b>	Tyrosine

# Table of Contents

Acknowledgements .....	ii
Abstract .....	iii
Publications .....	v
Conference proceedings .....	v
List of abbreviations .....	vi
<b>1. Introduction</b>	<b>1</b>
<b>2. Amyloidosis</b>	<b>8</b>
2.1. Introduction .....	8
2.2. The Beta-amyloid protein and the amyloid hypothesis .....	11
2.2.1. Alzheimer's disease .....	11
2.2.2. Beta-amyloid formation.....	13
2.2.3. Beta-amyloid aggregation.....	14
2.2.4. Methods for analysis of beta-amyloid aggregation.....	14
<b>3. Fluorescence</b>	<b>19</b>
3.1. Fluorescence theory.....	19
3.2. Characteristics of fluorescence emission.....	26
3.2.1. Stokes shift.....	26
3.2.2. Fluorescence quantum yield.....	28
3.2.3. Fluorescence lifetime .....	28
3.2.4. Fluorescence quenching.....	30
3.2.5. Anisotropy.....	34
3.3. Intrinsic protein fluorophores.....	37
3.4. Complexity of intrinsic fluorescence kinetics.....	38
<b>4. Steady-state and time-resolved fluorescence measurements</b>	<b>41</b>
4.1. Steady-state measurements.....	41
4.2. Time-resolved fluorescence measurements.....	43
4.2.1. The time-correlated single-photon counting method.....	48
4.2.2. Fluorescence decay analysis.....	53
4.3. Time-resolved emission spectra (TRES).....	55
4.4. Time-resolved anisotropy.....	60

<b>5. Sample preparation</b>	63
5.1. Buffer solutions.....	63
5.2. Monomerization of the beta-amyloid peptide (A $\beta$ <sub>1-40</sub> ).....	63
5.3. Preparing A $\beta$ <sub>1-40</sub> samples for measurements.....	63
5.3.1. A $\beta$ <sub>1-40</sub> sample.....	64
5.3.2. A $\beta$ <sub>1-40</sub> with copper ions (Cu <sup>2+</sup> ).....	64
5.3.3. A $\beta$ <sub>1-40</sub> with glucose .....	64
5.3.4. A $\beta$ <sub>1-40</sub> with quercetin.....	64
5.3.5. A $\beta$ <sub>1-40</sub> with Thioflavin T (ThT).....	65
5.4. Tyr, NAYA and A $\beta$ <sub>1-16</sub> with copper ions (Cu <sup>2+</sup> ).....	65
5.5. A $\beta$ <sub>1-11</sub> and A $\beta$ <sub>1-16</sub> with quercetin.....	65
5.6. Polystyrene standard beads.....	65
<b>6. Detecting beta-amyloid aggregation from time-resolved emission spectra</b>	66
6.1. Introduction.....	66
6.2. Results and discussion.....	68
6.3. Conclusion.....	73
<b>7. Copper ion (Cu<sup>2+</sup>) effects on beta-amyloid oligomerisation monitored by fluorescence of intrinsic tyrosine</b>	75
7.1. Introduction.....	75
7.2. Results and discussion.....	77
7.3. Conclusion.....	86
<b>8. Detecting beta-amyloid glycation by fluorescence of intrinsic tyrosine</b>	88
8.1. Introduction.....	88
8.2. Results and discussion.....	90
8.3. Conclusion.....	98
<b>9. Investigating the effect of quercetin on beta-amyloid aggregation by time resolved emission spectra (TRES)</b>	100
9.1. Introduction.....	100
9.2. Results and discussion.....	102
9.3. Conclusion.....	112
<b>10. Fluorescence anisotropy: a method for early detection of beta-amyloid aggregation</b>	114
10.1. Introduction .....	114

10.2. Results and discussion.....	115
10.3. Conclusion.....	119
<b>11. Nanoparticle tracking analysis (NTA) for the detection of beta-amyloid aggregates</b>	120
11.1. Physical principle underlying NTA.....	120
11.2. The Nanoparticle Tracking Analysis technique.....	121
11.3. Detection of beta-amyloid aggregation by NTA.....	124
11.3.1. Introduction.....	124
11.3.2. Results and discussion.....	126
11.3.3. Conclusion.....	129
<b>12. Conclusion</b>	131
<b>References</b>	136

# 1. Introduction

Neurodegenerative diseases (NDD) are debilitating and currently incurable conditions which primarily affect the neurons in the human brain. NDDs affect millions of people worldwide. And with the world population getting older<sup>1</sup>, the burden of NDDs is expected to mount<sup>2</sup>. Treatments may help relieve some of the mental or physical symptoms related to NDDs, however, their progression is irreversible and is accompanied by large personal and socioeconomic costs<sup>2</sup>. Although a wide range of diseases fall under the term neurodegenerative disease, Alzheimer's disease (AD) and Parkinson's disease (PD) are the most common.

AD was for many years ascribed to neurons death induced by deposits of fibrillar  $\beta$ -Amyloid ( $A\beta$ ) peptides. Recently, however, an alternative hypothesis has emerged, in which synapse failure is thought to be caused by soluble  $A\beta$  oligomers<sup>3-9</sup>. Accumulating research supporting this hypothesis has demonstrated that  $A\beta$  oligomers provide an intrinsic molecular basis for the cause, diagnosis, and treatment of Alzheimer's disease.

Detecting the oligomerization of  $A\beta$  at its early stages in terms of understanding how aggregation begins, how the local environment affects the aggregation pathway and what can be done to inhibit this aggregation before soluble toxic oligomers are formed, is paramount for developing intervention therapies. A significant research effort has been carried out in recent years to reveal detailed molecular mechanisms of the oligomerisation and fibrillisation of amyloids. Many techniques have been used for the purpose of developing a kinetic model that can explain the mechanisms of oligomer and amyloid fibril formation. Microscopic techniques such as atomic force microscopy (AFM) and transmission electron microscopy (TEM) provide valuable and detailed information about the dimensions and morphological characteristics of aggregates<sup>10-12</sup>. Nuclear magnetic resonance spectroscopy (NMR) technique enables visualization of molecular structures, detection of conformational changes and binding of small

molecules<sup>13</sup>. Recent developments in the NMR technique allows probing of interactions between A $\beta$  monomers and larger A $\beta$  assemblies with atomic resolution<sup>14</sup>. Dynamic light scattering (DLS) is commonly used to determine the size distribution of A $\beta$  aggregates<sup>15</sup>. The circular dichroism (CD) technique provides rapid evaluation of the secondary structure of the protein<sup>15,16</sup>. Conformation-specific antibodies are often used for their unique ability in recognising structural features of oligomers and amyloid fibrils<sup>17,18</sup>.

Fluorescence techniques have received special attention in recent years. This is due to their high sensitivity, specificity, and spatiotemporal resolution as well as the increasing availability of fluorescent probes, dyes, and proteins, which allow for non-invasive studies of protein-protein interactions, protein conformational changes, gene expression, and many other cellular processes<sup>19-21</sup>. In addition, the presence of chromophores in the human body, which are produced in excess amounts as a result of pathologies in the tissue such as nicotinamide adenine dinucleotide (NADH) and porphyrins in cancerous tissue, as well as chromophores that are present in normal tissue like flavin adenine dinucleotide (FAD), elastin, collagen, etc. make fluorescence techniques straightforward methods for the diagnosis of many diseases<sup>22-25</sup>.

In the case of tracking A $\beta$  aggregation reactions, most researchers use extrinsic fluorophores mostly because such a fluorescence capability is available in most laboratories and it has the advantage of being simple, rapid and extremely sensitive. Thioflavin T (ThT) is an example of a dye widely used to detect amyloid fibril sheet formation<sup>26-28</sup> even though it poorly detects early oligomer formation<sup>29-31</sup>. Other common fluorophores include 1-anilino-8-naphthalenesulfonate (ANS), 4,4'-dianilino-1,1'-binaphthyl-5,5'-disulfonic acid dipotassium salt (Bis-ANS)<sup>32, 33</sup>, Nile Red<sup>34</sup>, Congo Red<sup>28,35</sup> etc. Using extrinsic fluorophores in amyloid aggregation studies can be challenging due to the fact that the ratio of fluorophore to A $\beta$  can significantly influence the obtained results<sup>33</sup>. Moreover, it has been reported that some extrinsic fluorophores such as bis-ANS<sup>33</sup>, Congo red<sup>35</sup> and ThT<sup>36</sup> can affect the nucleation rate in some

cases, or even prevent aggregation<sup>37</sup>. Such complications can be avoided by exploiting A $\beta$ 's intrinsic fluorescence.

A $\beta$  is a peptide of 36–43 amino acids. It naturally occurs in the human body through sequential cleavages of the amyloid precursor protein (APP) by  $\beta$ - and  $\gamma$ -secretases. A $\beta$  peptides are found in nanomolar concentrations in biological fluids<sup>38</sup>. At these low concentrations, A $\beta$ s remain monomeric and function as antioxidants<sup>39</sup>. These monomeric forms of A $\beta$  are disordered and they have no regular secondary structure or fold<sup>40</sup>. Up to now there is no clear understanding on what initiates the aggregation of monomeric A $\beta$  peptides in the human body. However, in the case of Alzheimer's patients, A $\beta$  peptides self-assemble into small permeable toxic oligomers that can travel freely into the brain. Then at later stages, these aggregates grow into insoluble and less toxic protofibrils, fibrils and neurotic plaques<sup>41</sup>. This thesis is focused on studying the A $\beta_{1-40}$  peptide, which is the most abundant A $\beta$  peptide in the human brain<sup>42</sup>. Moreover, A $\beta_{1-40}$  amyloid deposits are found in patients affected by cerebral amyloid angiopathy, which is thought to be an initial phase in AD pathogenesis<sup>43,44</sup>.

A $\beta_{1-40}$  contains a single tyrosine residue (Tyr<sub>10</sub>) in addition to three phenylalanine residues (Phe<sub>4</sub>, Phe<sub>19</sub> and Phe<sub>20</sub>). Upon excitation at 280 nm, the intrinsic fluorescence of the peptide thus predominantly represents the fluorescence of the sole tyrosine residue. Time resolved spectroscopy studies of Tyr in A $\beta_{1-40}$  show that its fluorescence intensity decay at detection wavelength 315 nm is sensitive to peptide aggregation especially at its earliest stage<sup>29,45,46</sup>. Thus, can be used as a sensing tool for A $\beta_{1-40}$  oligomerization. However, in such heterogeneous fluorescent systems, where several processes affecting excited-state kinetics (like variable tyrosine local environments and/or dielectric relaxation) may be present, measuring the fluorescence decay at a single and arbitrary selected detection wavelength may not be sufficient to describe such a complex kinetics. For these cases the complementary technique such as time resolved emission spectra (TRES) may provide additional information. Indeed, the shape of

the A $\beta$ <sub>1-40</sub> spectrum at different moments of time after excitation and the way it evolves on the ns time scale may help to resolve the number of fluorescent sites involved and reveal the actual kinetics. Therefore, in this research we used both fluorescence intensity decays and TRES to maximize information on A $\beta$ <sub>1-40</sub> behaviour.

The overall aim of the studies presented in this thesis is to achieve molecular level understanding of the processes occurring in the early stages of beta-amyloid aggregation in a buffer solution, in the absence and presence of additional compounds affecting the progress of aggregation such as copper ions and glucose or factors that can potentially prevent aggregation like quercetin, by exploring mainly their intrinsic steady-state fluorescence, fluorescence intensity decay and anisotropy decay.

Chapter 2 describes amyloidosis and its relation to neurodegenerative diseases in general, the A $\beta$  peptide in particular and its association to Alzheimer's disease and the available techniques for the analysis of beta-amyloid aggregates.

In Chapter 3 details the underlying theoretical information regarding the fluorescence phenomenon, the general fluorescence characteristics and effects that one can expect in fluorescence studies of protein aggregation.

Chapter 4 describes in detail the fluorescence techniques employed to carry out this body of research, namely steady-state measurements, time-resolved fluorescence measurements of the intensity and anisotropy decays and time resolved emission spectroscopy TRES.

Chapter 5 characterises the samples used in this study and describes the method of sample preparation in each case. Samples include: (1) Pure A $\beta$ <sub>1-40</sub> to establish whether TRES is affected by peptide aggregation, (2) A $\beta$  with copper, which is considered a factor having large influence on aggregation, (3) A $\beta$  with glucose, to study the potential link between elevated glucose levels and A $\beta$  aggregation, (4) A $\beta$  with quercetin, as an example of a compound

crossing the blood-brain barrier, thus a potential drug for the disease or at least a nutrient helping prevent the disease.

Chapter 6 discusses the advantage of detecting beta-amyloid aggregation from time-resolved emission spectra, showing that time resolved emission spectra (TRES) of Tyr in A $\beta$ <sub>1-40</sub> can sufficiently demonstrate structural changes on the nanosecond time scale after excitation. Beta-amyloid's monomers can be distinguished from oligomers by means of the position of their emission spectra. Further spectral shift caused by dielectric relaxation can be useful for determining the size of the oligomers since their spectral shift gradually decreases as the aggregates grow larger.

Chapter 7 discusses Copper ion (Cu<sup>2+</sup>) effects on beta-amyloid oligomerisation monitored by fluorescence of intrinsic tyrosine. Fluorescence sensing of the early stages of A $\beta$ <sub>1-40</sub> aggregation in the presence of copper ions was achieved by intrinsic fluorescence time-resolved spectroscopy. By using time-resolved fluorescence techniques the formation of beta amyloid-copper complexes and the accelerated peptide aggregation are demonstrated. The shifts in the emission spectral peaks indicate that the peptides exhibit different aggregation pathways than in the absence of copper.

Chapter 8 demonstrates the feasibility of detecting beta-amyloid glycation by intrinsic fluorescence for the purpose of improving our molecular level understanding of the link between diabetes and Alzheimer's disease. In the presence of high glucose concentrations TRES measurements show the impact of glycation on A $\beta$ <sub>1-40</sub> oligomerisation, evidenced by the presence of the multiple peaks and their spectral shifts. Results shown in this chapter indicate that the formation of advanced glycation end products (AGEs) alters the aggregation pathway.

Chapter 9 discusses the effect of quercetin on beta-amyloid aggregation monitored by time resolved emission spectra (TRES) of intrinsic Tyrosine. In the presence of quercetin TRES exhibit multiple peaks with characteristic spectral shifts, indicating a different aggregation pathway. At a molar ratio of 1:1 ( $A\beta_{1-40}$  : Quercetin), TRES results show that small oligomers bound to quercetin grow in number rather than size with time of incubation. This was also confirmed by the ThT binding assay. Thus, quercetin experiments clearly showed early formation of  $A\beta$ -Quercetin complexes, which seem to inhibit further  $A\beta$  aggregation. This fact, combined with quercetin being a natural non-toxic substance capable of crossing the blood-brain barrier, makes it a potential nutrient that can help prevent or delay the development of Alzheimer's disease

The last two chapters report our efforts to use other than TRES to study  $A\beta$  aggregation and to explore synergy resulting from combining different experimental techniques.

Chapter 10 discusses fluorescence anisotropy of the intrinsic tyrosine residue as a method for early detection of beta-amyloid aggregation. It was found that time-resolved anisotropy measurements can efficiently follow the gradual transformation of  $A\beta_{1-40}$  peptides into small oligomers. However, when oligomers grow larger, their quantum yield diminishes and it becomes difficult to track them. In the presence of quercetin,  $A\beta_{1-40}$  aggregates reach their maximum size within 22 hr and then stop developing, which confirms quercetin's inhibitory effect on amyloid fibril formation. Anisotropy decays of  $A\beta_{1-40}$  in the presence of glucose were similar to those obtained for free  $A\beta_{1-40}$ . Thus, alterations in the aggregation pathway induced by the glucose presence were not visible using this technique.

Chapter 11 gives a brief introduction of the underlying physical principle, and the experimental implementation of the nano tracking analysis NTA technique. It also demonstrates the feasibility of detecting beta-amyloid aggregation in the absence and presence of quercetin using

NTA. It was found that the NTA instrument used to conduct the experiment can only operate on a particle size range of 100 to 1000 nm. NTA results show that the freshly prepared  $A\beta_{1-40}$  sample contains pre-formed aggregates and that quercetin slightly reduces the rate of the aggregation process at the molar ratio of 15:50 (Quercetin :  $A\beta_{1-40}$ ).

## 2. Amyloidosis

### 2.1. Introduction

Amyloidosis is a group of diseases in which abnormal proteins, known as amyloid fibrils, accumulate commonly in extracellular spaces of organs and tissues (plaques)<sup>47</sup> or in some cases as insoluble deposits inside the cell (intracellular inclusions)<sup>48</sup>. Amyloidosis can either be systemic or localized<sup>49,50</sup>. In systemic forms, amyloid fibrils are deposited in numerous tissues and organs by yet unknown mechanisms. In localized amyloidosis, deposits of amyloid fibrils are localized to one tissue. To date, 50 distinct proteins are known to assemble into amyloid fibrils related to human diseases. Table 1<sup>48</sup> shows examples of proteins or peptides known to assemble into amyloid fibrils and their associated neurodegenerative diseases.

**Table 1.** Proteins known to assemble into amyloid fibrils and their associated diseases<sup>48</sup>

Neurodegenerative diseases	
Protein/ peptide	Associated disease
$\alpha$ -Synuclein	Parkinson disease
$\alpha$ -Synuclein	Dementia with Lewy bodies
ABri	Familial British dementia
Actin	Various neurodegenerative disorders
ADan	Familial Danish dementia
Amyloid- $\beta$ peptide	Alzheimer disease
Androgen receptor with polyQ expansion	Spinal and bulbar muscular atrophy
Ataxins with polyQ expansion	Spinocerebellar ataxias
Atrophin 1 with polyQ expansion	Spinal and bulbar muscular atrophy
Ferritin	Neuroferritinopathy
Huntingtin with polyQ expansion	Huntington disease
Neuroserpin	Familial encephalopathy with neuroserpin inclusion bodies
Prion protein or fragments thereof	Spongiform encephalopathies
Superoxide dismutase	Frontotemporal dementia with Parkinsonism
TATA box-binding protein with polyQ expansion	Spinocerebellar ataxias 17
Tau	Frontotemporal dementia with Parkinsonism

advanced technologies such as cryo-electronic microscopy<sup>51,52</sup> and solid-state NMR spectroscopy<sup>53,54</sup> have helped identify the atomic structure of amyloid fibrils formed

from their monomeric protein precursors and explain how the formation of fibrils relates to disease. However, elucidating the driving force, or the trigger, of fibril formation remains unclear<sup>48</sup> and of major importance since insights into the mechanisms underlying aggregation of soluble, monomeric peptides into developed insoluble fibrils could help develop a therapeutic strategy that would possibly hinder, reverse or avoid fibril formation.

Although it is important to understand the mechanisms of fibril formation, the kinetics of fibril formation can be complicated, which makes the relationship between a certain mechanism and experimental observables unclear. The most accepted model describing the kinetics of amyloid formation is the nucleation-dependent polymerization model<sup>55,56</sup>, where the fibrillation process produces a sigmoidal kinetic curve (Figure 1). The first step in the process includes the formation of oligomers, which are transient, dynamic, heterogeneous and of unknown structure<sup>57</sup>. Oligomers then develop into higher-order structures, which can either be precursors of the amyloid fibril or off-pathway structures that cannot grow into fibrils<sup>48,55,57</sup>.

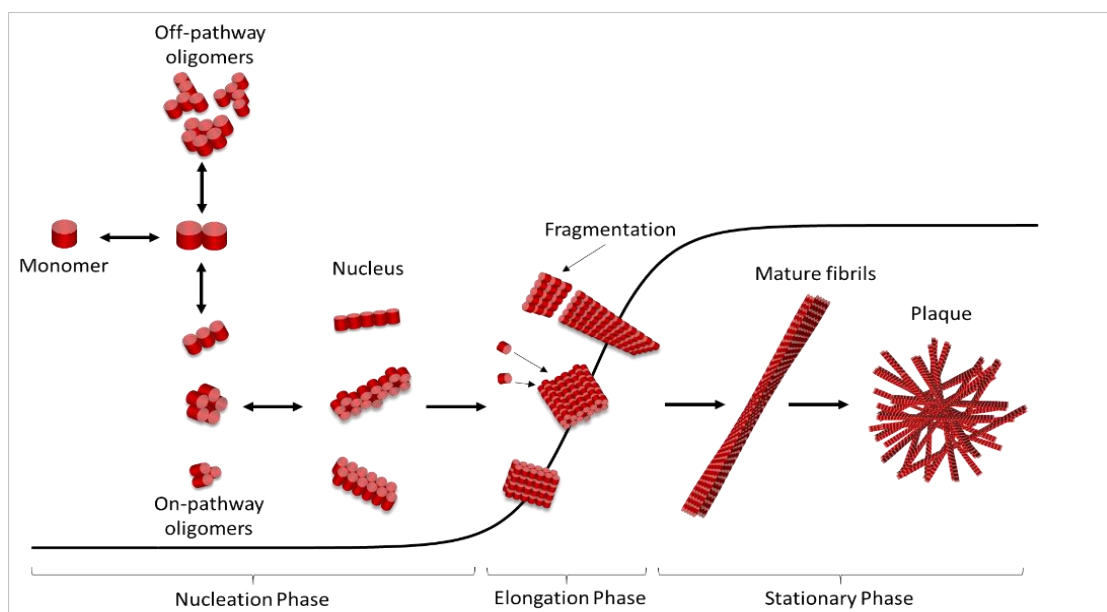


**Figure 1.** A schematic representation of the amyloid forming pathway

Off-pathway oligomers, however, might still be relevant to the disease due to the possibility of them being cytotoxic<sup>48,57</sup>. Once on-pathway oligomers reach a critical size, a nucleus is formed and a rapid, linear elongation of the aggregates would occur via the addition of monomeric proteins to the ends<sup>58</sup>. The possibility of nucleus formation partly determines the lag time length of amyloid self-assembly.

Irrespective of the precursor's initial fold, it will be subjected to structural transformation that would lead to the formation of a  $\beta$ -strand-rich secondary structure. Once the long cross- $\beta$  structures, called fibrils, are formed they can then fragment and produce other fibril ends that monomers can attach to, which result in exponential fibril growth and reduction in the length of the lag time of amyloid self-assembly<sup>58</sup>. The rate of fibril formation can also be enhanced by secondary nucleation<sup>55</sup>, where oligomer formation is accelerated on the surface of a pre-existing fibril.

Amyloid fibrils in general exhibit a similar underlying construction<sup>48</sup>, called the cross- $\beta$  fold, in which the  $\beta$ -strands within each protofilament line up perpendicularly to the fibril axis. The spacing between adjacent  $\beta$ -strands is around 4.7–4.8 Å, which is consistent with the well-known length of hydrogen bonds formed between the paired amide and carbonyl groups in adjacent  $\beta$ -strands.

The challenges we are facing today with Amyloids includes identifying what initiates the aggregation process, classifying the toxic species created during amyloid formation and understanding how they cause cellular dysfunction and death. Answering these demanding questions would enhance the progress in developing therapeutic strategies for a wide range of diseases related to amyloidosis (Table 1).

## 2.2. The Beta-Amyloid protein and the amyloid hypothesis

### 2.2.1. Alzheimer's disease

The clinical entity known as *Alzheimer's disease* (AD) was first described by the German psychiatrist, Alois Alzheimer, in the early 1900s<sup>59</sup>. In his report, he described the clinical course and changes in the brain of a 55-year-old woman, Auguste D., dying after a 4-year history of progressive dementia. Alois Alzheimer was able to demonstrate an overall reduction in the size of the cerebral cortex and the hippocampus (centre of memory and learning and), and enlarged ventricles (figure 2).

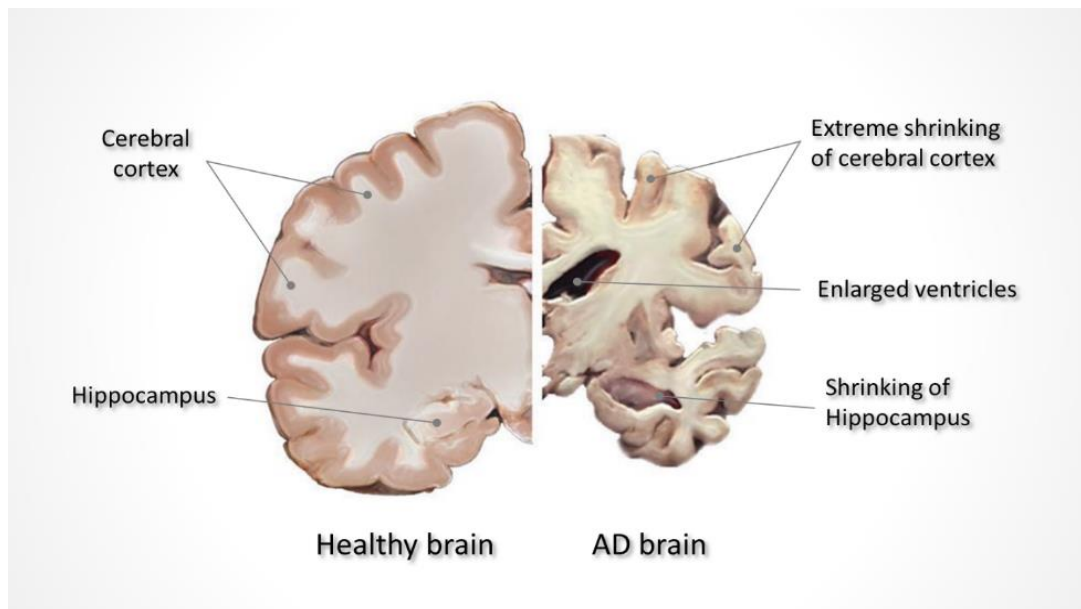


**Figure 2** Comparison of a healthy brain and a brain with severe Alzheimer's Disease (National institutes of Health NIH, 2016)<sup>221</sup>.

Dr. Alzheimer also demonstrated that many irregular clumps and tangled bundles of fibres were formed in the brain of the patient<sup>59</sup>. The plaques are found in the extracellular space of the brain and they are particularly present in the hippocampus region. Plaques are mainly composed of aggregates of a peptide called beta-Amyloid

(A $\beta$ )<sup>60</sup>. The intracellular neurofibrillary tangles in the brain are composed of a hyperphosphorylated Tau protein <sup>61</sup>. Tau proteins are abundant in neurons of the central nervous system. They stabilize microtubules by interacting with tubulin<sup>62</sup>. Microtubules are structures that help guide nutrients and molecules from the cell body to the axon and dendrites<sup>63</sup>. In the case of Alzheimer's, abnormal chemical changes cause Tau to detach from microtubules and stick to other Tau molecules, leading to the formation of tangles inside the neuron and destabilisation of the microtubules<sup>62</sup>. Emerging evidence<sup>64</sup> suggests that build-up of A $\beta$  between neurons causes activation of p38 MAPK (i.e. a class of mitogen-activated protein kinases (MAPKs) that are responsive to stress stimuli) in the cell, which leads to the abnormal phosphorylation of Tau. Thus, when the A $\beta$  level reaches a tipping point, a rapid spread of Tau is observed throughout the brain. Hence it is strongly believed that A $\beta$  plays the main role in neuronal dysfunction and AD<sup>65,66</sup>.

Identifying AD biomarkers has moved our understanding of the disease from one based on symptoms to one based on brain changes. Since these changes start well before clinical signs and symptoms appear, Alzheimer's can be diagnosed before the dementia stage. Early diagnosis of AD could have important personal and financial benefits. Hence, researchers from different fields are coming together to design and develop advanced diagnostic methods that might allow early-stage diagnosis of AD<sup>67-</sup><sup>69</sup>. The most promising methods to date are based on identifying the levels of Tau protein and A $\beta$  in cerebrospinal fluid (CSF)<sup>70</sup>. Moreover, considerable efforts are made to advance A $\beta$  and Tau as blood-based biomarkers for AD<sup>71,72</sup>.

### 2.2.2. Beta amyloid formation

Beta-amyloid can be produced by different types of cells such as smooth muscle cells, neurons, astrocytes, platelets, and fibroblasts<sup>73,74</sup>. The A $\beta$  peptide is released after a number of sequential cleavage events of the amyloid precursor protein (APP) found on the surface of cells throughout the body. APP is a large transmembrane protein, composed of 695-770 amino acids<sup>75</sup>. It has a large extracellular domain, a single intramembranous domain and a short cytoplasmic domain (Figure 3). The A $\beta$  sequence is partially embedded in the plasma membrane.

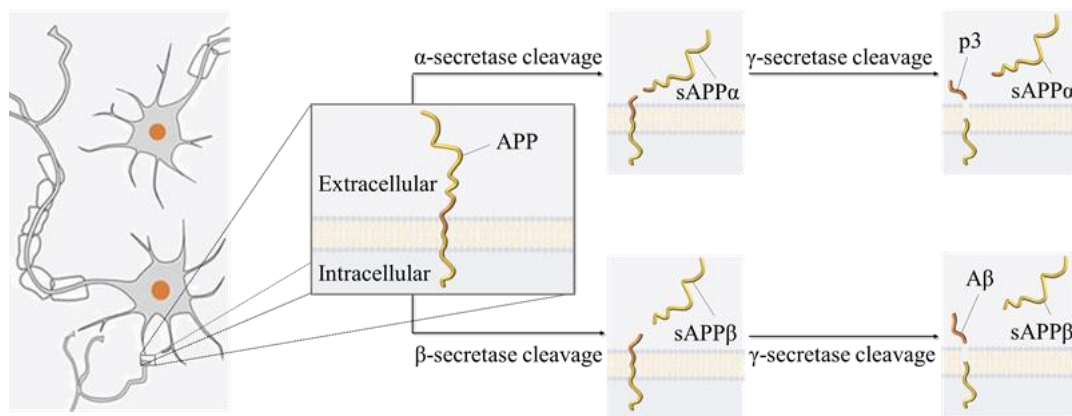


**Figure 3.** Schematic depiction of the APP processing and cleavage products. The primary pathway of APP processing involves cleavages by  $\alpha$ - and  $\gamma$ -secretases resulting in the formation of a long-secreted form of APP (sAPP $\alpha$ ) and a shorter fragment (p3). Alternatively, the amyloidogenic pathway involves the sequential action of  $\beta$ - and  $\gamma$ -secretases liberating sAPP $\beta$  and A $\beta$  from APP. (OpenClipart-Vector, n.d.)<sup>222</sup>.

There are two APP processing pathways<sup>75,76</sup> mediated by a number of proteolytic enzymes;  $\alpha$ -secretase,  $\beta$ -secretase and  $\gamma$ -secretase. The primary pathway of APP processing involves the sequential action of  $\alpha$ - and  $\gamma$ -secretases. The  $\alpha$ -secretase cleaves APP within the A $\beta$  domain releasing a large soluble fragment of APP (sAPP $\alpha$ ). This is followed by a  $\gamma$ -secretase cleavage within the intramembranous portion of APP, which leads to the formation of a shorter fragment (p3), the p3 peptide

has no known function and is not associated with plaque formation<sup>77,78</sup>. This pathway is therefore non-amyloidogenic. The alternative pathway involves sequential cleavage by  $\beta$ - and  $\gamma$ -secretases. The  $\beta$ -secretase cleavage site is located at the distal end of the A $\beta$  sequence. Therefore, processing APP via the alternative pathway leads to the formation of the pathogenic A $\beta$  species. It should be noted that  $\gamma$ -secretase proteases exhibit low substrate sequence specificity. Consequently, A $\beta$  peptides of varying lengths are formed with the main product being 40 residues long (A $\beta_{1-40}$ ). The elongated A $\beta$  peptide consisting of 42 amino acids (A $\beta_{1-42}$ ) is produced to a lower extent, but is more prone to aggregation than A $\beta_{1-40}$ .

### **2.2.3. Beta amyloid aggregation**

The monomeric form of A $\beta$  is disordered and lacks any regular secondary structure or fold<sup>40</sup>. However, A $\beta$  is considered an amphiphilic molecule due to the fact that residues 1 to 16 are hydrophilic while residues 17 to 40/42 are mainly hydrophobic. The amphiphilic nature of this molecule is thought to drive its ability to spontaneously aggregate, at least under certain circumstances, into multimers, oligomers and large fibrillar aggregates with a highly ordered cross-beta sheet structure. Although deposition of A $\beta$  fibrils is one of the major pathological hallmarks of Alzheimer's disease, it is widely accepted that small oligomeric intermediates are more toxic to cells and synapses than mature fibrils<sup>79</sup>. Yet there is still no clarity as to which of the bewildering list of A $\beta$  oligomeric species, identified in literature, is pathologically relevant in Alzheimer's disease<sup>79</sup>.

### **2.2.4. Methods for analysis of beta-amyloid aggregates**

Over the past century, many theories and experimental tools have been established to study protein structure-function relationships. Identifying the size, structure and

function of proteins helps determine tissue physiology or disease pathology. Thus, many experimental tools and techniques have been established providing complementary information regarding the morphology of static structures, molecular resolution of static structures, near-molecular resolution of dynamic structures, and dynamic measures of molecular self-assembly.

Since the early to mid 1900's, many tools were developed to visualize molecular structures. X-ray crystallography, for instance, was developed to determine the 3-dimensional (3D) atomic crystal structure of biomolecules. To obtain an x-ray structure, molecules need to be crystallised, but many proteins can only be crystallised with difficulty, if at all, and even then, the observed conformation may not be representative of the molecule in real life. In contrast, the Nuclear Magnetic Resonance Spectroscopy (NMR) technique enables visualization of molecular structures without crystallization<sup>13</sup>, and allows detection of conformational changes or binding of small molecules. However, NMR is limited to relatively small proteins or parts of proteins<sup>13</sup>. Larger proteins or complexes of several biomolecules cannot be determined using NMR. However, recent developments in the NMR technique have allowed probing of interactions between A $\beta$  monomers and larger A $\beta$  assemblies with atomic resolution<sup>14</sup>. Electron microscopy (EM) is another imaging technique that allows for the observation of biomolecules at sub-nanometer resolution. Imaging with EM, however, requires protection of biological materials from the intense beam of electrons and the high vacuum conditions. To protect samples from these extreme conditions they can either be dried and stained with heavy metals or rapidly cooled and imaged under cryogenic conditions<sup>52,80,81</sup>. Atomic force microscopy (AFM) is arguably the most powerful and versatile microscopy technology for studying samples on the nanoscale<sup>12</sup>. Unlike the EM, AFM does not require any sample preparation and

works perfectly well in ambient air or even a liquid environment. However, a significant limitation to both EM and AFM is that the results they provide will be inevitably affected by the biased adsorption of aggregates onto the sample substrates<sup>82,83</sup>

Light scattering techniques are commonly utilized to determine molecular sizes and interactions in pure solutions<sup>84</sup>. Although they are simple and easily applicable techniques that allow for rapid and non-invasive analysis of many types of materials, these methods have several pitfalls. They usually make no allowance for the shape of the particles being tested, since the mathematical models used to calculate the distributions are based on spherical systems<sup>85,86</sup>. Therefore, any measured distribution using light scattering techniques is basically equivalent to a spherical distribution of the material under study. They also give inaccurate measurements of the size distribution of small particles when small amounts of large aggregates are present in the sample<sup>87</sup>. An excellent tool for rapidly evaluating the secondary structure, folding and binding properties of proteins is circular dichroism (CD). CD is a form of light absorption spectroscopy that measures the difference in absorbance of left-handed and right-handed circularly polarized light. Because different types of secondary structures,  $\alpha$ -helix,  $\beta$ -sheet and random coil, have characteristic CD spectra in the far-UV region of the spectrum (i.e. 190-250 nm), far-UV CD is widely used to investigate the secondary structure of proteins<sup>88</sup>, whereas near-UV CD (i.e. >250 nm) is used to measure tertiary folding<sup>89,90</sup>. However, using this technique in quantitative estimations for  $\beta$ -sheet-containing proteins is challenging because of the vast morphological and spectral diversity of  $\beta$ -structures<sup>91</sup>. Hence predictions for proteins of unusual  $\beta$ -structures such as membrane proteins, protein aggregates, and amyloid fibrils are less reliable<sup>92</sup>. Another well-established tool for determining secondary

protein structure is Fourier transform infrared (FTIR) spectroscopy<sup>93,94</sup>. It is rapid, requires less sample preparation than most techniques and spectra can be obtained across different protein sizes and in numerous environments<sup>95</sup>. However, specificity and interpretability of FTIR spectroscopy may be limited due to overlapping or non-diagnostic spectral bands.

Noncovalent, extrinsic fluorescent dyes were also used in many fields of protein analysis<sup>96</sup>. For example measuring surface hydrophobicity<sup>97</sup>, identifying protein folding intermediates<sup>98</sup>, and tracking aggregation or fibrillation<sup>99,100</sup>. The main mechanisms underlying the fluorescence properties of most extrinsic dyes are (twisted) intramolecular charge transfer reactions and solvent relaxation processes, which are influenced by the dye-protein interactions and the changes in the environment. The employment of extrinsic fluorescent dyes such as 1-anilino-8-naphthalenesulfonate (**ANS**), 4,4'-dianilino-1,1'-binaphthyl-5,5'-disulfonic acid dipotassium salt (**Bis-ANS**), Nile Red, Thioflavin T (**ThT**), etc. has the advantage of being simple, rapid, extremely sensitive and suitable for high-throughput screening. However, this approach cannot be applied in brain tissue because of the blood–brain barrier. Thioflavin T is an example of a dye widely used to characterize amyloid aggregates *in vitro* and *ex vivo*<sup>101</sup>, but due to its charge and hydrophilic nature it cannot be used for *in vivo* studies. Nevertheless, this dye has provided a starting point for the development of uncharged thioflavin derivatives, which can be used to detect amyloid *in-vivo*<sup>102</sup>.

Another fluorescence-based measurement method is fluorescence correlation spectroscopy (FCS). FCS is basically a correlation analysis of the temporal fluctuation of fluorescence intensity. The fluctuations in fluorescence arise from the Brownian motion of particles in the focal volume or because of chemical reactions<sup>103</sup>. Thus,

fluorescence fluctuations carry information about the size and concentration of the detected particles<sup>103,104</sup>. Several attempts employing FCS and labelling amyloids with fluorescent probes like ARCAM-1<sup>105</sup>, ThT<sup>106</sup> or HiLyte Fluor 488<sup>107</sup> allowed the characterisation of aggregation intermediates during the assembly process. Recent studies suggest that extrinsic dyes should be used with caution when studying amyloid fibril formation specifically in the presence of exogenous compounds that may affect their fluorescence readings<sup>108</sup>. Moreover, it has been reported that extrinsic dyes can to some extent influence the amyloid aggregation process<sup>36</sup>.

Usually, the characterization of the kinetics of fibrillation process requires the combination of several techniques due to the metastable nature of the prefibrillar assemblies and the non-crystalline nature of fibrillar protein aggregates. Thus, one challenge is to propose a simple and non-invasive method which permits information simultaneously about the shape, size and distribution of heterogeneous protein aggregates specifically at the early stages of the process. The approach reported in this thesis is based on utilization of A $\beta$ 's intrinsic fluorophore tyrosine (Tyr) to probe the peptides early stages of aggregation. Time-resolved fluorescence spectroscopy is sensitive to changes in the Tyr local environment and thus can be used to monitor molecular interactions and motions that occur in the pico-to nanosecond timescale including reorientation of solvent molecules, rotational diffusion of macromolecules and energy transfer.

## 3. Fluorescence

### 3.1. Fluorescence theory

Spectroscopy is a branch of science concerned with the investigation of the interaction of electromagnetic radiation with matter. In this work we focus primarily on luminescence spectroscopy, specifically fluorescence - an emissive process on the ns time scale, associated with the transition from the excited singlet state of the fluorophore to the ground state. Fluorescence spectroscopy techniques are widely used for examining static and dynamic properties of different systems because fluorophores (fluorescent chemical compounds) are energetically rich species upon excitation and can strongly interact only with immediate neighbouring molecules. These interactions with the microenvironment affect the fluorophore's properties and fluorescence characteristics, which in turn provides indirect but very useful information on the host system <sup>109</sup>. Another important feature of fluorescence spectroscopy is the convenient ns time scale of the fluorescence process, which enables monitoring fast kinetics such as translational and rotational diffusion of fluorescent molecules, reorientation of molecules in the solvation shell and nonradiative excitation energy transfer, etc.

Here we outline the general principles of fluorescence spectroscopy. The radiative and nonradiative transitions, the Franck–Condon principle and the Jablonski diagram are described and explained.

Light - absorbing molecules contain antennae groups known as chromophores, which are responsible for the absorption of light. When chromophores are subjected to an oscillating electromagnetic radiation of appropriate energy, an electron in the chromophore at the ground state  $\Psi_i$  can be promoted to a higher energy excited state  $\Psi_j$  given that the energy of the photon corresponds with the difference in energy between

the two quantised electronic energy states involved in the transition <sup>110</sup>. This process of electron displacement during the transition causes the related chromophore to undergo an electric dipole transition in which the energy of the absorbed photon becomes part of the excited molecule total energy. The square of this transition dipole moment  $|M_{ji}^2|$  is proportional to the probability or the intensity of a transition from  $\Psi_i$  to  $\Psi_j$ . In quantum mechanics the transition dipole moment  $\vec{M}_{ji}$  is given by:

$$\vec{M}_{ji} = \int \Psi_j^* \vec{\mu} \Psi_i d^3r \quad 1$$

Where  $\Psi_i$  and  $\Psi_j$  are two different eigen states in one molecule,  $\vec{\mu}$  is the dipole moment operator and the integral is over all space.  $\vec{\mu}$  is the product of the particle's charge  $q$  and its position  $r$ . However, in a system with  $n$  charged particles,  $\vec{\mu}$  would be the sum of every individual charge  $q_n$  multiplied by its position  $r_n$

$$d^3r \vec{\mu} = \sum_n q_n r_n \quad 2$$

To fully understand the effects of electronic excitation in molecules the motion of the nuclei must be taken into account<sup>110</sup>. The total energy of a molecule  $E_t$  is composed of energy due to nuclear motion (vibrational and rotational) and electronic energy. According to the Born – Oppenheimer approximation, these energies can be treated separately because the energy gap between electronic states is much greater than that between vibrational states, which in turn is much greater than that between rotational states. As a result the total wave function can be separated into electronic, vibrational and rotational parts

$$\Psi(r, R) = \psi_e(r, R_e) \cdot \psi_v(R) \cdot \psi_r(R) \quad 3$$

The electronic wave function,  $\psi_e$ , is approximated in all electronic coordinates at the equilibrium nuclear coordinates ( $R_e$ ) based on the Born-Oppenheimer assumption. The mass of electrons is much smaller than the nuclear mass, thus the rotational wave function  $\psi_r$  only depends on nuclear coordinates. For simplicity the rotational wave function will not be considered here because most of the spectra are not rotationally resolved. Therefore, the transition moment integral can be adequately expressed as<sup>11</sup>

$$M = \iint \psi_e'^*(r, R_e) \cdot \psi_v'^*(R) (\mu_e + \mu_n) \psi_e(r, R_e) \cdot \psi_v(R) dr dR \quad 4$$

where  $\psi$  and  $\psi'$  designate the lower and upper energy states respectively. Both the nuclear and electronic parts contribute to the dipole moment operator. Equation 4 can be integrated by two parts, with  $\mu_n$  and  $\mu_e$  respectively. A product of two integral is obtained

$$M = \int \psi_e'^*(r, R_e) \cdot \mu_e \cdot \psi_e(r, R_e) dr \int \psi_v'^*(R) \cdot \psi_v(R) dR + \int \psi_v'^*(R) \cdot \mu_n \cdot \psi_v(R) dR \int \psi_e'^*(r, R_e) \cdot \psi_e(r, R_e) dr \quad 5$$

Electronic wave functions are orthogonal to each other thus the integral  $\int \psi_e'^*(r, R_e) \cdot \psi_e(r, R_e) dr$  is zero and Equation 5 becomes

$$M = \int \psi_e'^*(r, R_e) \cdot \mu_e \cdot \psi_e(r, R_e) dr \int \psi_v'^*(R) \cdot \psi_v(R) dR \quad 6$$

The first integral of the above equation defines the electronic selection rules, while the second integral is the basis of vibrational selection rules.

Selection rules can be easily determined by identifying the symmetry of the transition moment function  $\psi'^* \mu \psi$ , if the integrand is symmetric or even (i.e.  $f(x) = f(-x)$ ) than the value of the integral will not be zero and the transition is allowed. On the other hand, if

the integrand is antisymmetric or odd (i.e.  $f(x) = -f(-x)$ ) the integral would be zero and the transition is forbidden.

An electronic transition to a higher excited state due to photon absorption is an extremely fast process that occurs within  $10^{-15}$  s. It is basically instantaneous compared with the time scale of nuclear motions. Therefore, it is safe to assume that electronic transitions are most likely to occur without changes in the positions of the nuclei in the molecular system or its environment. This is known as the Franck-Condon principle<sup>111</sup>. Accordingly, if a molecule is to move from one vibrational level during an electronic transition to another, the transition is most likely to happen if these two vibrational states have a large overlap (Figure 4a). This explains why some peaks in the absorption spectrum appear strong while others appear weak (Figure 4b). The vibrational overlap between any two eigenstates is expressed by the second integral in equation 6. The square of that integral is called the Franck-Condon factor:

$$\text{Franck - Condon factor} = \left| \int \psi_v'^*(R) \cdot \psi_v(R) dR \right|^2 \quad 7$$

Figure 4 illustrates the transition of a diatomic molecule from the ground state to a higher excited state. The lower curve represents the energy of the ground state as a function of distance between the two nuclei. The upper curve represents the energy of the first excited state  $S_1$ . Note that the equilibrium bond length in the excited state is shifted to the right because the excited bimolecular molecule is typically larger<sup>109</sup>. The vibrational states of each electronic state are represented by the horizontal wave

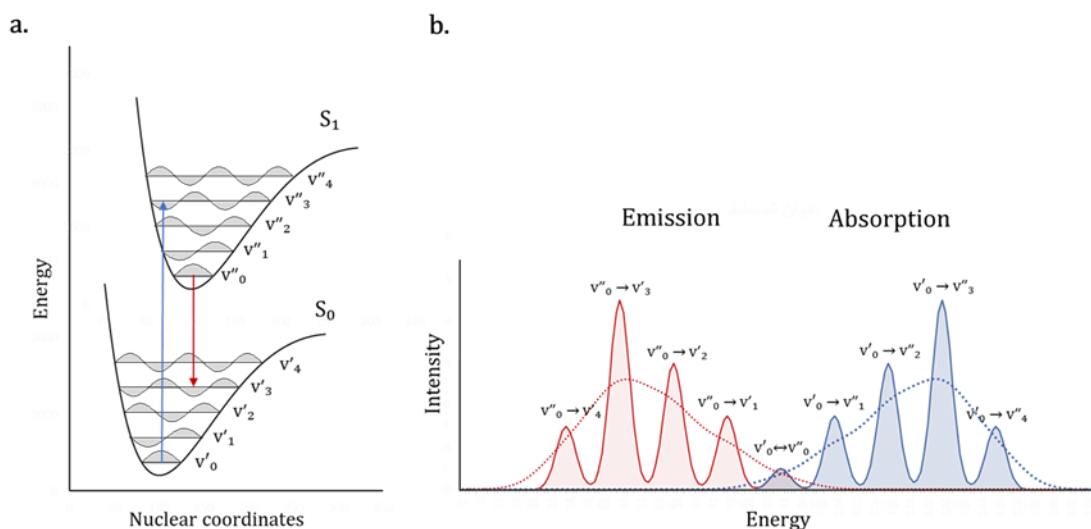


**Figure 4.** a) Franck–Condon principle energy diagram. The potential wells are shown favoring transitions between  $v = 0$  and  $v = 3$ . b) Schematic representation of the absorption (blue) and fluorescence (red) spectra corresponding to the energy diagram in Figure 4, a. The Absorption-emission symmetry is due to the equal shape of the ground and excited state potential wells. The narrow lines can usually only be observed in the spectra of dilute gases. The dotted-line curves represent the inhomogeneous broadening of the same transitions as occurs in liquids.

functions. Transitions are represented by vertical arrows due to the assumption of constant nuclear coordinates during the transition. At room temperature most molecules will be at the lowest vibrational state  $V_0$  of the electronic ground state  $S_0$  according to the Boltzmann distribution law:

$$N_1/N_0 = \exp(-\Delta E/kT) \quad 8$$

where  $N_0$  and  $N_1$  are the number of molecules in the ground state and a higher energy state respectively,  $\Delta E$  is the difference between energy levels,  $k$  is Boltzmann constant ( $k = 1.380649 \times 10^{-23} \text{ J K}^{-1}$ ) and  $T$  is the absolute temperature. Therefore, absorption will almost always occur from  $S_0 (v_0)^{110}$ . The most probable transition due to photon absorption is represented by the blue arrow in figure (4a). This vibronic transition (i.e. a transition that involves a change in both electronic and vibrational states) is most probable because the overlap between  $v_0$  and  $v'_2$  is the greatest.

Molecules in the excited state try to get rid of the excess energy as fast as possible <sup>109</sup>. In a condensed environment, the fastest process would be the vibrational relaxation process ( $10^{-14}$ - $10^{-12}$  s in a non-viscous solution). It is a non-radiative process that carries the molecule to the lowest vibrational level of the lowest excited singlet state by transferring excess energy to the surrounding medium during collisions with the neighbouring molecules<sup>109</sup>. Then a radiative transition to the electronic ground state, known as fluorescence, can occur. The red arrow shown in figure (4a) represents the most probable radiative transition from the electronic excited state  $S_1(v_0)$  to the ground state  $S_0$ .

Many relaxation mechanisms, however, compete with the fluorescence process<sup>112</sup>. The Jablonski diagram is often used to describe the radiative and nonradiative relaxation mechanisms for excited state molecules (Figure 5). Absorption of light carries a molecule to some higher vibrational level of either  $S_1$  or  $S_2$ . Subsequently, nonradiative transitions would occur through numerous mechanisms.

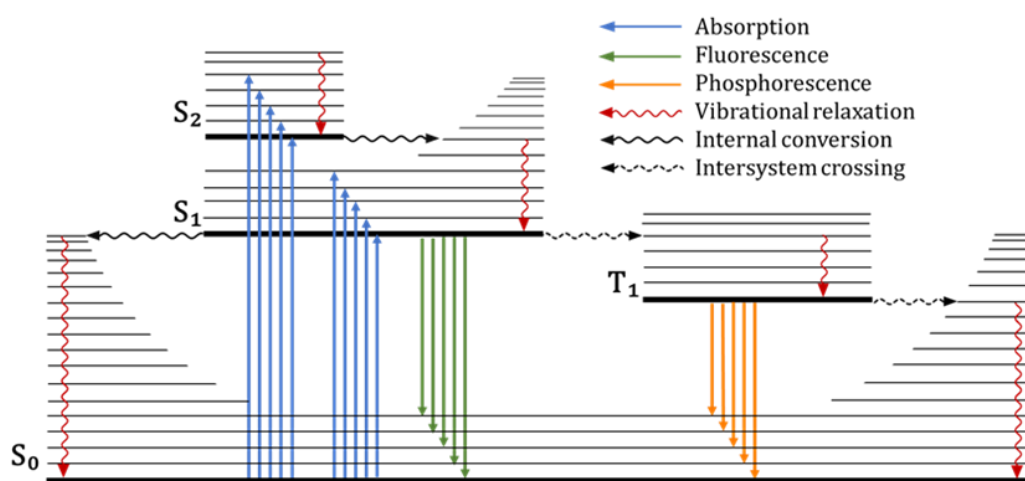


**Figure 5.** Illustration of the Jablonski diagram showing the possible radiative and non-radiative transitions.

In addition to vibrational relaxation, which allows the excited molecule to relax to the lowest vibrational level, there is internal conversion. This transition happens when a vibrational state of an excited electronic state can couple with a vibrational state of a lower electronic state. The rate of internal conversion between two electronic states is inversely proportional to the energy gap between those two levels<sup>113</sup>. The energy splitting between the ground state and the first electronic state is considerably large compared to energy splitting between higher-lying electronic excited states. Accordingly, the rate of internal conversion between  $S_1$  and  $S_0$  would be slow and comparable to that of radiative transition. Higher-lying electronic states, on the other hand, would experience faster internal conversion that would mostly outcompete the rate of radiative transitions. Thus, the  $S_1 (v_0) \rightarrow S_0$  fluorescence emission is usually the only radiative transition that can be observed. This principle is the physical basis of the Kasha's Rule<sup>114</sup> which states that: "luminescence only occurs with appreciable yield from the lowest excited state of a given multiplicity". Another type of nonradiative transition is intersystem crossing<sup>115</sup>. This process involves a transition to a state with a different spin multiplicity  $S_1 \rightarrow T_1$ . Such transitions are common in heavy-atom molecules with strong spin-orbit coupling. However, they were not observed in  $A\beta$  samples during peptide aggregation. When intersystem crossing occurs, the excited electron becomes trapped in the triplet state with only spin-forbidden transitions available to return to the ground singlet state. Therefore, the rate constant of the radiative transitions  $T_1 \rightarrow S_0$ , termed phosphorescence, is several orders of magnitude smaller than that for fluorescence.

## 3.2. Characteristics of fluorescence emission

Fluorescence emission of a given fluorophore often exhibits a number of general characteristics. In the following sections we will review the fluorescence characteristics and effects that one can expect in fluorescence studies of protein aggregation.

### 3.2.1. Stokes shift

Energy of fluorescence emission is in general lower than that of absorption as the Jablonski diagram clearly shows. This energy difference is called the Stokes shift and it is mainly due to vibrational relaxation, which carries the excited molecule rapidly to the lowest vibrational level of  $S_1$ . Fluorescent molecules may exhibit a further Stokes shift due to solvent reorganization<sup>115,116</sup>. Figure 6 illustrates solvent molecules surrounding a fluorophore before and after excitation.

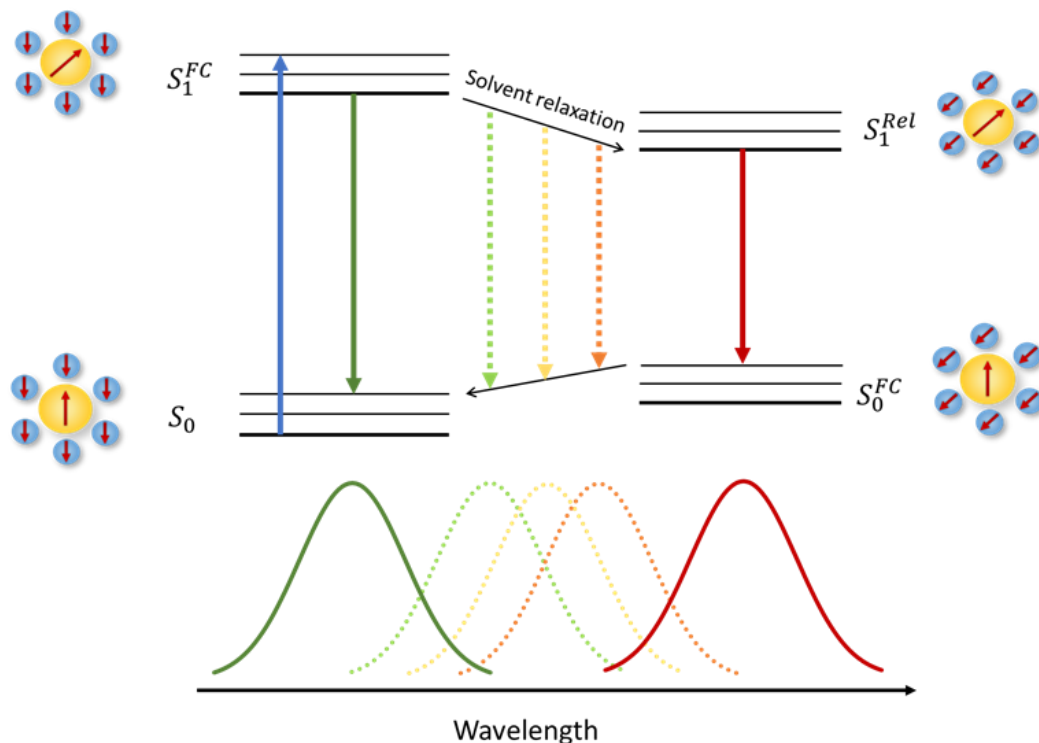


**Figure 6.** Jablonski diagram showing the effects of solvent relaxation on the emission energy

Initially the solvent molecules dipole moments interact with the fluorophore's dipole moment to yield an energetically favourable configuration  $S_0$ . Upon excitation the fluorophore's dipole moment changes, which then induces solvent molecules to re-orientate themselves around the excited fluorophore to minimize the total energy of the system. However, absorption of a photon is a very fast process ( $10^{-15}$ sec) that occurs in a far shorter timeframe than it takes for solvent molecules to rearrange themselves around the excited molecule. Therefore, the excited molecule becomes in an energetically unfavourable Frank-Condon excited state  $S_1^{FC}$ . After solvent relaxation, which typically takes around  $10^{-11}$  to  $10^{-10}$  sec, the excited state becomes in an energetically favourable configuration  $S_1^{Rel}$ . The fluorophore remains in the excited state for around  $10^{-10}$  -  $10^{-7}$  sec before it emits a photon and returns to the ground state. In the ground state solvent molecules will once again be in an unfavourable arrangement  $S_0^{FC}$  and then undergo re-orientation to reach an energetically favourable configuration  $S_0^{Rel}$ . This has the effect of decreasing the energy split between the excited state and the ground state, which leads to a further red shift in fluorescence emission. Therefore, increasing the solvent polarity will lead to a larger Stokes shift. The fluorophore's polarity is also relevant as it determines the sensitivity of the excited state to solvent effects.

In some situations, fluorophores can emit before or during solvent relaxation<sup>115,116</sup>. This can occur if the rate of solvent relaxation around the fluorophore is slower or comparable to the fluorescence decay rate. The rate of solvent relaxation depends on the mobility of the fluorophore's solvation envelope (i.e. local viscosity). Under these conditions the emission spectra exhibit time-dependent changes. For a homogeneous sample<sup>116</sup>, the spectral centroid of the emission spectrum  $\nu(t)$  would shift exponentially towards longer wavelengths and can be assumed using the equation:

$$\nu(t) = \nu_{\infty} + (\nu_0 - \nu_{\infty})e^{\frac{-t}{\tau_s}} \quad 9$$

where  $\nu_0$  and  $\nu_{\infty}$  are the spectral centroids at  $t=0$  and  $t=\infty$  respectively and  $\tau_s$  is the solvent relaxation time. For a heterogeneous sample, however, the emission spectra of individual fluorophores shift differently and the experimental centroid of the emission spectrum may be more complex than exponential.

### 3.2.2. Fluorescence quantum yield

The fluorescence quantum yield (Q) is the ratio of the number of photons emitted to the number of photons absorbed by the sample<sup>115</sup>.

$$Q = \frac{\textit{Photons emitted}}{\textit{Photons absorbed}} \quad 10$$

The quantum yield can also be determined by the relative rates of the radiative and non-radiative pathways, which depopulate the excited state<sup>115</sup>

$$Q = \frac{k_r}{k_r + \sum k_{nr}} \quad 11$$

where  $k_r$  and  $k_{nr}$  are the decay rates of the radiative and non-radiative processes, respectively.  $\sum k_{nr}$  includes all decay rate constants for the various processes that compete with the emission process, such as internal conversion, intersystem crossing, quenching etc.

### 3.2.3. Fluorescence lifetime

Fluorescence lifetime ( $\tau$ ) denotes the average time a molecule remains in its excited state before returning to the ground state. The mathematical expression of  $\tau$  can be given in terms of radiative and non-radiative decay constants<sup>117</sup>

$$\tau = \frac{1}{k_r + \sum k_{nr}} \quad 12$$

However, fluorescence emission is a random process and only few molecules emit their photons at exactly  $t = \tau$ . For instance, if the decay is a single exponential (Equation 15), 63 % of the excited molecules decay before  $t = \tau$  and 37% decay at  $t > \tau$ .

Exciting a population of molecules using a light pulse with a  $\delta$ -function at  $t=0$ , brings a number of molecules  $[M^*]$  to the  $S_1$  singlet excited state. The rate equation describing the decay of this population of excited molecules  $[M^*]$  from state  $S_1$ , due to fluorescence emission is<sup>117</sup>:

$$\frac{d[M^*]}{dt} = -(k_r + k_{nr})[M^*] = -\frac{[M^*]}{\tau} \quad 13$$

the solution to the above differential equation is an exponential function:

$$[M^*](t) = [M^*](0)e^{-\frac{t}{\tau}} \quad 14$$

And since fluorescence intensity  $I$  is proportional to the number of excited molecules  $[M^*]$  the above equation can be written in the form:

$$I(t) = I(0)e^{-\frac{t}{\tau}} \quad 15$$

In the presence of multiple non-interactive fluorescent species, the same treatment can be extended linearly by adding further exponential terms describing different lifetimes.

$$I(t) = \sum_{i=1}^n I_i(0)e^{-\frac{t}{\tau_i}} \quad 16$$

### 3.2.4. Fluorescence quenching

Quenching refers to any process which reduces the fluorescence intensity of a given substance. Fluorescence intensity can be reduced by a variety of processes<sup>115</sup>, such as collisional quenching, excited state reactions, complex-formation and energy transfer.

#### Collisional quenching

Collisional quenching occurs when the excited fluorophore experiences contact with an atom or molecule that can facilitate non-radiative transitions to the ground state<sup>115</sup>. Molecular oxygen<sup>118</sup>, iodide ions and acrylamide are examples of common chemical quenchers<sup>119</sup>. In the simplest case of collisional quenching, the Stern-Volmer relation holds<sup>120</sup>:

$$\frac{F_0}{F} = \frac{\tau_0}{\tau} = 1 + K_{sv}[Q] \quad 17$$

where  $F_0$  and  $F$  are the fluorescence intensities observed in the absence and presence of quencher respectively,  $\tau_0$  and  $\tau$  are lifetimes in the absence and presence of quencher respectively,  $[Q]$  is the quencher concentration and  $K_{sv}$  is the Stern-Volmer quenching constant, which can be expressed in the form  $K_{sv} = k_q \tau_0$  where  $k_q$  is the quenching rate constant (Figure 7).

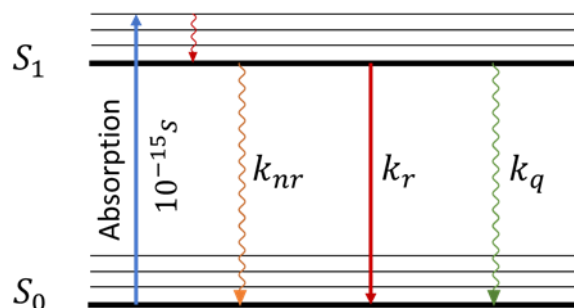


**Figure 7.** A Jablonski diagram showing three possible relaxation mechanisms; A non-radiative relaxation with a decay rate  $k_{nr}$ , radiative emission characterised by the decay constant  $k_r$  and collisional quenching with rate constant  $k_q$ .

### Static Quenching

Static quenching occurs if the fluorophore can form a complex with the quencher in the ground state, so that its emission is abolished. In such a case, fluorescence intensity would decrease but not the lifetime<sup>120,121</sup>. This happens because the fluorophores interacting with the quencher become non-fluorescent and those that do not interact emit normally. When static quenching occurs, the dependence of fluorescence intensity as a function of the quencher concentration follows the relation:

$$F_0/F = 1 + Ka[Q] \quad 18$$

where Ka is the association constant of the complex.

### Fluorescence Resonance Energy Transfer

Resonance energy transfer (RET) or fluorescence resonance energy transfer (FRET), is a mechanism describing energy transfer between two light-sensitive molecules<sup>115</sup>. This process occurs only if the emission spectrum of one fluorophore, called the donor, overlaps with the absorption spectrum of another molecule, called the acceptor (Figure 8a). the donor fluorophore, initially in the electronic excited state, may transfer energy to the acceptor molecule through nonradiative dipole-dipole

interactions (Figure 8b). This leads to a decrease in the donor's fluorescence intensity and lifetime and enhances the fluorescence of the acceptor probe, if the acceptor is fluorescent.

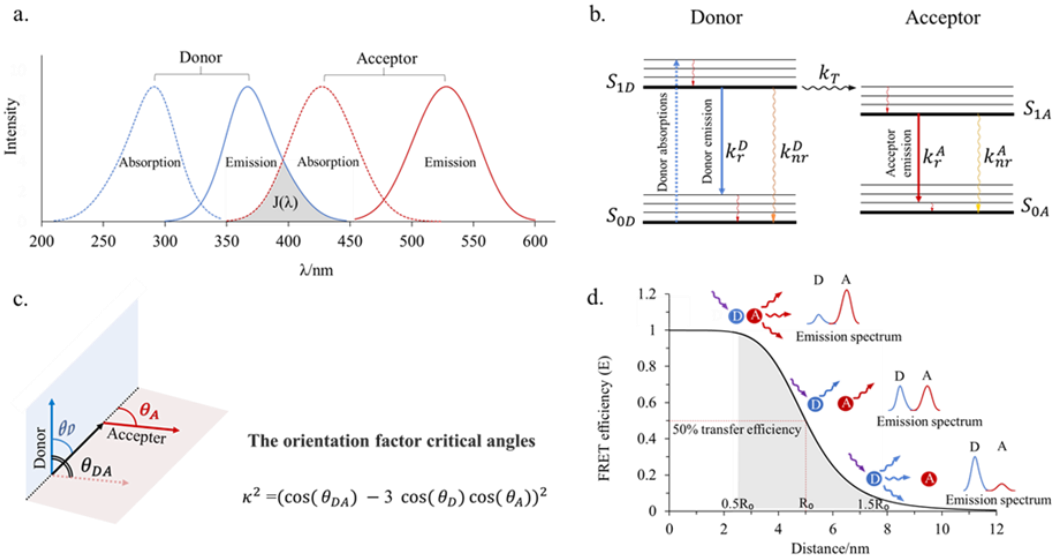


**Figure 8.** (a) An example of a FRET-Pair system where the emission spectrum of the donor overlaps the absorption spectrum of the acceptor. (b) Jablonski Diagram showing the effect of FRET. (c) schematic showing the donor (blue) and acceptor (red) dipoles, the separation vector (black) and the critical angles  $\theta_D$ ,  $\theta_A$  and  $\theta_{DA}$  used in the definition of the orientation factor  $\kappa$ . (d) Plot showing the dependence of FRET efficiency on the distance between donor (blue) and acceptor (red).

The extent of FRET is highly affected by the degree of spectral overlap between the donor's emission and the acceptor's absorption, and the distance ( $r$ ) between the donor-acceptor pair<sup>115</sup>. Thus, the rate of energy transfer  $k_T$  (Figure 8b) is expressed as a function of the distance  $r$

$$k_T(r) = \frac{1}{\tau_D} \left( \frac{R_0}{r} \right)^6 \quad 19$$

Where  $\tau_D$  is the donor's lifetime in the absence of acceptor and  $R_0$  is the Forster distance, which depends on the overlap integral ( $J$ ) of the donor emission spectrum

with the acceptor absorption spectrum (Figure 8a) and the relative orientation of the donor emission dipole moment and the acceptor absorption dipole moment (Figure 8c)<sup>115</sup>

$$R_0^6 = \frac{9000 \ln(10)}{128 \pi^5 N_A} \frac{\kappa^2 Q_D}{n^4} J \quad 20$$

$$J = \frac{\int f_D(\lambda) \epsilon_A(\lambda) \lambda^4 d\lambda}{\int f_D(\lambda) d\lambda} \quad 21$$

Where  $N_A$  is Avogadro's number,  $\kappa$  is the dipole orientation factor,  $Q_D$  is the donor's fluorescence quantum yield in the absence of the acceptor,  $n$  is the refractive index of the medium,  $f_D(\lambda)$  is the donor emission spectrum and  $\epsilon_A$  is the molar extinction coefficient of the acceptor.

If  $\lambda$  is expressed in cm and  $J(\lambda)$  is in units of  $M^{-1} \text{ cm}^3$ ,

$$R_0 = 9.78 \times 10^3 \left( \frac{\kappa^2 Q_D}{n^4} J \right)^{\frac{1}{6}} \quad \text{in } (\text{\AA})$$

The efficiency of FRET ( $E$ ) is inversely proportional to the sixth power of the distance between donor and acceptor due to the dipole–dipole coupling mechanism<sup>115</sup>, and can be expressed in the form

$$E = \frac{R_0^6}{R_0^6 + r^6} \quad 22$$

$R_0$  is considered the distance at which the energy transfer efficiency is 50%. Figure (8d) shows how FRET efficiency decreases with the sixth power of the donor-acceptor separation. Therefore, it is commonly used as a research tool for measuring Angstrom-scale distances. The useful range for measuring FRET, however, is indicated by the grey shaded region in Figure (8d) with limits of  $0.5R_0$  and  $1.5R_0$ . Thus, FRET can be effectively used as a nano-scale ruler for those distances near the Förster distance.

### 3.2.5. Anisotropy

Fluorescence anisotropy ( $r$ ) is a measure of the extent of molecular rotation during the period between absorption and emission. It generally relies on selectively exciting a subpopulation of fluorophores with polarized light and monitoring polarized emission (Figure 9a). Fluorophores in suspension absorb polarised photons with  $\text{Cos}^2\alpha$  probability where  $\alpha$  is the angle between the fluorophore's absorption transition moment and the electric vector of the electromagnetic wave of excitation.

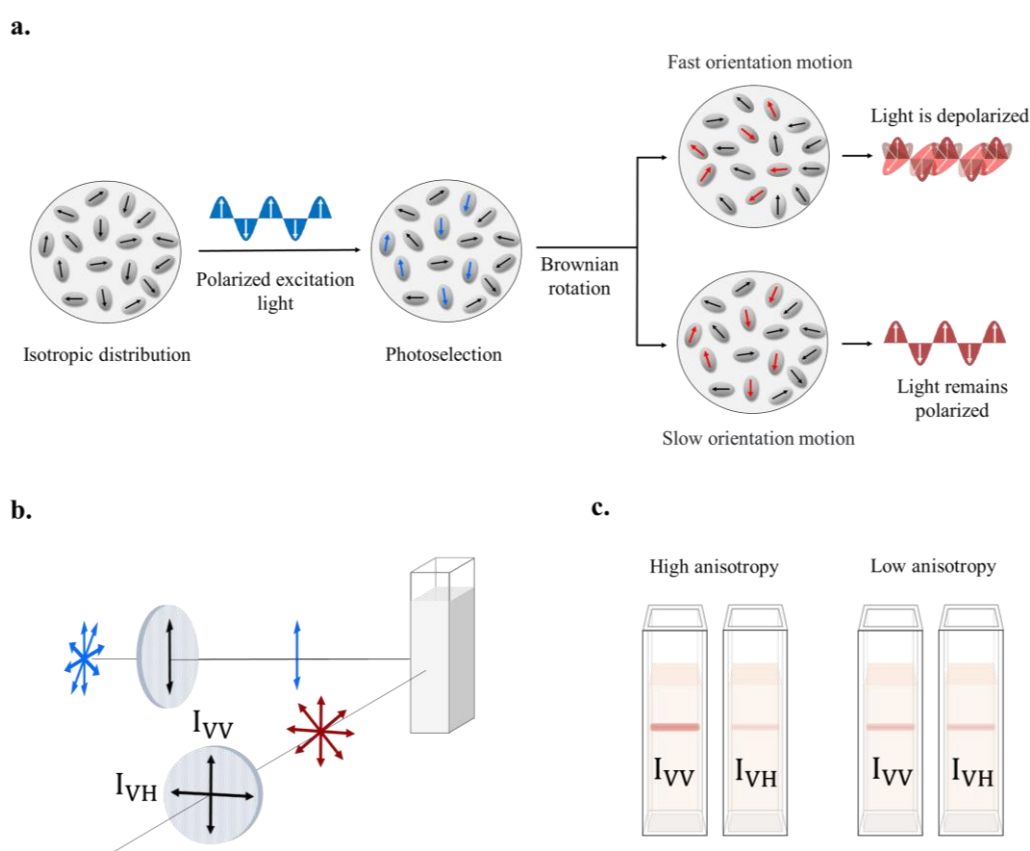


**Figure 9** a) Depiction showing how Polarized excitation selectively excites dipole-aligned fluorophores. Excited molecules which rotate quickly emit light in a depolarized manner whereas particles with slow rotation emit polarized light. b) Illustration of fluorescence anisotropy experiment using excitation and emission polarizers. c) Depiction showing the difference between  $I_{VV}$  and  $I_{VH}$  at high and low anisotropy.

The excited population of fluorophores will then emit fluorescence. Depending on how fast the fluorophore is rotating in solution, a proportion of the emitted

fluorescence will remain polarized with respect to the excitation source. The slower the rotational diffusion, the more the emitted light retains the incoming polarization. The faster the rotational diffusion, the more depolarized the emitted light will be (Figure 9a).

A standard anisotropy measurement is taken by placing a polarizer in the excitation light path and another in the emission light path of a fluorometer (Figure 9b). The excitation light is typically polarized along the vertical axis and the emission intensity is measured in both the vertical ( $I_{VV}$ ) and horizontal ( $I_{VH}$ ) planes (Figure 9b, c).  $I_{VV}$  and  $I_{VH}$  are then used to calculate the anisotropy ( $r$ ) using the following equation:

$$r = \frac{I_{VV} - I_{VH}}{I_{VV} + 2I_{VH}} \quad 23$$

In steady-state anisotropy measurements, continuous illumination is used to measure intensities  $I_{VV}$  and  $I_{VH}$  and an average anisotropy value  $\bar{r}$  is derived from equation (23) opposed to an anisotropy decay  $r(t)$ . In time-resolved anisotropy, intensity decays  $I_{VV}(t)$  and  $I_{VH}(t)$  are used instead to calculate the anisotropy decay  $r(t)$

$$r(t) = \frac{I_{VV}(t) - I_{VH}(t)}{I_{VV}(t) + 2I_{VH}(t)} \quad 24$$

Taking the simplest case of a spherical particle, which displays a single decay time  $\tau$ , the intensity  $I(t)$  and anisotropy  $r(t)$  decays are given by

$$I(t) = I_0 e^{-t/\tau} \quad 25$$

$$r(t) = r_0 e^{-t/\tau_c} \quad 26$$

where  $\tau_c$  is the rotational correlation time,  $I_0$  is intensity at  $t = 0$  directly after excitation and  $r_0$  is anisotropy in the absence of depolarization processes such as energy transfer and rotational diffusion.  $r_0$  has a maximum theoretical value of 0.4 when the excitation

and emission dipoles are parallel and a minimum value of -0.2 when the excitation and emission dipoles are perpendicular according to the equation.

$$r_0 = \frac{2}{5} \left( \frac{3 \cos 2\beta - 1}{2} \right) \quad 27$$

where  $\beta$  is the angle between the excitation and emission dipoles.

In this particular simple case steady state anisotropy  $\bar{r}$  can be determined by the average of  $r(t)$  weighted by  $I(t)$ :

$$\bar{r} = \frac{\int_0^{\infty} r(t) I(t) dt}{\int_0^{\infty} I(t)} \quad 28$$

Measuring steady-state anisotropy is simple. However, the time-resolved method provides additional information that can't be measured directly by steady-state anisotropy such as the values of  $r_0$  and  $\tau_c$  as well as the fluorophores lifetime.

The rotational correlation time  $\tau_c$  is related to the average molecular rotational diffusion coefficient,  $D_r$ , and in the simplest case of a spherical particle to the hydrodynamic molecular volume of the fluorophore,  $V$ , and the local viscosity,  $\eta$ , by the equation:

$$\tau_c = \frac{1}{6D_r} = \frac{V\eta}{TK} \quad 29$$

Where  $T$  is the absolute temperature and  $K$  is the Boltzman's constant. Hence, from time-resolved anisotropy one can obtain information about the fluidity of the medium or the size of the molecules in it.

### 3.3. Intrinsic protein fluorophores

Intrinsic protein fluorescence arises from three amino acid residues with aromatic side chains: tryptophan (Trp), tyrosine (Tyr), and phenylalanine (Phe) (Figure 10). The indole group in the trp residue is the strongest source of ultraviolet absorbance and emission in proteins<sup>122</sup>. The quantum yield of Tyr, however, is quite similar to Trp<sup>112</sup>, yet it has a much narrowly distributed emission spectrum (Figure 10).

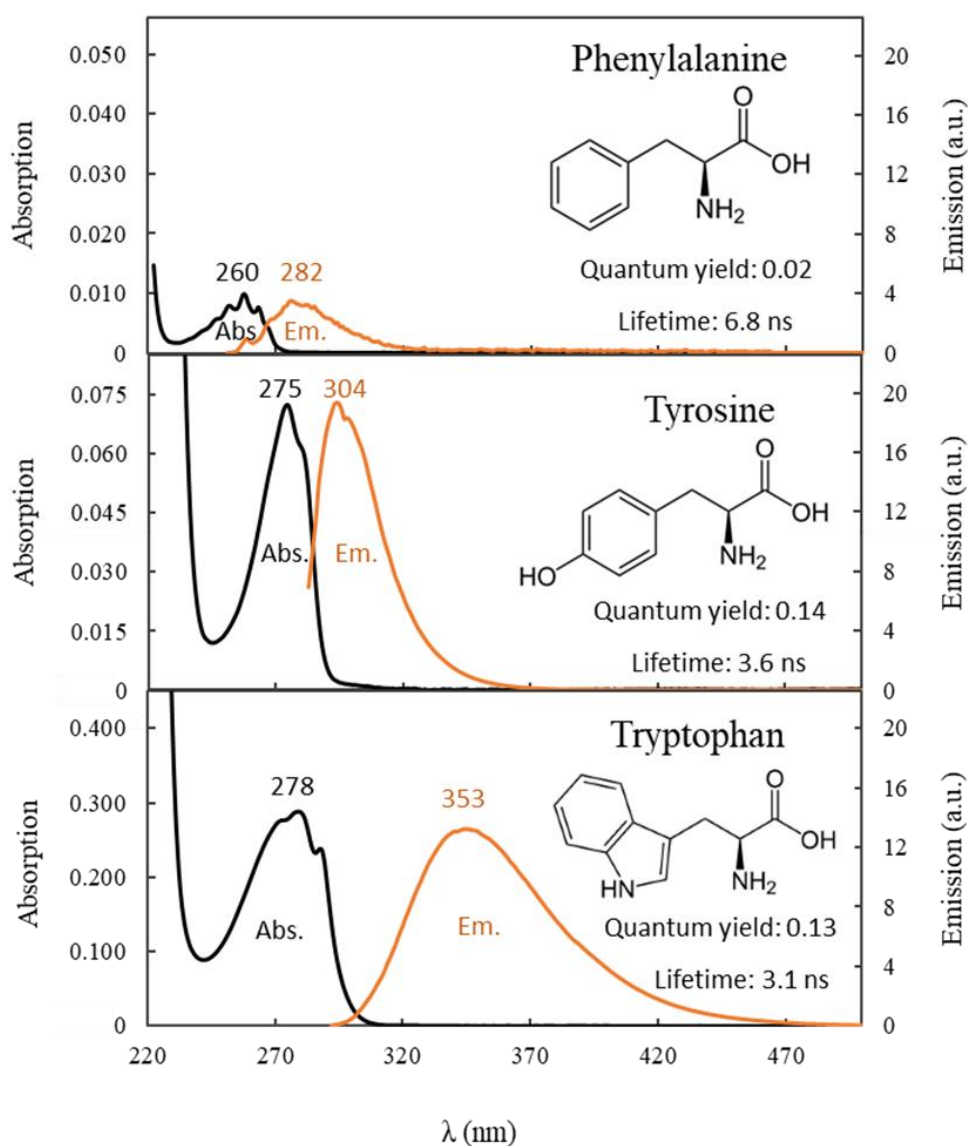


**Figure 10.** Absorption (Black) and emission (Red) spectrum of intrinsic fluorophores: Phe (50  $\mu$ M), Tyr (50  $\mu$ M) and Trp (50  $\mu$ M) in water together with the quantum yield<sup>112</sup>, lifetime<sup>112</sup>, and chemical structure of each fluorophore.

Emission of Tyr in native proteins is commonly quenched due to energy transfer to Trp or interactions with the peptide chain, i.e., ionization of Tyr by nearby carboxyl or amino groups<sup>112</sup>. As for the Phe residue, it is almost never used experimentally because it has a very low quantum yield<sup>112</sup> and it can only be observed if the protein sample lacks Tyr and Trp residues.

The emission of an intrinsic fluorophore is highly sensitive to its local environment. Therefore, intrinsic fluorophores are often used for detection of protein conformational changes<sup>122</sup>.

### **3.4. Complexity of intrinsic fluorescence kinetics**

Protein intrinsic fluorescence carries a variety of information on protein conformation. But protein intrinsic fluorophores usually exhibit complex fluorescence decay kinetics, such complexity hindering any straightforward interpretation of time-resolved fluorescence data. Decades of effort have been devoted to explain the multifarious decay of single intrinsic fluorophores in heterogeneous environments. As a result, two dominating models have been proposed for this purpose: the model of dielectric relaxation and the rotamer model.

The rotamer model contends that fluorophores may exist in various ground-state conformations (rotamers). In proteins, rotamers describe the different conformations of an amino acid side-chain based on the rotational isomers. Because different rotamers have different rates and paths of depopulation of the excited state due to their individual spatial arrangements, they usually display distinct decay times. Thus, individual components of a multi-exponential decay of an intrinsic protein-fluorophore are merely attributed to the presence of individual rotamers<sup>123–126</sup>.

In contrast, the dielectric relaxation model attributes the complexity of the decay to a single fluorophore conformation surrounded by an environment exhibiting dielectric relaxation as a response to the rapid increase in the fluorophore's dipole moment upon electronic excitation. Because the rate of dielectric relaxation is comparable to the rate of depopulation of the excited-state, in this particular case, the spectrum will exhibit a measurable time-dependent red-shift. As a result fluorescence intensity decays measured at short-wave lengths of the spectrum would require an extra component with a short lifetime to signify the loss in fluorescence intensity. Conversely, when decays are measured at long-wavelengths, an increasing component (i.e. an exponential component with negative amplitude) is added to represent the increase in fluorescence intensity caused by emission spectral shift<sup>112,127</sup>.

One of the most common observations in fluorescence intensity decay measurements of protein intrinsic fluorophores is the lifetime-wavelength correlation. That is, the mean decay times increase with increasing detection wavelength. This lifetime-wavelength correlation can be easily explained by the relaxation model and is commonly used against the rotamer model. However, some studies<sup>128</sup> suggest that such correlation can be explained within the rotamer model by demonstrating that rotamers emitting at short-wavelengths are more likely to be involved in charge transfer, hence have shorter lifetimes. The validity of the relaxation model has also been questioned due to the absence of frequent appearance of negative amplitudes in protein decays.

This uncertainty surrounding the interpretation of protein autofluorescence has hindered the development of protein fluorescence lifetime-based techniques and its applications. In our approach we assume that both dielectric relaxation and depopulation of the excited states can occur simultaneously, which provokes the need to distinguish the effect of relaxation on fluorescence emission from heterogeneity.

Previous research<sup>129</sup> suggests that relaxation and heterogeneity can be distinguished from each other by a quantitative model of fluorescence during homogeneous electrostatic relaxation. The proposed model characterises the time variation of the fluorescence intensity obtained at fixed wavelengths and the evolution of the instantaneous spectrum. However, the situation becomes more complicated when studying protein aggregation because distinguishing between dielectric relaxation and heterogeneity (rotamers) is not the only problem. Added to that is the problem of assembly, which is naturally associated with the appearance of multiple oligomers increasing the heterogeneity of the sample.

## **4. Steady-state and time-resolved fluorescence measurements**

Fluorescence is a phenomenon that can be described by a number of parameters such as excitation and emission wavelengths, intensity, polarisation, quantum yield, lifetime and position in x, y and z. Hence, the objective of a fluorescence measurement is to obtain information about as many parameters as possible. In practice, multiple instruments are typically needed to measure different fluorescence parameters. Fluorescence measurements can be generally categorized into two main types: steady-state and time-resolved measurements. Here we describe in detail the fluorescence measurement techniques used in this study.

### **4.1. Steady-state measurements**

The steady-state technique (Figure 11) typically involves the use of a continuous beam of light for illumination. A Xenon arc lamp is often used because it provides a wide spectrum for excitation ranging from the ultraviolet to the near-infrared. The beam of light produced by the source can be then filtered by an excitation monochromator that allows a narrow band of wavelengths of the electromagnetic radiation to pass through to the sample. In the sample-compartment the sample absorbs the incoming light and emits fluorescence. The resulting emission is then filtered by the emission monochromator, which transmits specific wavelengths to the photomultiplier detector. The general principle of operation of a photomultiplier is to convert incident photons into electrons according to the photoelectric effect by means of an opaque or semi-transparent photocathode. Photoelectrons are then multiplied by a dynode structure, based on the process of secondary emission, to provide a measurable electric current signal at the output. All components of the instrument (i.e. spectrofluorometer) are connected to a controller, which transfers information to and from the host computer.

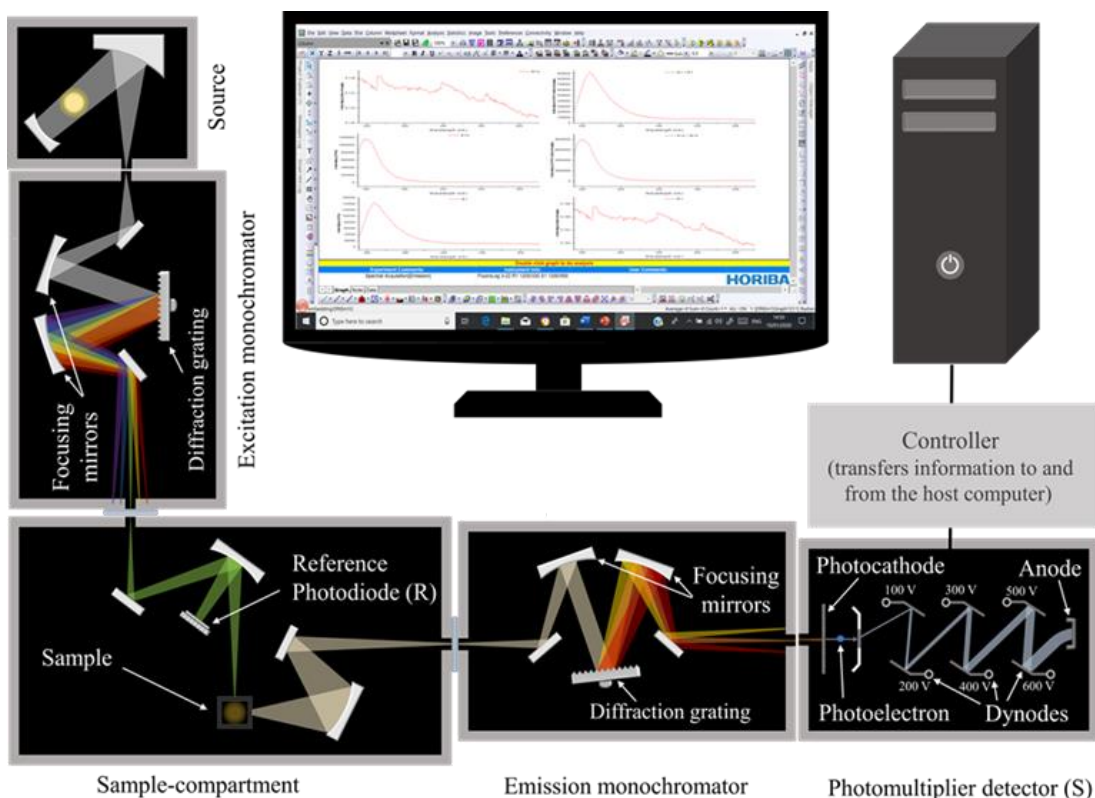


**Figure 11.** Schematic diagram of a typical Emission Spectrometer apparatus setup

The emission spectrum of the sample is obtained by setting the wavelength of the excitation monochromator to a wavelength that the sample is known to well absorb, the wavelength of the emission monochromator is scanned across a range of emission wavelengths and the intensity of the fluorescence is recorded on the detector as a function of emission wavelength. The excitation spectrum, on the other hand, is obtained by fixing the emission wavelength to a known fluorescence emission by the sample, the wavelength of the excitation monochromator is scanned across a chosen excitation range and the intensity of fluorescence is recorded on the detector as a function of excitation wavelength. The excitation spectrum will appear identical to the absorption spectrum as long as the sample obeys Kasha's rule. Nearly all molecules

obey Kasha's rule. However, there are a few exceptions such as azulene which has  $S_2 \rightarrow S_1$  fluorescence emission due to the unusual high energy gap between the  $S_1$  and  $S_2$  singlet states.

## 4.2. Time-resolved fluorescence measurements

Time-resolved fluorescence spectroscopy monitors the emission of a sample as a function of time after a brief excitation pulse (ideally a delta-pulse). Looking at the relationship between time-resolved and steady-state fluorescence, we find that steady-state observations are simply an average of the time-resolved phenomena over the sample's intensity decay<sup>115</sup>. For example, if a sample exhibits a single-exponential intensity decay  $I(t) = I_0 e^{-\frac{t}{\tau}}$  then the steady-state intensity  $I_{ss}$  would be described in the form

$$I_{ss} = \int_0^{\infty} I_0 e^{-\frac{t}{\tau}} dt = I_0 \tau \quad 30$$

$I_0$  depends mostly on the concentration of the fluorophore and some instrumental parameters. Therefore, the steady-state intensity  $I_{ss}$  is considered proportional to the lifetime  $\tau$ . This outcome corresponds with the proportional relationship existing between the fluorophore's quantum yield and lifetime as shown in Equ. 11 and Equ. 12.

The time-resolved measurement technique is relatively complex and expensive in comparison with the steady state technique. But in return fluorescence intensity decays provide important molecular information that are typically lost during the time averaging process. Such information help reveal conformational changes in macromolecules, differentiate between dynamic and static quenching and in the presence of FRET the decays can be used to determine the distribution of accepters around donors.

Time-resolved fluorescence techniques fall broadly into two main groups: frequency-domain and time-domain. In concept, the two techniques are similar but they require different instrumentation and have distinct applications. In the frequency-domain method<sup>130</sup>, the sample is excited with amplitude-modulated light. The frequency of the modulation (typically in the range from 10MHz - 1GHz) is usually comparable to the reciprocal of the lifetime<sup>115</sup>. Electrooptic modulators are often used to modulate light at frequencies of up to 200 MHz<sup>112</sup>. These optical devices are mainly constructed of a material capable of rotating polarized light when an electric field is applied across the material. The modulators are, therefore, placed between two crossed polarizers so that the amount of light transmitted through the system is proportional to the applied electric field. Modulators can be replaced with intrinsically modulated light sources such as pulsed lasers, laser diodes, and light emitting diodes (LEDs) in order to achieve light modulation at GHz frequencies<sup>112</sup>.

The fluorescence emission follows the same modulation with some phase delay and a smaller amplitude as shown in figure (12, a). The lifetime of the sample  $\tau$  can be determined from the phase angle shift between the excitation and emission ( $\Phi$ ) or the amplitude ratio between the excitation and emission amplitudes of the modulation ( $m$ )<sup>130</sup> (Figure 12a).

For a single-exponential emitter<sup>115</sup> the lifetime  $\tau$  is given by:

$$\tau = \frac{1}{\omega} \tan \Phi \quad 31$$

Or

$$\tau = \frac{1}{\omega} \sqrt{\frac{1}{m^2} - 1} \quad 32$$

Where  $\omega$  is the modulation frequency in radians/s. However, for a mixture of fluorescent components, the separate lifetime parameters are usually recovered by scanning over a range of frequencies to achieve statistical significance.

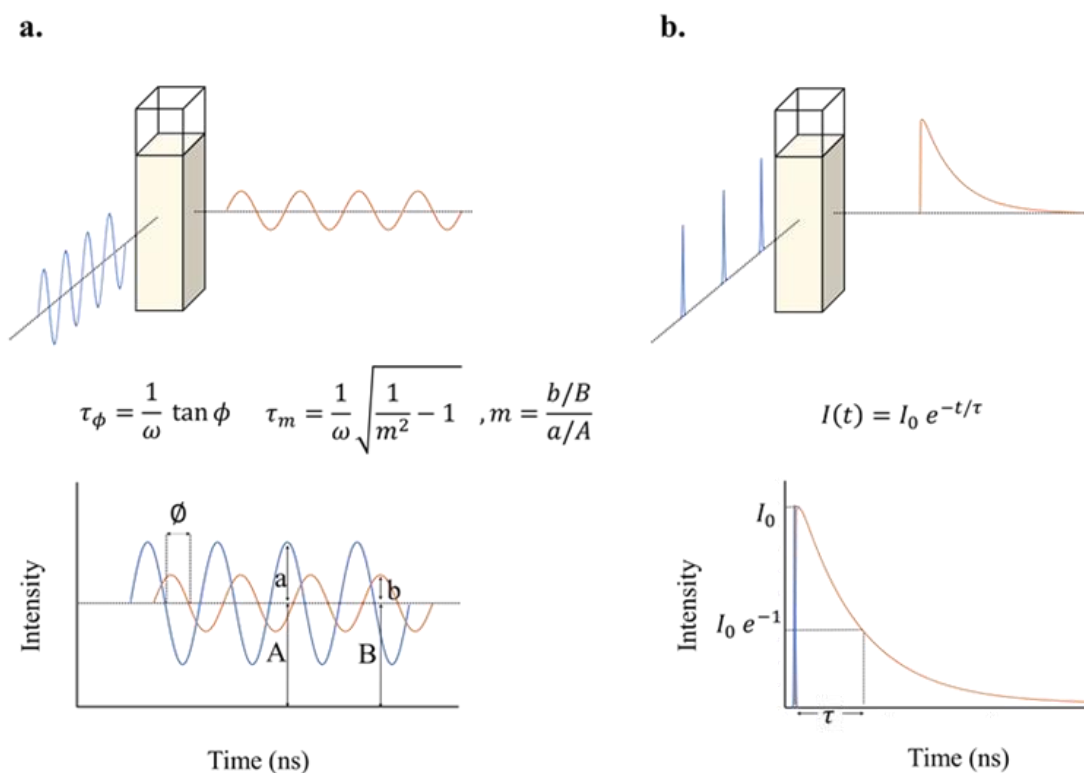


**Figure 12.** Scheme of (a) the frequency-domain fluorescence lifetime technique showing the Differential phase angle between excitation and emission  $\Phi$  and the calculation of the amplitude ratio between the excitation and emission amplitudes  $m$ . (b) the time-domain fluorescence lifetime technique.

The frequency-domain technique is probably the oldest among time-resolved fluorescence techniques. Despite its age, it allows accurate measurements of extremely short fluorescence lifetimes of a few picoseconds<sup>131</sup> with a continuous excitation source, tuneable from the UV to the near-IR. In contrast to time-domain measurements, the frequency-domain method is relatively fast and mostly effective in cases where there is a high signal-to-noise ratio. The frequency-domain technique, however, is only efficient for exponential and multi-exponential decays due to the relatively simple formula linking measurables with the decay model parameters. When the fluorescence intensity

decay is other than exponential, the use of this technique is not practical. And in cases where the emission signal is too weak the time-domain method becomes favourable<sup>132</sup>.

The time-domain fluorescence technique, on the other hand, is conducted by exposing the sample to an ultrashort pulse of light whose time duration is significantly shorter than the sample's decay time (Figure 12b). The sample's fluorescence intensity decay is recorded by a high-speed detection system capable of measuring intensity or anisotropy on the nano-second timescale.

The measured fluorescence decay,  $F(t)$ , does not usually represent the true decay of the sample,  $R(t)$ , unless the excitation light pulse is infinitely narrow ( $\delta$ -pulse) and the response of the detection system is infinitely fast.

In practice, both the excitation pulse and the detector response are relatively broad, which means that the instrumental response of the system (i.e. the source, detector, and electronics),  $I(t)$ , is inevitably convolved with the decay function  $R(t)$ . The assumed  $R(t)$  is regarded as the response of the fluorescent system to the delta-type excitation and is given in the form of analytical formula characterised by a number of decay parameters. To recover the decay parameters, one must apply the re-convolution analysis. Re-convolution treats the excitation pulse as a chain of  $\delta$ -pulses of amplitudes  $I(t')$  at any given time  $t'$  (Figure 13a, b), so that the observed decay  $F(t)$  is a convolution integral, i.e. the sum of the decays from all  $\delta$ -pulses initiated during the duration of the excitation pulse (Figure 13c).

$$F(t) = I(t) \otimes R(t) = \int_0^t I(t') R(t - t') dt' \quad 33$$

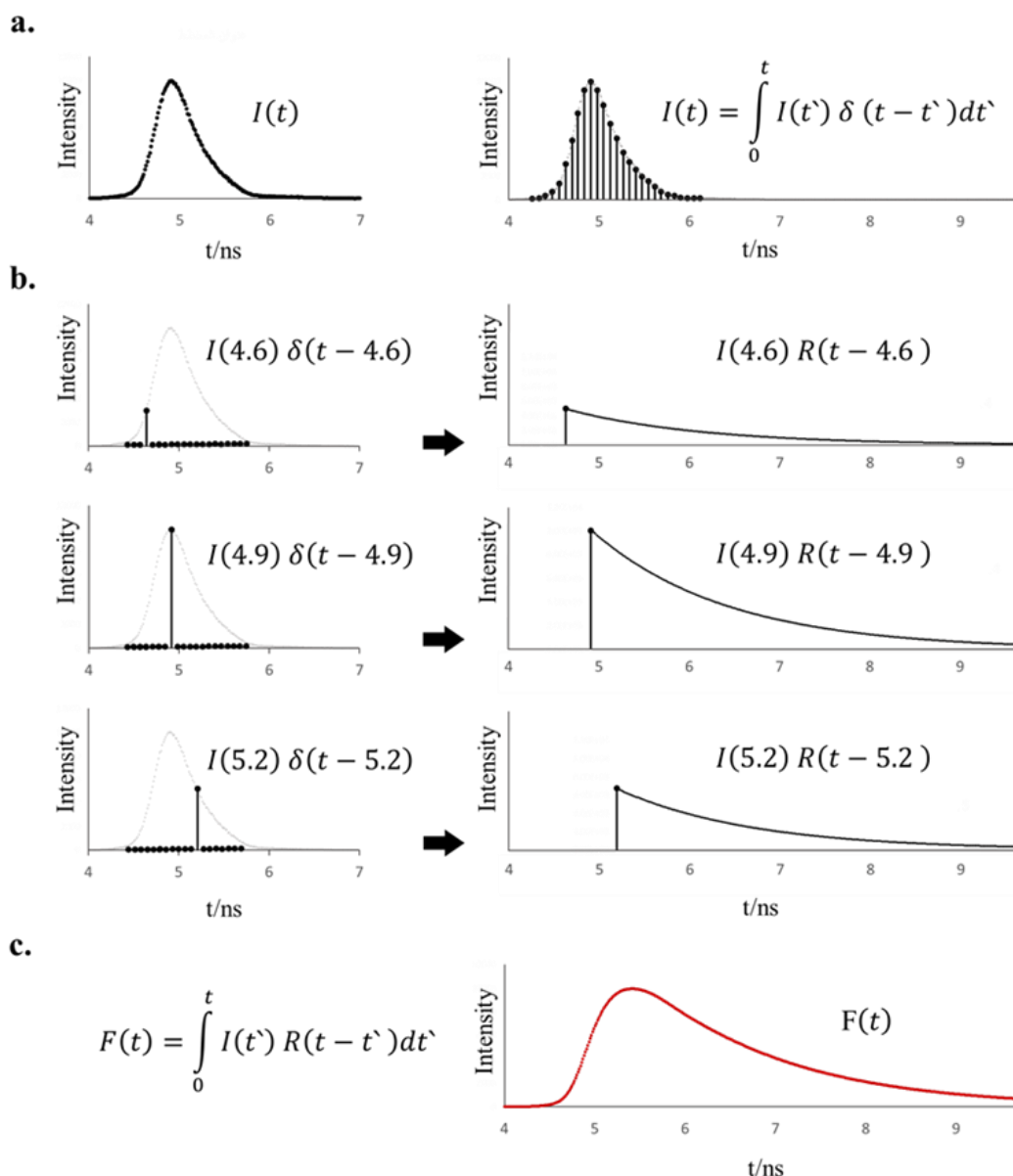


**Figure 13.** (a) Example of an instrumental response  $I(t)$  measured using a scattering solution with the emission monochromator set to the same wavelength of the excitation source 295 nm.  $I(t)$  can be expressed as a continuous sum of weighted Dirac delta functions. (b)  $\delta$ -pulses of amplitudes  $I(t')$  at three given times  $t'=4.6, 4.9$  and  $5.2$  ns and their corresponding fluorescence intensity decays. (c) Fluorescence intensity decay measured for 2,5-Diphenyloxazole (PPO) at excitation 295 nm and emission 359 nm., which represents the impulse response of the sample  $R(t-t')$ , convoluted by the instrument response  $I(t')$ .

In practice, the instrumental response function  $I(t)$  is usually measured from scattered excitation light.  $I(t)$  is then re-convoluted with an assumed fluorescence impulse response  $R(t)$  and compared with the measured fluorescence decay  $F(t)$  by a statistical goodness of fit criterion, e.g. a chi-squared test. This type of analysis strongly depends

on choosing the appropriate theoretical model for  $R(t)$  to be fitted to the measured data. Typically, a sum of 1, 2, ...,  $N$  exponentials with pre-exponential factors and decay times is assumed to describe  $R(t)$ , and the simplest model satisfying the goodness-of-fit criteria is regarded as the correct model.

#### 4.2.1. The time-correlated single-photon counting method

The most common technique used to record time-domain data is the method of Time-correlated single-photon counting (TCSPC)<sup>133</sup>. Figure 14 shows a schematic diagram of a TCSPC set-up.

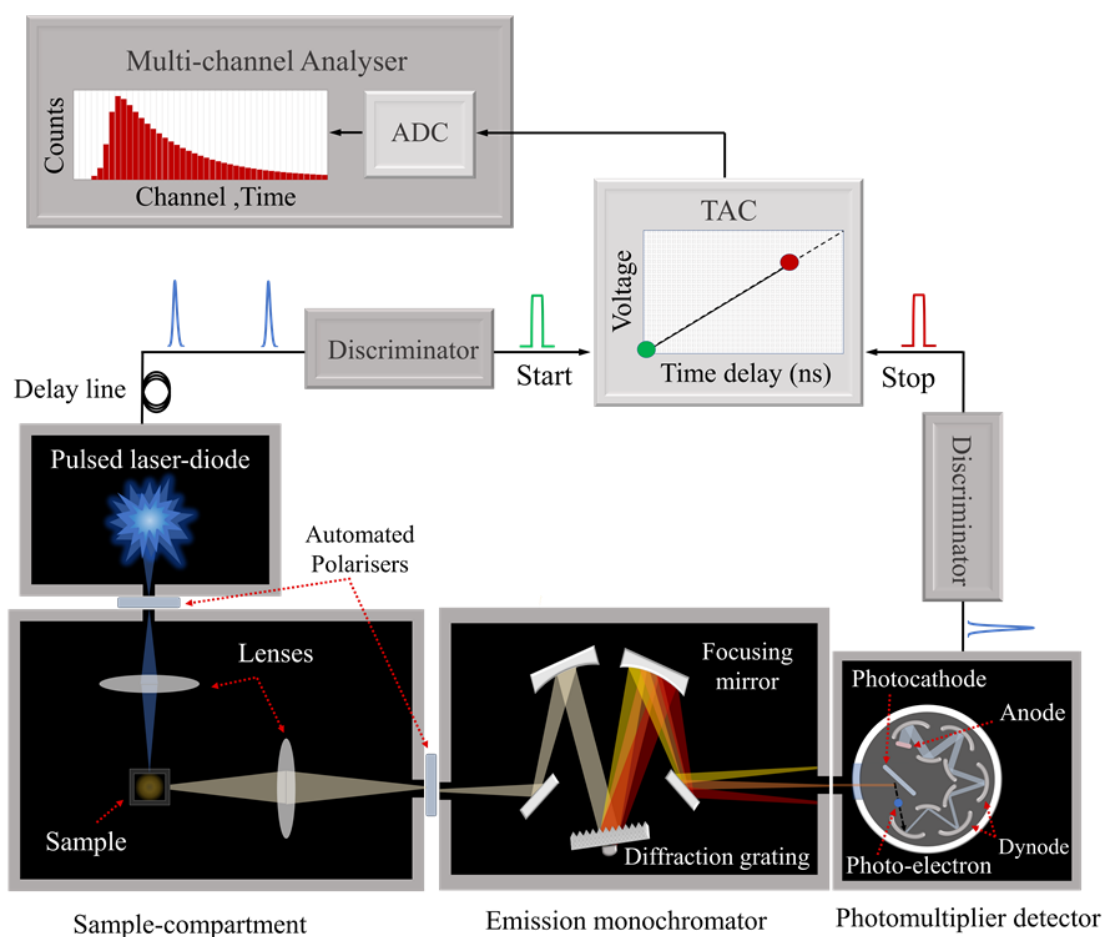


**Figure 14.** Typical Experimental setup for TCSPC based techniques

The instrumentation needed for this technique includes<sup>134</sup>:

- a) a short pulse width excitation source (i.e. pulsed laser diodes with optical pulses as short as 70ps) with a relatively high pulse repetition rate (ranging from 10KHz to 1MHz).
- b) Optical components of a typical spectrometer: Monochromators, collection and focusing optics and polarisers
- c) A single-photon detector
- d) Timing electronics, namely a time to amplitude converter (TAC), a multichannel analyser (MCA) and discriminators

The pulsed excitation source generates a flash of light that is partially used to excite the sample. The subsequent fluorescence emission is detected at a right-angle orientation to separate it from excitation. Emission can be filtered by an emission monochromator allowing single wavelengths of the electromagnetic spectrum to reach the single photon detector. The most common type of detectors employed in fluorescence lifetime determination by the TCSPC technique is the Photomultiplier tube (PMT)<sup>134</sup>. It allows detection of light at the single-photon level. The flash produced by the excitation source generates an electronic signal that can be used as a start impulse for a time-to-amplitude converter (TAC).

When the TAC is activated by the start signal, it begins to build voltage across a capacitor until it receives the stop pulse, generated from the detector side of the instrument by a constant fraction discriminator, or until it completes its sweep. Subsequently an analog output pulse will be generated as a result of discharging the capacitor. The amplitude of this output pulse is proportional to the measured time between the start and stop pulses. The analog output is then digitized by an analog-to-

digital converter and sent to a MCA, which records these repetitive start-stop signals to generate a histogram of photon counts as a function of time-channel units.

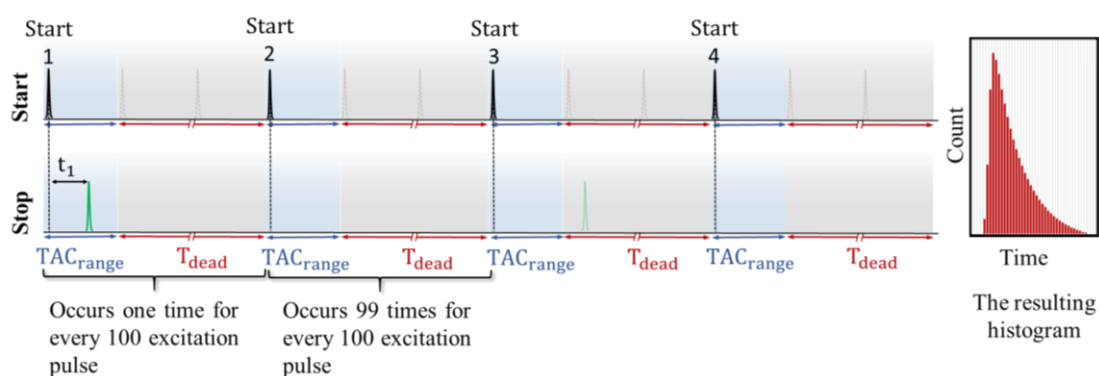
One infamous artifact in TCSPC is photon pile-up<sup>133</sup>. This effect results from the fact that a TCSPC device can detect only one photon per signal period. Therefore, at high photon detection rates only the first photon is being timed. All subsequent photons are ignored because the TAC is busy analyzing the first photon event within the same period, which leads to the shortening of the measured fluorescence lifetimes. To avoid the pile-up effect, one must keep the photon count rate below or around 1% of the laser repetition rate.

In TCSPC applications there are two different operating modes: The forward mode and the reverse mode. In the forward mode, the pulse rate from the light source is connected to the start input of the TAC and the pulses from the detector are connected to the STOP input. Good collection statistics require that the rate of the equally-spaced pulses generated by the light source are substantially higher than the rate of the random pulses coming from the detector (Fig. 15).

Consequently, the vast majority of the TAC cycles will be started by the start pulse but never stopped by the stop signal, and would require reset at overflow. The reset process takes about  $1\mu\text{s}$  and that keeps the electronics busy 20 times more than the actual time needed. For example, if the photon count rate is 1% of the laser repetition rate and the measurement time range is 50 ns, then the time it would take to record a single photon would be  $100 \times 50\text{ns} + 100 \times 1\mu\text{s} \approx 0.11\text{ ms}$ . In the reverse mode, the low rate signal coming from the detector is connected to the START input and the high-count rate signal coming from the light source is connected to the STOP input. Thus, in the reverse mode, the time needed to record a single photon is reduced to  $100 \times 50\text{ns} + 1 \times 1\mu\text{s} \approx 6\ \mu\text{s}$ . However, when reverse mode is employed the reference pulses coming from

the excitation source must be shifted by a long delay, so that they reach the TAC input later than the start pulses coming from the detector. This delay is usually set to be slightly longer than the measurement time range. In this case the recorded data will appear reversed in comparison with data recorded in the forward mode (Fig. 15), and can be easily flipped using an acquisition/analysis software.

#### Forward mode



#### Reverse mode

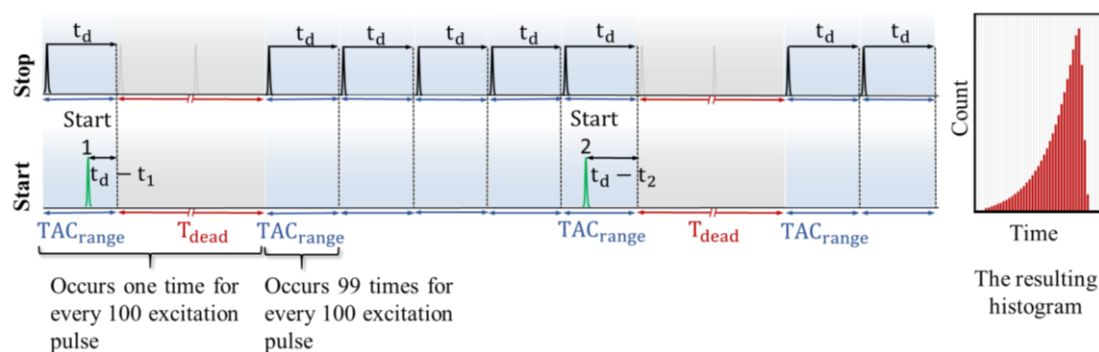


**Figure 15.** Illustration of the forward (above) and reverse (below) operating modes in TCSPC. In this example, the photon count rate is 1% of the laser repetition rate. The time range  $T_{AC\ range}$  and the deadtime of the timing electronics  $T_{dead}$  are constant during measurement. In the forward mode, the time between the start signal, initiated by the excitation source, and the stop signal coming from the detector  $t_1$  is recorded and used to generate a histogram of photon counts as a function of time. In the reverse mode, time is recorded between the start signal coming from the detector and the stop signal coming from the excitation source. In this case the reference pulses coming from the excitation source must be shifted by a long delay  $t_d$ , so that they reach the TAC input later than the start pulses coming from the detector.

TCSPC can be used to measure fluorescence intensity decays and determine their parameters, including lifetimes ranging from several picoseconds to milliseconds and

beyond. The lower limit of the lifetime range,  $\tau_{min}$ , is set by the jitter of the TCSPC electronics, the light source and the detector. In general,  $\tau_{min}$  can be estimated from the equation<sup>135</sup>

$$\tau_{min} = \frac{1}{10} \cdot FWHM_m \quad 34$$

$$FWHM_m = \sqrt{FWHM_{exc}^2 + FWHM_{det}^2 + FWHM_{elec}^2} \quad 35$$

Where  $FWHM_m$  is the instrumental full width at half maximum,  $FWHM_{exc}$  is the optical excitation pulse full width at half maximum,  $FWHM_{det}$  is the detector transit time spread and  $FWHM_{elec}$  is the width of the electronic jitter. The factor 1/10 represents the fact that lifetimes as short as 10% of the instrumental response can be determined by numerical reconvolution.

The upper limit of the lifetime range,  $\tau_{max}$ , is given by the repetition frequency of the pulsed light source,  $f_{exc}$ . Accordingly,  $f_{exc}$  must be adjusted before measurement so that it satisfies the following condition

$$\tau_{max} = \frac{1}{10} \cdot \frac{1}{f_{exc}} \quad 36$$

The upper limit of the lifetime measurement is also influenced by the dark count rate of the detector. As explained previously, the fluorescence collection rate must be less than 2% of the excitation rate. Because noise counts contribute to the fluorescence collection rate, the amount of fluorescence that can be collected will be reduced. Narrowing the time range selected for measurement, which is usually set to be 10-20 times the samples expected lifetime, can help reduce the amount of noise counts contributing to the fluorescence collection rate. Thus, detectors with high dark count

rates will have a narrow TCSPC operating range. For example, consider a detector with 200,000 cps noise, in this case, the longest measurable lifetime would be around 5ns.

#### 4.2.2. Fluorescence decay analysis

Histograms obtained in TCSPC technique can be used to perform the reconvolution of the equation 33, namely establishing the goodness of fit of the assumed model of the decay, and its parameters. A measure of the instrumental response,  $I(t)$ , is needed for this type of analysis and it has to be done to a similar precision as the decay,  $Y(t)$ , (i.e. has the same number of counts in the peak channel).

There are many methods to solve Equation 33. The most widely used method is the nonlinear least squares method, which involves using a quantity  $\chi^2$  as a measure of mis-match between the experimental data  $Y(t)$  and the fitted function  $F(t)$ .  $\chi^2$  can be calculated by the following formula

$$\chi^2 = \sum_N \left[ \frac{Y(i) - F(i)}{\sigma(i)} \right]^2 \quad 37$$

Where  $N$  is the number of data channels selected for analysis,  $Y(i)$  is the fluorescence decay data,  $F(i)$  is the fitted function and  $\sigma(i)$  is the expected deviation from statistical consideration. In photon counting experiments  $\sigma(i)$  is usually estimated from the data using the Poissonian distribution, therefore,  $\sigma(i) \approx \sqrt{Y(i)}$ .

$\chi^2$  is then minimized by varying the parameters of the fitting function. The minimum value of  $\chi^2$  is achieved when the actual deviation between  $Y(i)$  and  $F(i)$  equals the expected deviation. Accordingly,  $\chi^2$  would be nearly equivalent to the number of degrees of freedom,  $v = N-n$ , where  $n$  is the number of fitted parameters. Typically,  $\chi^2$  is normalised so that its value is independent of  $v$

$$\chi_v^2 = \frac{\chi^2}{\nu} \approx 1 \text{ for a good fit} \quad 38$$

Another important criterion used to evaluate the goodness of fit is the random distribution of weighted residuals,  $W_t$ , given by:

$$W_t = \frac{Y(t) - F(t)}{\sqrt{Y(t)}} \quad 39$$

Figure 16 shows an example of fitting three different models to the fluorescence decay of N-Acetytyrosinamide (NAYA). The relatively high chi-square value obtained from fitting data to the single exponential model, as well as the trend observed in the weighted residuals (Figure 16a) indicates that it's not the proper model. The two-exponential model, on the other hand, gives a better chi-square value and shows a random distribution of residuals (Figure 16b), which suggest that it is the appropriate model. Fitting an additional exponential decay component produced no significant improvement (Figure 16c), which confirms that the two-exponential model is indeed the best model describing the data.

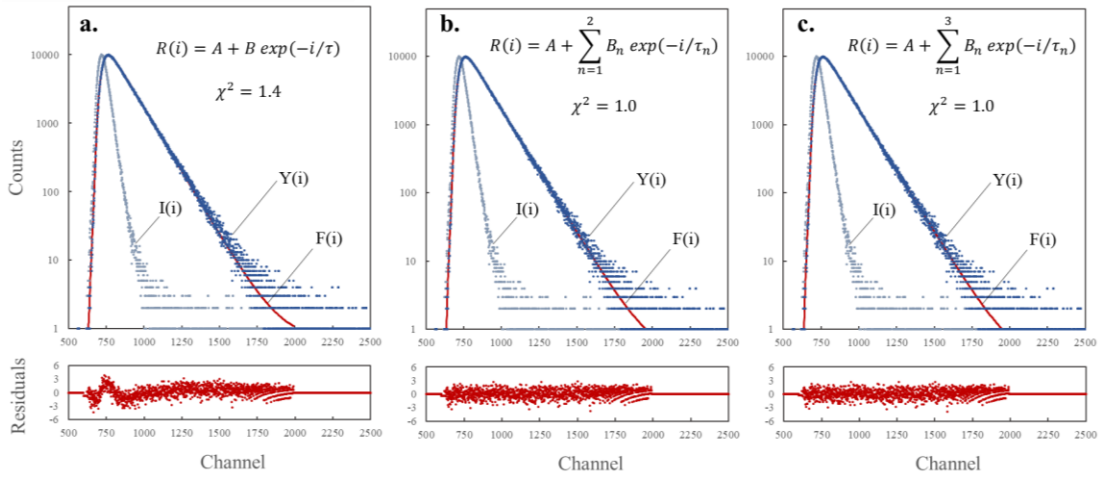


**Figure 16.** The fluorescence intensity decay of NAYA,  $Y(i)$ , obtained from the TCSPC technique, the instrumental response,  $I(i)$ , and the fitted function  $F(i)$ ; a) single exponential, b) two-exponentials, c) three-exponentials.

### 4.3. Time resolved emission spectra (TRES)

Time resolved emission spectra can be collected by using fluorescence intensity decays at different emission wavelengths across the fluorophore's spectrum<sup>136</sup>. The outcome is a 3-D surface that can be sliced perpendicular to the time axis, highlighting the temporal evolution of the fluorescence spectra. This is of great importance, as it allows the study of a wide range of photophysical phenomena associated with excited-state interactions, and relaxation processes<sup>112</sup> or sample heterogeneity. Figure 17a shows an example illustrating how excited-state reactions may affect TRES. In such a case two distinct emitting species are usually observed: emission from the initially excited-state or the Frank-Condon state  $S_{FC}$  and emission occurring from species formed in the excited-state reaction  $S_R$ . The lifetimes  $\tau_{FC}$  and  $\tau_R$  of the states  $S_{FC}$  and  $S_R$  are usually different because emission is occurring from different molecular species. The  $S_{FC}$  and  $S_R$  states may also have different emission spectra because of their different electronic states or chemical structures. In the excited-state reaction model, states  $S_{FC}$  and  $S_R$  are linked by a chemical rate constant  $K_c$ . If  $K_c$  is substantially small relative to the decay rate of the  $S_{FC}$  state, then emission will occur primarily from the  $S_{FC}$  state. In contrast if  $K_c$  is greater than the decay rate of the  $S_{FC}$  state, then emission will occur mostly from the  $S_R$  state. Emission will occur from both states,  $S_{FC}$  and  $S_R$ , if the reaction rate and the decay rate are comparable (Figure 17a)

Emission spectrum might also display a time-dependent shift while retaining the spectral shape (Figure 17b). This behaviour occurs as a result of general solvent effects. In this case emission occurs during the solvent relaxation process, which means that the solvent relaxation rate  $K_s$  and the decay rate  $K$  are comparable. If  $K_s$  is substantially smaller or greater than  $K$ , then emission will be observed from the  $S_{FC}$  or the  $S_R$  state respectively.

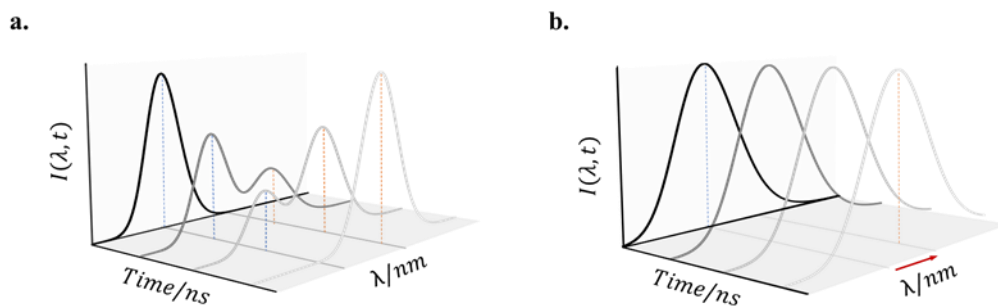


**Figure 17.** Normalized time-resolved emission spectra (TRES) for; a) an excited state reaction, b) a continuous relaxation process.

TRES can also readily identify different species in a heterogeneous sample, even with strongly overlapping spectra, if their lifetimes are different. This is another advantage TRES has over the steady-state method as shown in figure 18.

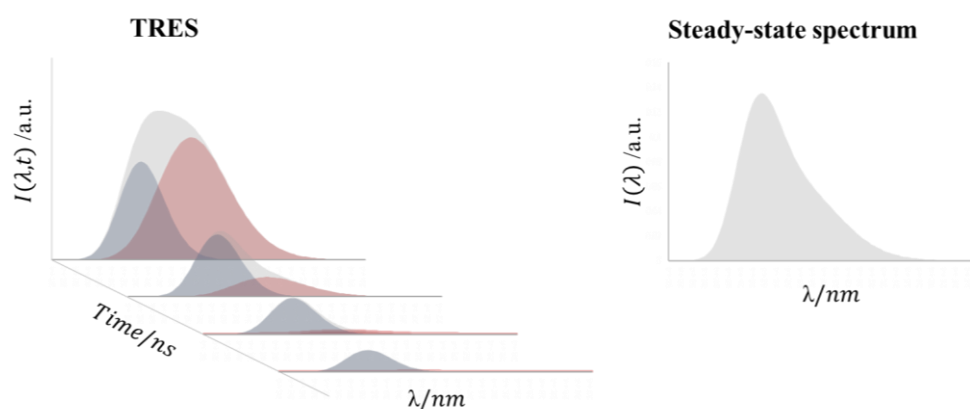


**Figure 18.** The TRES and the steady-state spectrum of a mixture of two fluorescent species with different lifetimes and strong emission overlap.

TRES studies of aggregating structures like proteins, which is the key approach presented in this thesis, may provide more useful information on the kinetics than the traditional fluorescence intensity measurements. It is also challenging, because the studied samples are continuously evolving and are not homogeneous systems. Therefore, it is unlikely that the measured TRES can be interpreted in terms of single mechanisms

like dielectric relaxation, excited-state reaction or the mixture of two independent fluorophores.

The approach used in our study to construct the time-resolved emission spectra is as follows:

- A fixed wavelength is used to excite the A $\beta$ <sub>1-40</sub> sample and both steady-state emission spectrum and fluorescence intensity decays were collected. Steady-state fluorescence spectral measurements were obtained using a Fluorolog-3 spectrofluorometer. The excitation and emission monochromators were set at 5-nm slit widths for a bandpass of 5 nm. Measurements were taken with an excitation wavelength of 279 nm to selectively excite Tyr only, and the emission was monitored over a range of wavelengths in increments of 1 nm at different stages of aggregation. Fluorescence intensity decays were obtained by the standard TCSPC method. TCSPC measurements were conducted on a Horiba Scientific DeltaFlex fluorometer (HORIBA Jobin Yvon IBH Ltd, Glasgow, UK). The system was equipped with Seya-Namioka monochromators with a focal length of 100 mm and a peak transmission efficiency of 62% for excitation and emission. The excitation source used was a HORIBA NanoLED with a centre wavelength of 279 nm, pulse duration of 50 ps and a repetition rate of 1 MHz<sup>137</sup>.
- A series of 10 to 12 fluorescence decay curves were collected at the emission wavelengths between 294 and 330 nm at 3 or 5 nm increments. This chosen wavelength range encompasses the entire emission spectrum of Tyr in A $\beta$  peptides.
- The measured fluorescence intensity decays  $F_{\lambda}(t)$  were analysed by two alternative deconvolution programs. Both capable of coping with the expected scattered light but by different approaches. The first deconvolution software assumes  $n$ -

exponential decay of fluorescence intensity and directly accounts for the presence of scattered excitation light in the Tyr decay (equation 40).

$$F(t) = a + bL(t + \Delta) + c \int_0^t L(t + \Delta - t')I(t')dt' \quad 40$$

where  $L(t)$  is the prompt excitation function,  $a$ ,  $b$ , and  $c$  are the background level, contribution of the scattered light and the scaling parameter, respectively, and  $\Delta$  is the time-shift between the prompt and decay curves due to the wavelength response of the light detector.  $I(t)$  is the multi-exponential model function. Figure (19 a) shows an example of fluorescence intensity decays processed by this deconvolution program.

The second software, DAS6 - the commercial HORIBA Scientific software, represents the scattered light as an additional component with a fixed short lifetime in the  $(n+1)$ -exponential model decay function (Figure 19b).

This step is merely for the purpose of getting a good representation of the decay curves (good  $\chi^2$  values and random residuals). Because it is unlikely that changes in lifetimes and pre-exponential factors can adequately explain the underlying kinetics of complex fluorescent systems, where several processes affecting excited-state kinetics (like variable tyrosine local environments and/or dielectric relaxation) may be present.

- The fitted multi-exponential functions  $I_\lambda(t)$  are then used to calculate the TRES  $I_t(\lambda)$  using the equation

$$I_t(\lambda) = I_\lambda(t) \times \frac{S(\lambda)}{\int_0^\infty I_\lambda(t)dt} \quad 41$$

where  $S(\lambda)$  is the steady-state fluorescence spectrum, and the integral is proportional to the total photons emitted in the lifetime experiment.

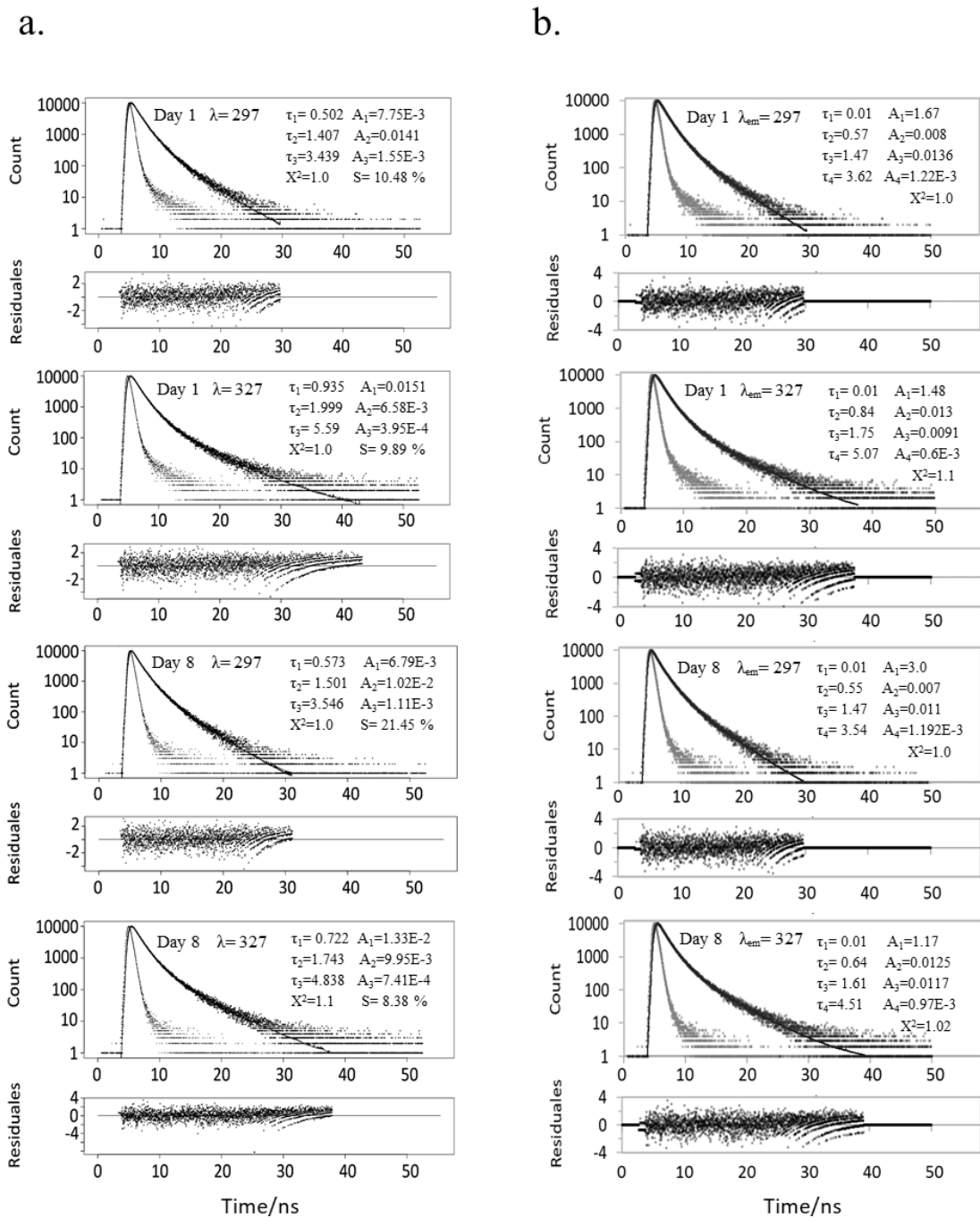


**Figure 19.** Fluorescence decay data of beta-amyloid at detection wave lengths 297 and 327 nm at two stages of aggregation (Day1 and Day 8) analysed by two alternative deconvolution programs; (a) analysis that directly accounts for the presence of scattered excitation light, S, and fits a 3-exponential model to the data.  $\tau_1$ ,  $\tau_2$  and  $\tau_3$  are the decay time constants from the decay fitting, and  $A_1$ ,  $A_2$  and  $A_3$  are the corresponding pre-exponential factors (b) analysis that represents scattered light as an additional component with a fixed short lifetime, thus a 4-exponential model is fitted to data.  $\tau_1$ ,  $\tau_2$ ,  $\tau_3$  and  $\tau_4$  are the decay times, and  $A_1$ ,  $A_2$ ,  $A_3$  and  $A_4$  are the corresponding pre-exponential factors. The goodness of fit is determined by the  $X^2$  value ( $X^2 \approx 1$ ) and the random distribution of weighted residuals.<sup>138</sup>

- The obtained spectra  $I_t(\lambda)$  were then converted from the wavelength to the wavenumber scale according to  $I_t(\nu) = \lambda^2 I_t(\lambda)$ .
- TRES were obtained at several stages of aggregation, namely 1, 5, 24, 48, 72, 96, 142 and 168 hrs after sample preparation (the number indicates the age of the sample when the measurement at the first wavelength has been started). From the data obtained for each stage of aggregation, 14 TRES were calculated at different times after excitation.

#### 4.4. Time-resolved anisotropy

Anisotropy decays  $r(t)$  can be obtained using the TCSPC method by exciting the sample with short pulses of vertically polarized light, and measuring decays of the vertically (VV) and horizontally (VH) polarized emission. The obtained Intensity decays  $I_{VV}(t)$  and  $I_{VH}(t)$  can then be used to calculate  $r(t)$  from equation 24. But due to the potential bias that detectors and monochromators have for one plane of polarisation over another, a grating factor ( $G$ ) is used to correct for the instrument's differential transmission of the two orthogonal vector orientations and equation 24 is corrected as follows

$$r(t) = \frac{I_{VV}(t) - G I_{VH}(t)}{I_{VV}(t) + 2G I_{VH}(t)} \quad 42$$

the G-factor is obtained from the ratio of the perpendicular (HV) and the parallel (HH) polarized emission components when the excitation light is polarized in the horizontal plane

$$G = \frac{\int I_{HV}(t) dt}{\int I_{HH}(t) dt} \quad 43$$

Most of the laser output is blocked when the excitation polarizer is in the horizontal position, thus measuring the G-factor could be very time-consuming. However, G is only a number and the peak counts of  $I_{HV}(t)$  and  $I_{HH}(t)$  are sufficient at about 1000 counts.  $I_{VV}(t)$  and  $I_{VH}(t)$  measurements are achieved by holding the excitation polarizer at the vertical position. the emission polarizer, on the other hand, is toggled between vertical and horizontal for a specified dwell time (60 sec) until a peak difference of 10000 counts is reached

Anisotropy data analysis typically begins with calculating the sum,  $S(t)$ , and difference,  $D(t)$ , curves from the experimental data

$$S(t) = I_{VV}(t) + 2G I_{VH}(t) \quad 44$$

$$D(t) = I_{VV}(t) - G I_{VH}(t) \quad 45$$

Then a reconvolution analysis as described in section 4.2.1 is applied on the total fluorescence intensity  $S(t)$ , yielding the fluorescence decay parameters. Once a suitable fit to the sum data is found, a second reconvolution analysis is carried out to recover  $r(t)$

$$D(t) = S(t) \otimes r(t) \quad 46$$

The model provided for  $r(t)$  by the deconvolution software (HORIBA Scientific DAS 6.8.14) assumes a simple spherical shape for all species and a maximum two rotational correlation times

$$r(t) = b_1 e^{-t/\tau_{c1}} + b_2 e^{-t/\tau_{c2}} + r_{\infty} \quad 47$$

Where  $b_1$  and  $b_2$  are fractional contributions of the rotational correlation times  $\tau_{c1}$  and  $\tau_{c2}$  respectively, and  $r_\infty$  is the residual anisotropy. Values of  $r_\infty$  greater than zero indicate that the angular range of rotational motion of the fluorophore is restricted.  $r_0$  can be determined from the values  $b_1$  and  $b_2$  by:  $r_0 = b_1 + b_2$ .

## 5. Sample preparation

### 5.1. Buffer solutions

- a. Phosphate-Buffered Saline (PBS; Sigma-Aldrich, USA): One tablet of PBS was dissolved in deionized water (200 mL) to yield 0.01 M phosphate buffer, 0.0027 M potassium chloride and 0.137 M sodium chloride, pH 7.4, at 25 °C.
- b. N-2-hydroxyethylpiperazine-N'-2-ethanesulfonic acid (HEPES; Sigma-Aldrich, UK) solution 0.1 M with pH 7.4 at 37 °C. For stability and optimal performance, the buffer solution was stored at temperature 2 to 8 °C and protected from light.

### 5.2. Monomerization of the beta-amyloid peptide ( $A\beta_{1-40}$ )

Re-suspending the lyophilised peptide ( $A\beta_{1-40}$ ; Sigma-Aldrich) was achieved by the treatment in 1,1,1,3,3,3- Hexafluoro-2-Propanol (HFIP; Sigma-Aldrich)<sup>29,139</sup>.  $A\beta_{1-40}$  was diluted in 100% HFIP to 0.1mM and sonicated for at least 10 minutes. The clear solution containing the dissolved peptide was then aliquoted in Eppendorf microcentrifuge tubes and the HFIP was allowed to evaporate inside a fume-hood. For thorough HFIP removal the resulting peptide films were dried under vacuum. The samples were then stored at -20 °C. Based on our experience with  $A\beta_{1-40}$ , we have found that the ratio of monomers to oligomers varies from batch to batch, even if purchased from the same company. Thus, in some cases (see section 9.2, batch 2), a considerable amount of oligomers will remain in the sample even if treated with HFIP.

### 5.3. Preparing $A\beta_{1-40}$ samples for measurements

Aliquots (containing 3.5 nmol of  $A\beta_{1-40}$ ) were allowed to thermally stabilize at room temperature before using.

### **5.3.1. A $\beta$ <sub>1-40</sub> sample:**

A $\beta$ <sub>1-40</sub> films were re-suspended in HEPES or PBS solution. The amyloid suspension was sonicated for around 10 sec. The final concentration of A $\beta$ <sub>1-40</sub> was 50  $\mu$ M and at pH 7.4. The sample was then incubated at temperature 37°C.

### **5.3.2. A $\beta$ <sub>1-40</sub> with copper ions (Cu<sup>2+</sup>):**

The buffered (HEPES, pH 7.4) solution of A $\beta$ <sub>1-40</sub> peptide (50  $\mu$ M) was prepared prior to measurements with three different concentrations of Cu<sup>2+</sup>: 5, 15 and 35  $\mu$ M. Samples were sonicated after adding CuSO<sub>4</sub>·5H<sub>2</sub>O for around 15 sec, but were not subjected to continuous stirring during the experiment. Samples were incubated at temperature 37°C.

### **5.3.3. A $\beta$ <sub>1-40</sub> with glucose:**

A $\beta$ <sub>1-40</sub> films were re-suspended in a buffer (HEPES/ PBS, pH 7.4) solution containing 50 mM Glucose (D-(+)-glucose; Sigma-Aldrich, USA) and sonicated for 15 sec. The amyloid suspension was kept in a micro-cuvette with a volume of ~140  $\mu$ l and was not stirred during the experiment. The sample was incubated at 37°C and all components and solutions were in thermal equilibrium before use.

### **5.3.4. A $\beta$ <sub>1-40</sub> with quercetin:**

A $\beta$ <sub>1-40</sub> films were re-suspended in a buffer (HEPES pH 7.4) solution containing different concentrations of quercetin dihydrate (C<sub>15</sub>H<sub>10</sub>O<sub>7</sub> · 2H<sub>2</sub>O; Riedel-de Haen, Germany) and sonicated for around 10 sec. The final concentration of components in the samples were 50  $\mu$ M A $\beta$ <sub>1-40</sub> and 15 or 50  $\mu$ M Quercetin.

### **5.3.5. A $\beta$ <sub>1-40</sub> with Thioflavin T (ThT)**

For the Thioflavin T assay, A $\beta$ <sub>1-40</sub> films were re-suspended in a buffer (HEPES pH 7.4) solution containing Thioflavin T (Th T; Sigma-Aldrich, UK ) with and without quercetin. The final concentration of components in the two samples were 50  $\mu$ M A $\beta$ <sub>1-40</sub>, 15  $\mu$ M ThT and 0 or 50  $\mu$ M Quercetin. Samples were incubated at 37°C and all components and solutions were in thermal equilibrium before use.

### **5.4. Tyr, NAYA and A $\beta$ <sub>1-16</sub> with copper ions (Cu<sup>2+</sup>)**

The buffered (HEPES, pH 7.4) solutions of Tyr, NAYA, and A $\beta$ <sub>1-16</sub> peptides were prepared prior to measurements and incubated at temperature 37°C. Different concentrations of CuSO<sub>4</sub>·5H<sub>2</sub>O were added to the solutions. The molar concentrations of Cu<sup>2+</sup> ranged from 0 to 50 mM for Tyr, and 0 to 100  $\mu$ M for NAYA and A $\beta$ <sub>1-16</sub>.

### **5.5. A $\beta$ <sub>1-11</sub> and A $\beta$ <sub>1-16</sub> with quercetin:**

samples were prepared by dissolving A $\beta$ <sub>1-11</sub> and A $\beta$ <sub>1-16</sub> peptides (Sigma-Aldrich, UK) in a buffer (HEPES, pH 7.4) solution to a concentration of 50  $\mu$ M. Different concentrations of quercetin dihydrate were added to the solutions. The molar concentrations of quercetin ranged from 0 to 200  $\mu$ M.

### **5.6. Polystyrene standard beads:**

Polystyrene nanometre standard beads with sizes of 50, 100, and 460 nm were purchased from Sigma-Aldrich, UK. They were diluted from the supplied package in distilled water. Dilutions were chosen based on maintaining 20–100 particles per viewing area, as recommended by the Nanosight manufacturer.

## 6. Detecting beta-amyloid aggregation from time-resolved emission spectra

### 6.1. Introduction

The majority of the techniques used to investigate beta-amyloid performance on a molecular level use A $\beta$  labelled dyes. Our approach to this task is to use the sub-ns time and sub-nm spatial resolution of time-resolved fluorescence spectroscopy of intrinsic fluorophores. This allows a non-invasive detection of very small changes in the surroundings of the fluorophore without disturbing its native structure. For example, it has been demonstrated<sup>46</sup> that when exciting A $\beta$  with a 279 nm pulsed LED source, A $\beta$ 's single tyrosine (Tyr) fluorescence decay responds to the changes in its environment induced by peptide oligomerization from the early stages. Unfortunately, the intrinsic fluorescence decay of amino acids such as Tyr in solution is complicated and has remained unresolved over several decades.

Typically, such decays are analysed by fitting to multi-exponential functions which are explained by one of two contradictory views of the excited state processes: the rotamer model (assuming discrete ground-state conformations<sup>124,125</sup>) and the dielectric relaxation model (spectral shift due to dipolar relaxation<sup>115,127</sup>). Previous beta-amyloid studies<sup>37,46,140</sup>, based on Tyr fluorescence and molecular dynamics simulations, suggested that the Tyr fluorescence decay can be adequately explained by a four-rotamer model. Moreover, the plot of the ratio of pre-exponential factors versus time can serve as a calibration curve for determining the extent of A $\beta$  oligomerisation. More recently, a study has shown an alternative model with less variables, which also fits well to the A $\beta$  decay during oligomerisation, and assumes a continuous stable distribution of the

fluorescence transition rates resulting in the non-Debye fluorescence intensity decay function<sup>141</sup>

$$I_{\alpha,\kappa}(t) = \exp \left[ -\frac{1}{\kappa} \int_0^{\kappa(\frac{t}{\tau_0})^\alpha} \left( 1 - \exp \left[ -\frac{1}{x} \right] \right) dx \right] \quad 48$$

where  $\tau_0$  (of the dimension of time) and the non-dimensional parameters  $\alpha$  and  $\kappa$  determine the stable distributions of the fluorescence transition rates. Tracking the evolution of  $\tau_0$ ,  $\alpha$  and  $\kappa$  during A $\beta$  aggregation has shown<sup>45</sup> that  $\alpha$  takes values larger than one during the first 40 h of aggregation, which is not possible if the relaxation of the excited-states is the only process occurring, no matter what the distribution of the transition rates is.

In this chapter, we study changes in TRES collected for Tyr in A $\beta$  and the possibility of using these changes as an indicator of peptide aggregation. In our approach, we assume that both the dielectric relaxation and depopulation of the excited states in the current composition of oligomers occur at the same time scale and thus both affect the fluorescence decay. Previous research<sup>129,142</sup> suggests that these processes can be distinguished from each other by a quantitative model of simultaneous decay and electrostatic relaxation. Note that the model of homogeneous dielectric relaxation assumes the existence of a single form of a fluorophore, where the transient spectra decreases its intensity and shifts towards lower energies, but maintains its shape. Here we investigate whether the aggregating amyloids can be described by a similar model, or whether the consideration of more than one fluorescent residue is needed. For this purpose, we monitor the time-resolved emission spectra (TRES) changes in an A $\beta$  sample during its aggregation over eight days.

## 6.2. Results and discussion

Experimental observations of A $\beta$ 's fluorescence intensity decays,  $I_\lambda(t)$ , (Figure 20b) show that the mean decay lifetime ( $\bar{\tau} = \frac{\int_0^\infty t I_\lambda(t) dt}{\int_0^\infty I_\lambda(t) dt}$ ) increases with an increase in the detection wavelength, which is consistent with the lifetime wavelength correlation usually observed in protein fluorescence. We can also see that the decays evolve when the sample ages. For example, the fluorescence decays at a detection wavelength of 297 nm show that the mean lifetime at day 8 ( $\bar{\tau} = 0.91 \pm 0.02$  ns) is shorter than at day 1 ( $\bar{\tau} = 1.20 \pm 0.01$  ns), whereas decays at a detection wavelength of 327 nm have a similar mean lifetime ( $\bar{\tau} \approx 1.37 \pm 0.06$  ns). Fitting the decays to the three-exponential model (Figure 20a) shows that at an early stage of aggregation (day 1), all three lifetimes increase with the detection wavelength. At a late stage the increase is smaller and the lifetime-wavelength correlation can hardly be observed. The contributions of scattered light (parameter S in figure 20a) show that decay curves measured at short detection wavelengths are highly affected by scattered excitation light, especially at the late stages of aggregation. For example, the contribution of scattered light at a detection wavelength of 297 nm is 10.6% at day 1 and increases to 21.5% at day 8.

The TRES  $I_t(\nu)$  were calculated for several fixed times. Figure (20 c) shows the examples of six spectra at different times after excitation measured on day 1 and then on day 8. For the purpose of detailed analysis of the A $\beta_{1-40}$  TRES we modelled the recovered spectra  $I_t(\nu)$  using the Toptygin-type approach<sup>129</sup>, which assumes that the fluorescence spectrum  $I_t(\nu)$  of a single fluorescent residue can be expressed as  $\sim \nu^3 g(\nu)$ , where  $g(\nu)$  is the Gaussian distribution function. Consequently, the spectrum of a sample with  $N$  fluorescent residues would be described by the sum of  $N$  normalized functions of the type  $\sim \nu^3 g(\nu)$

$$I_t(v) = \sum_{i=1}^N \frac{C_i(t)v^3 \exp\left[-(v - v_i(t))^2 / (2\sigma_i^2(t))\right]}{\sqrt{2\pi} v_i(t) \sigma_i(t) (v_i^2(t) + 3\sigma_i^2(t))} \quad 49$$

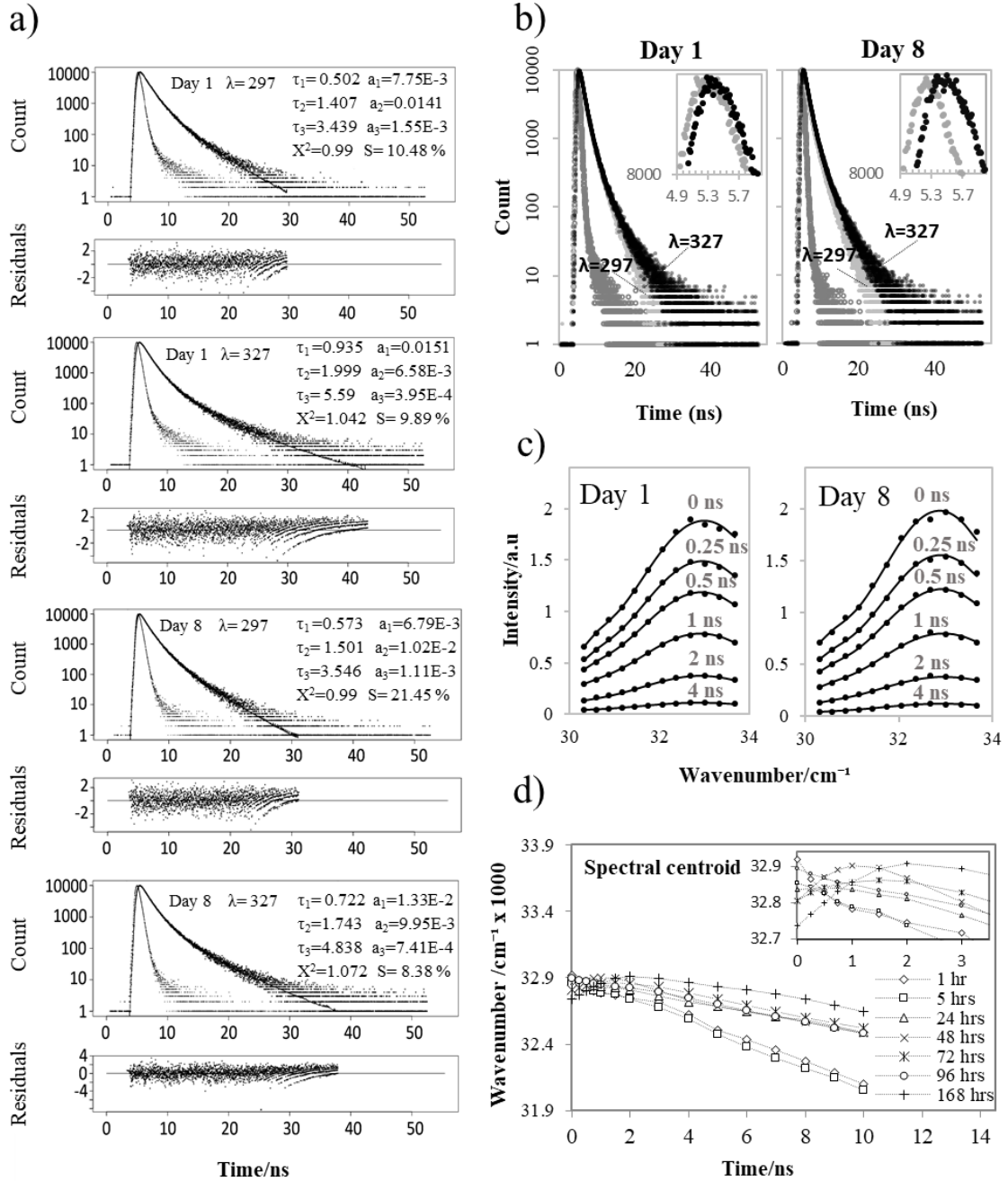


**Figure 20.** (a) Fluorescence decay data of beta-amyloid at the detection wave lengths 297 and 327 nm together with the excitation pulse, fitted three-exponential function, the scattered light term (S) and the distribution of residuals. (b) The time-wavelength correlation observed in two decays of beta-amyloid at detection wave lengths 297 and 327 nm and at two different stages of aggregation: day 1 and day 8. The insets show the peak areas of the experimental curve. (c) Time resolved emission spectra (TRES) obtained at two different stages of aggregation (day 1 and day 8) fitted to a two Gaussian profile. (d) The change in the centroid of the emission spectrum (see equation (50)) on the nanosecond scale at different stages of aggregation. <sup>143</sup>

where  $t$  is the time after excitation in ns,  $\nu$  is wavenumber in  $\text{cm}^{-1}$ ,  $\sigma_i(t)$  is the standard deviation of each component,  $\nu_i(t)$  is its peak position and  $C_i(t)$  - the fluorescence intensity contribution of the  $i$ -th component at the time  $t$ , i.e. the fluorescence intensity decay of this component. According to the Toptygin paper<sup>129</sup>  $g(\nu)$  should be a skewed function. However, we use Gaussian to reduce the number of parameters of our model of TRES. It should also be noted that equation 49 is a technical model of the TRES (i.e. may represent more than just a dielectric relaxation) and the analysis of the goodness of fit and the recovered parameters has to be done first to suggest any specific mechanism or cause of the observed TRES.

The observed good fit of the function from equation (49) when  $N=2$  to the experimental TRES data may be an indication of the existence of two fluorescent forms, but we cannot exclude the fact that there is a single form with a double-peak spectrum. If the latter is the case, the spectrum should shift as a whole monotonically towards shorter wavenumbers. To investigate this option, we have inspected the changes in the position of the spectral centroid  $\nu_c(t)$  given by the equation

$$\nu_c(t) = \frac{\nu_1(t)C_1(t) + \nu_2(t)C_2(t)}{C_1(t) + C_2(t)} \quad 50$$

A plot of  $\nu_c(t)$  against time  $t$  is shown in figure (20 d). The change in the spectral centroid  $\nu_c(t)$  is non-exponential. In fact, an initial increase is observed before a gradual decrease occurs. This non-monotonic behaviour of  $\nu_c(t)$  suggests a more complex composition of the sample and has brought us to the hypothesis that the sample contains two or more different forms, all involved in the solute solvent-relaxation with the peaks undergoing exponential decays at their own rates. The parameters obtained from fitting the two-Gaussian profile to the TRES are plotted in figures (21 a, b and c).

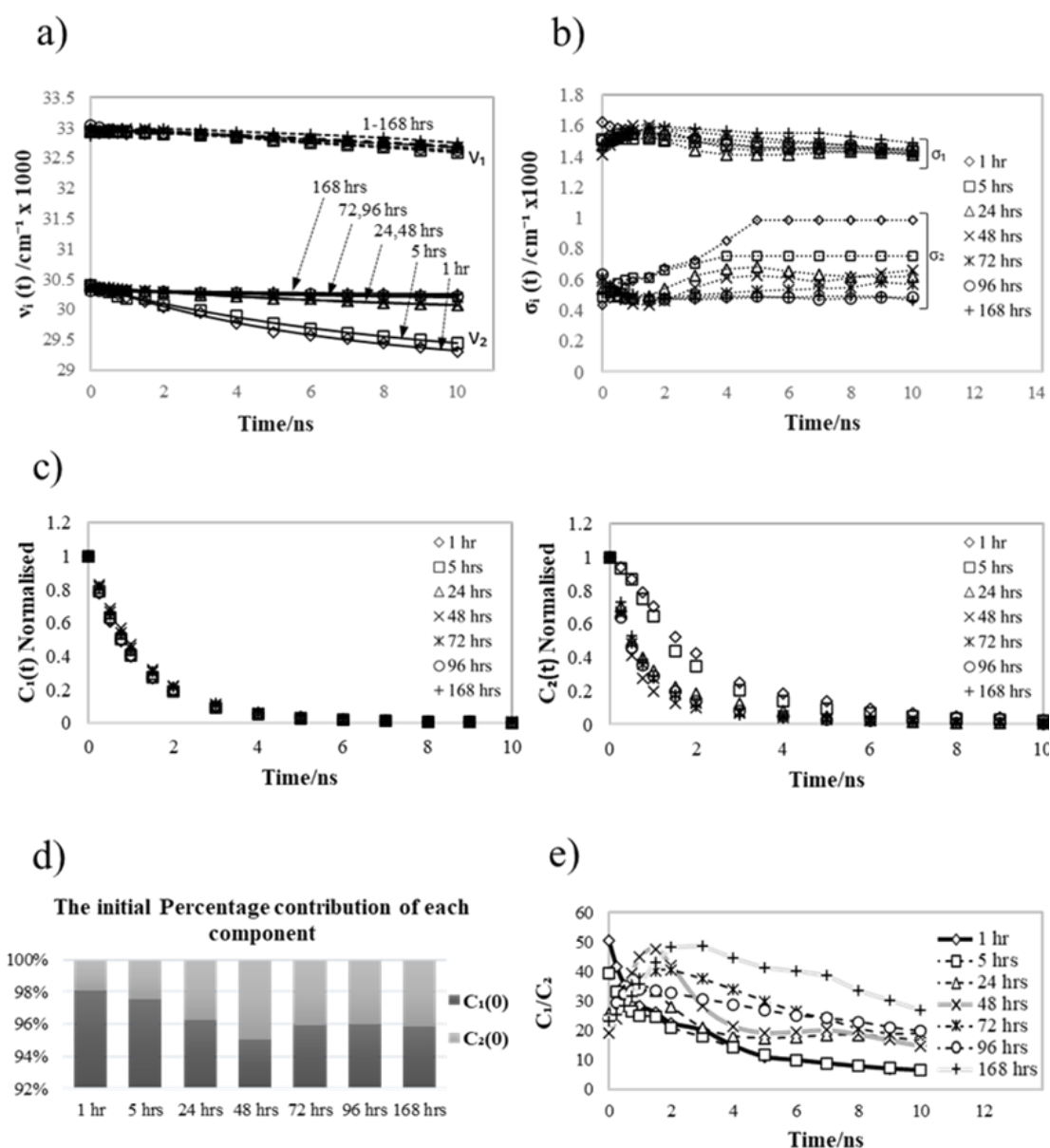


**Figure 21 .** (a) Evolution of the peak positions  $v_1(t)$  and  $v_2(t)$  with time. (b) Standard deviation of both peaks  $\sigma_1(t)$  and  $\sigma_2(t)$  at different stages of aggregation. (c) fluorescence intensity decay of each component (monomers  $C_1$ , oligomers  $C_2$ ). (d) The initial Percentage contribution of each component  $C_1(0)$  and  $C_2(0)$  at different stages of aggregation. (e) The Ratio of the monomer to oligomer contribution  $C_1(t)/C_2(t)$  plotted against time. <sup>143</sup>

The parameters describing the position of each peak  $v_l(t)$ , starting at  $33\,000\text{ cm}^{-1}$  and  $v_2(t)$  starting at  $30\,500\text{ cm}^{-1}$ , evolve in time, as shown in figure (21 a). The position of the first peak  $v_1(t)$  does not show significant changes in time, indicating slow dielectric relaxation. Currently we associate this peak with  $A\beta$  monomers. Monomers are expected

to have a short dielectric relaxation time due to their small size and concomitant tyrosine's exposure to water, thus the dielectric relaxation process is almost completed before the fluorescence occurs, and therefore has a very weak effect on the shift of the fluorescence peak.

The position of the second peak  $\nu_2(t)$  shifts exponentially from an initial value  $\nu_2(0)$  to a substantially lower energy value  $\nu_2(\infty)$  with the relaxation time  $\tau_r \approx 8 \text{ ns}$ . The dielectric relaxation times  $\tau_r$  of the second form (see table 2) increase as the sample ages, suggesting the gradual growth of the formed oligomers. This relaxation time can therefore be used as an indicator of the progress of A $\beta$  aggregation. Oligomerisation explains the initial shift of the emission peak from  $33\,000 \text{ cm}^{-1}$  to about  $30\,500 \text{ cm}^{-1}$  and its further red shift due to dielectric relaxation.

**Table 2.** The TRES second peak's positions  $\nu_2(0)$  and  $\nu_2(\infty)$ , and the dielectric relaxation times  $\tau_r$ . The parameters estimates and their standard errors were obtained by fitting data points to single exponential decay functions using the data analysis software Origin Pro 8.6.

	1 hr	5 hr	24 hr	48 hr	72 hr	96 hr	168 hr
$\nu_2(0) \text{ cm}^{-1}$	$30\,410 \pm 70$	$30\,370 \pm 98$	$30\,370 \pm 31$	$30\,380 \pm 12$	$30\,330 \pm 10$	$30\,314 \pm 9$	$30\,320 \pm 11$
$\nu_2(\infty) \text{ cm}^{-1}$	$29\,000 \pm 77$	$29\,000 \pm 105$	$29\,940 \pm 33$	$29\,920 \pm 13$	$30\,150 \pm 11$	$30\,169 \pm 9$	$30\,210 \pm 11$
$\tau_r(t) \text{ ns}$	$6.6 \pm 0.7$	$8 \pm 1$	$9 \pm 1$	$8.9 \pm 0.4$	$9.0 \pm 0.8$	$10.6 \pm 0.9$	$11 \pm 1.6$

Because the Gaussian functions used in equation (49) are normalised, parameters C1 and C2 can be considered as the fluorescence contributions of each component. Thus, the plots of C1 and C2 versus time (Figure 21 c) represent the decay of the fluorescence intensity of each component individually. The results show that the mean lifetime of the second peak is highly affected by A $\beta$  aggregation, suggesting that at the early stages of

aggregation, the impact of dielectric relaxation on the fluorescence decay curve is strong. The first peak does not show any significant changes in the mean lifetime, which is consistent with the first peak representing monomers.

The ratio  $C1(0)/C2(0)$  shows that the contribution of the monomer peak is dominant but slightly decreases as the sample ages (Figure 21d). The  $C1(t)/C2(t)$  ratio changes after excitation, as shown in figure (21 e), which is a result of two components decaying at different rates. In the course of aggregation, the ratio  $C1(t)/C2(t)$  evolves differently on the nanosecond scale due to the change in the amount and mean decay time of the oligomers, and therefore can be used as an indication of the stage of aggregation.

### **6.3. Conclusion**

Changes in the TRES of the aggregating beta-amyloids indicate at least two different sub-systems of fluorescent tyrosine—one originating from Tyr in monomers and the other from Tyr in oligomers.

The latter decay is likely to be determined by several processes. In addition to the dielectric relaxation, we cannot exclude the heterogeneity of the formed oligomers, each showing slightly different fluorescence characteristics, thus leading to the distribution of fluorescence lifetimes.

The observed kinetics is complex and the multiexponential functions need to be fitted to the experimental decays to satisfy the goodness of fit criteria. The multi-exponential approach is sufficient for determining TRES from the raw fluorescence decays. However, because we demonstrated that the dielectric relaxation, probably together with the heterogeneity of the fluorescence residues substantially impact the observed decays, both processes cannot be neglected in the proper model of the kinetics. Therefore, in the studies of protein aggregation, the kinetic models combining both the dielectric

relaxation and the variety of the specific mechanisms of depopulation of the excited states (e.g. one governed by the so called stable distribution of the decay rates<sup>142</sup>) should be considered to properly represent the fluorescence characteristics of the heterogenic molecular system.

## 7. Copper ion ( $\text{Cu}^{2+}$ ) effects on beta-amyloid oligomerisation monitored by fluorescence of intrinsic tyrosine

### 7.1. Introduction

Metal ions such as  $\text{Cu}^{2+}$  and  $\text{Zn}^{2+}$  are found in abnormally high concentrations within senile plaques of Alzheimer's. In vitro studies<sup>144,145</sup> show that such ions can bind to  $\text{A}\beta$  directly and modulate the aggregation process. Given the redox activity of Cu it is strongly believed that its complex with  $\text{A}\beta$  ( $\text{Cu-A}\beta$ ) might be involved in the formation of reactive oxygen species<sup>145</sup> that contribute to the oxidative stress observed in Alzheimer's disease. Thus, it appears that the interaction of Cu with  $\text{A}\beta$  is linked to Alzheimer's disease.

$\text{Cu-A}\beta$  complexes have been investigated widely for the past decade by means of various techniques including IR spectroscopy<sup>146[6]</sup>, x-ray absorption spectroscopy XAS<sup>146,147</sup>, circular dichroism CD<sup>147,148[</sup>, Nuclear Magnetic Resonance NMR<sup>147[7]</sup>, Raman spectroscopy<sup>149 9]</sup> and Electron Paramagnetic Resonance EPR<sup>147,148[7,8]</sup>. Currently, the most accepted coordination model of  $\text{Cu}^{2+}$  ions to the  $\text{A}\beta$  peptide at pH7.4 suggests that the  $\text{Cu-A}\beta$  complex can exist in two main forms<sup>150-152</sup> as shown in Figure 22. The two components are usually noted I and II. In component I,  $\text{Cu}^{2+}$  preferably binds to the  $\text{NH}_2$ -terminal amine, the adjacent CO from the Asp1-Ala2 peptide bond, the N atom from the imidazole ring of His6 and imidazole ring of His13 or His14, or two N atoms from His13 and His14. The apical position of the square-pyramidal copper complex is likely to be occupied by an oxygen atom from either a carboxylate group or a water molecule. Component II can be generated by the deprotonation of the Asp1-Ala2 amide bond, which leads to  $\text{Cu}^{2+}$  binding equatorially to the deprotonated amide function from the

Asp1-Ala2 peptide bond, the N-terminal amine, the adjacent CO from Ala2-Glu3 peptide bond and one N atom from the imidazole ring of either His6, His13 or His14.

The extensively discussed aspect of the role of copper in Alzheimer's is its impact on the aggregation of A $\beta$  in the presence of A $\beta$ -Cu<sup>2+</sup> complexes<sup>150</sup>.

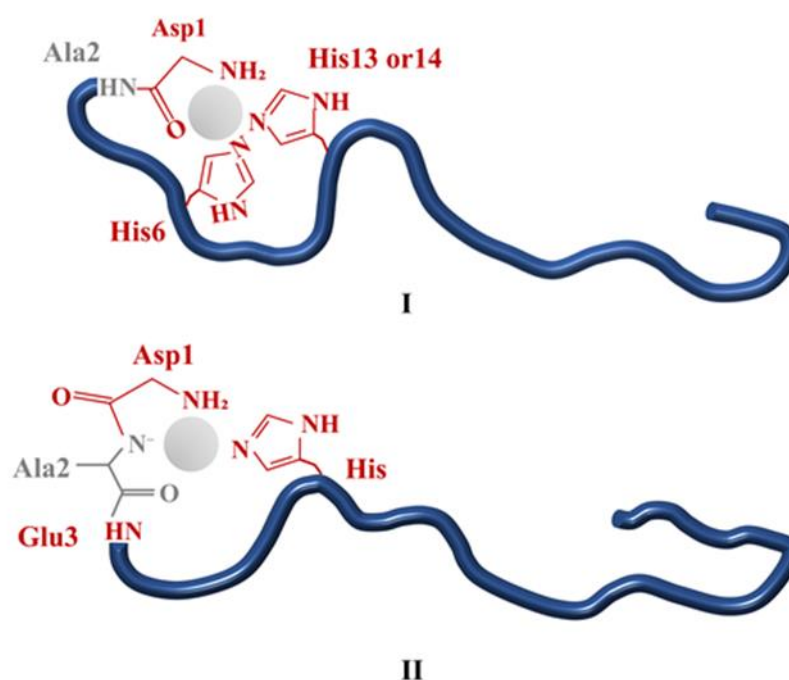


**Figure 22.** Scheme showing the coordination sites of Cu<sup>2+</sup>-A $\beta$  for component I and II at pH 7.4. <sup>153</sup>

The formed aggregates are either amorphous or fibrillar and both depend on experimental parameters such as the concentration of Cu<sup>2+</sup> and the pH level. It has been suggested that Cu<sup>2+</sup> ions accelerate the formation of fibrils at the 1:1 ratio, possibly due to metal-mediated dimerization and a stabilization of oligomers<sup>150</sup>. Conversely, excess amounts of Cu<sup>2+</sup> produces more amorphous aggregates and less fibrils.

Here we use for the first time our non-invasive technique to research A $\beta$ <sub>1-40</sub> interactions with copper ions and consequent aggregation of the copper – bound amyloids, making the next step towards better understanding of neurotoxicity of amyloid oligomers. Our approach explores the relationship between the changes in intrinsic fluorescence of Tyr<sub>10</sub>

in A $\beta$ <sub>1-40</sub>, and the progress of A $\beta$ <sub>1-40</sub> aggregation<sup>37,46,126,140</sup>. Thanks to the non-invasiveness of the Tyr<sub>10</sub>-based approach we achieve a perhaps unique opportunity to detect the earliest stages of A $\beta$ <sub>1-40</sub>-Cu<sup>2+</sup> interactions, well before the other techniques (like that based on ThT fluorescence) detect any changes.

To allow the interpretation of the Tyr in A $\beta$ <sub>1-40</sub> decay data in the context of copper impact on aggregation, we extended the lifetime measurements to the number of samples with Tyr-containing amyloid fragments and copper, and gradually increased the level of their complexity (sequentially: Tyr, N-Acetyltirosinamide (NAYA), A $\beta$ <sub>1-16</sub>, A $\beta$ <sub>1-40</sub>).

## 7.2. Results and discussion

Copper in the solutions of A $\beta$  fragments can potentially cause two types of effects on fluorescence kinetics: direct, i.e. quenching of Tyr fluorescence and indirect, by having the influence on aggregation process. The potential direct effects were investigated first. Adding mM concentrations of Cu<sup>2+</sup> reduces the value of Tyr's fluorescence lifetime  $\tau$  as shown in Figure (23a). The ratio  $\tau_o/\tau$ , where  $\tau_o$  is the lifetime of Tyr without Cu<sup>2+</sup>, follows the Stern-Volmer relationship, i.e. is proportional to the concentration of Cu<sup>2+</sup> (Figure 23b), indicating collisional quenching. However, at the concentrations of Cu<sup>2+</sup> ions in the  $\mu$ M range i.e. similar to the concentration of A $\beta$  (50  $\mu$ M) used in our experiments,  $\tau$  remains constant (Figure 23c), which excludes collisional quenching of Trp by Cu<sup>2+</sup> in  $\mu$ M range. The next step was to investigate the influence of Cu<sup>2+</sup> on NAYA, which is considerably an appropriate model compound of a nonterminal tyrosine within a protein. Fluorescence decay of Tyr in NAYA is intrinsically more complex and well described by a two-exponential model. Adding Cu<sup>2+</sup> to NAYA did not affect the

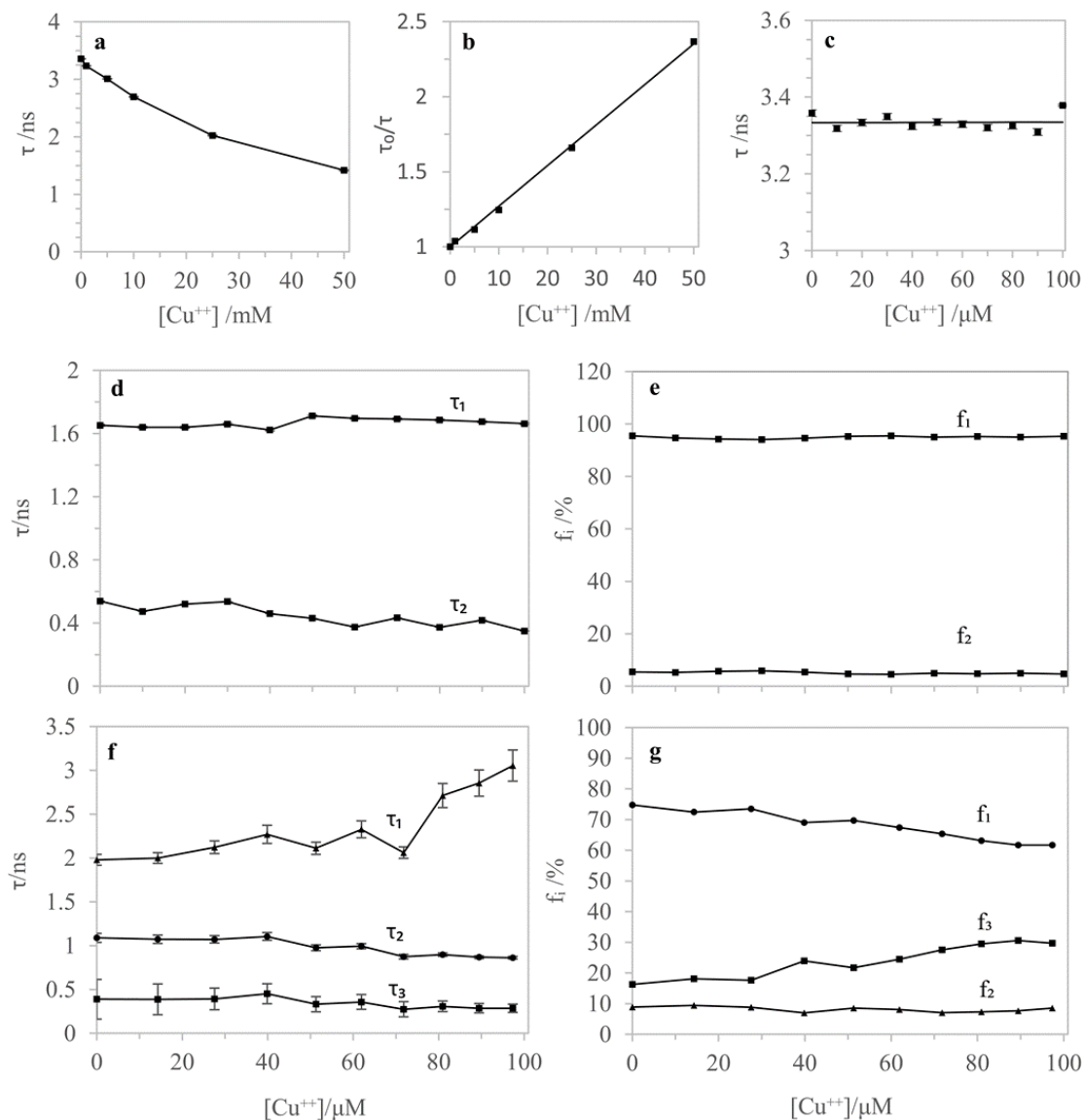


**Figure 23.** Plots showing the correlation between Tyr's Fluorescence lifetime  $\tau$  and the concentration of  $\text{Cu}^{2+}$  in mM (a) and  $\mu\text{M}$  (c) scales; The Stern–Volmer plot of fluorescence quenching of Tyr by  $\text{Cu}^{2+}$  ions (b); Plot showing the effect of  $\text{Cu}^{2+}$  on parameters obtained from fitting NAYA's fluorescence decay to a two-exponential model: decay times  $\tau_1$  and  $\tau_2$  (d), and the percentage contributions  $f_1$  and  $f_2$  (e); Parameters obtained from fitting Tyr's fluorescence decay in a  $50 \mu\text{M}$   $\text{A}\beta_{1-16}$  solution to a three-exponential decay model plotted against  $\text{Cu}^{2+}$  concentration: Tyr fluorescence decay times  $\tau_1$ ,  $\tau_2$  and  $\tau_3$  (f), percentage contributions  $f_1, f_2$  and  $f_3$  (g). Error bars represent the standard deviation.<sup>153</sup> (Measurements were taken by Thorben Wellbrock)

lifetime components and their contributions as we increased the concentration of  $\text{Cu}^{2+}$  up to  $100 \mu\text{M}$  (Figure 23 d and e). Therefore, it is reasonable to accept that the fluorescence kinetics of NAYA is also not affected by  $\text{Cu}^{2+}$ . The  $\text{A}\beta_{1-16}$  fragment was

then investigated upon adding  $\mu\text{M}$  concentrations of  $\text{Cu}^{2+}$ . Due to increasing complexity of the local environment of Tyr in this peptide, obtaining a good fit for fluorescence decay for the no- $\text{Cu}^{2+}$  sample required using a 3-exponential model. The fitted decay times and their associated contributions change with  $\text{Cu}^{2+}$  concentration as shown in Figure (23f) and g. The effect observed is likely to be a result of the  $\text{Cu}^{2+}$ -A $\beta$  complex formation, as His6 and His13 (or His14) are expected to form copper ion binding site in A $\beta_{1-16}$  peptide. This explains why Tyr's fluorescence signal in A $\beta_{1-16}$  is considerably sensitive to the change in  $\text{Cu}^{2+}$  concentration. Overall, the effect of adding  $\mu\text{M}$  concentrations of  $\text{Cu}^{2+}$  is weak either because the binding of  $\text{Cu}^{2+}$  with A $\beta_{1-16}$  is insignificant or because the effect of binding to  $\text{Cu}^{2+}$  is weak.

The copper ions effects on the full Alzheimer's peptide, A $\beta_{1-40}$ , were studied by monitoring fluorescence responses of three samples: one without copper and the other two containing 15  $\mu\text{M}$  and 35  $\mu\text{M}$  of  $\text{Cu}^{2+}$ . Because A $\beta_{1-40}$  tends to aggregate, measurements were taken several times over the period of 80 hours to track the evolution in the Tyr signal. Fluorescence intensity decays of A $\beta_{1-40}$  were analysed using the DAS6 software from HORIBA Jobin Yvon (IBH) Ltd, thus an additional component is required to represent the scattered excitation light. Decays of A $\beta_{1-40}$  were best fitted to the 4-exponential model functions ( $\chi^2= 0.9 - 1.1$ , and residuals were randomly distributed). Figures (24a and b) show the changes in the lifetime components and percentage contributions as the A $\beta_{1-40}$  sample aggregation progresses in the absence of  $\text{Cu}^{2+}$  ions. Three of the lifetime components ( $\tau_1 \approx 0.1$  ns,  $\tau_2 \approx 1$  ns and  $\tau_3 \approx 3.4$  ns) remain constant during the aggregation process whereas the fourth  $\tau_4$  exhibits a significant decrease from 18 ns to 8 ns within 80 hours.

The contributions of the two short lifetime components  $f_1$  and  $f_2$  show an increase in the first 15 hours and then remain constant as the aggregation progresses (Figure 24b).

Simultaneously, the contributions of the two components with larger lifetimes,  $f_3$  and  $f_4$ , exhibit an initial decrease and then remain the same as the sample ages. Changes observed in the fluorescence decay parameters suggest conformational changes in  $A\beta_{1-40}$  during its aggregation and can be used to indicate the stage of peptide aggregation, as we obtained previously<sup>46</sup>.

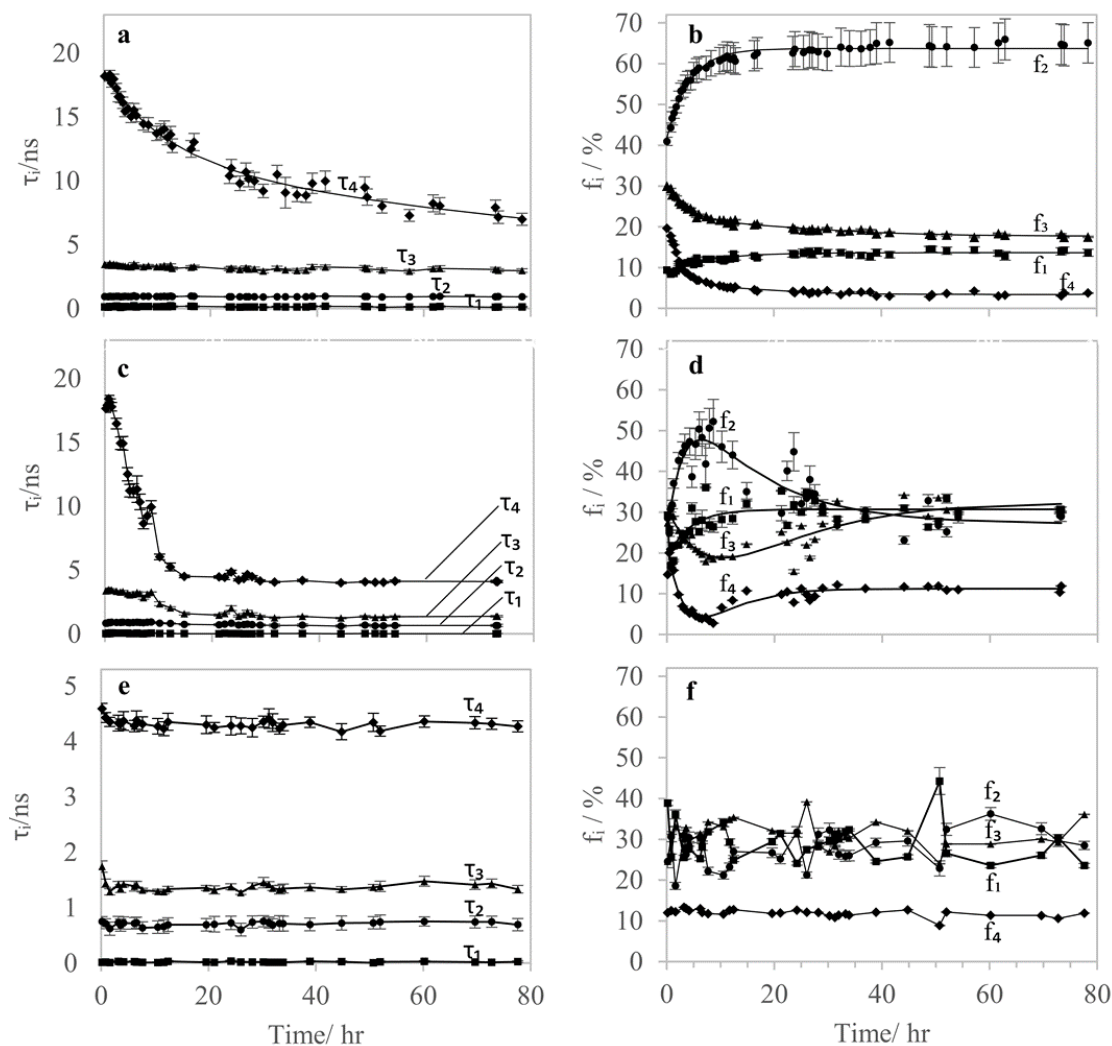


**Figure 24.** Parameters obtained from fitting Tyr fluorescence decay in a 50  $\mu$ M  $A\beta_{1-40}$  solution to a four-exponential decay model as aggregation proceeds: Tyr fluorescence decay times  $\tau_1$ ,  $\tau_2$ ,  $\tau_3$  and  $\tau_4$  in free  $A\beta_{1-40}$  (a), in the presence of 15  $\mu$ M (c) and 35  $\mu$ M (e) of  $Cu^{2+}$ , percentage contributions of the decay components  $f_1$ ,  $f_2$ ,  $f_3$  and  $f_4$  in free  $A\beta_{1-40}$  (b), in the presence of 15  $\mu$ M (d) and 35  $\mu$ M (f) of  $Cu^{2+}$ . Error bars represent the standard deviation.<sup>153</sup> (Measurements were taken by Thorben Wellbrock)

Figure (24c) shows the developments in lifetime components of  $A\beta_{1-40}$  in the presence of 15  $\mu$ M of  $Cu^{2+}$ . Note, that the initial values of  $\tau_1$ - $\tau_4$  are identical to those obtained in

the absence of  $\text{Cu}^{2+}$ . This demonstrates that, like in  $\text{A}\beta$  fragments, the presence of copper ions does not affect directly (i.e. by quenching) the fluorescence kinetics of Tyr in  $\text{A}\beta_{1-40}$ . However, the later changes in the fluorescence decays demonstrate different behavior of aggregation. The decay times  $\tau_1$  and  $\tau_3$  remain constant only for the first 10 hours and then they decay to  $\tau_1 \approx 0.01$  ns,  $\tau_2 \approx 0.6$  ns and  $\tau_3 \approx 1.4$  ns within the next 5 hours and remain constant afterwards. The lifetime of the fourth component decays at a faster rate than that observed in free  $\text{A}\beta_{1-40}$  from 18 ns to 4 ns within 10 hours. Simultaneously, the contributions of the decay components  $f_1$  and  $f_4$  show similar behavior to that observed in free  $\text{A}\beta_{1-40}$  for the first 10 hours only and then this trend breaks down (Figure 24d). The lifetimes and contribution parameters taken together indicate faster complexation and formation of the final product that is completely different than the structure created in the absence of  $\text{Cu}^{2+}$ .

In the presence of 35  $\mu\text{M}$  concentration of  $\text{Cu}^{2+}$  (Figure 24e and f), the decay times along with the associated relative contributions are fairly constant during the time of experiment and their values are almost identical to those obtained for the 15  $\mu\text{M}$   $\text{Cu}^{2+}$  sample after around 15 hours. This suggests that the aggregation occurring in the 35  $\mu\text{M}$   $\text{Cu}^{2+}$  sample is similar to the process in the 15  $\mu\text{M}$   $\text{Cu}^{2+}$  sample but is significantly accelerated.

To summarize this section, the analysis of Tyr fluorescence decays shows that copper ions not only accelerate the aggregation of  $\text{A}\beta_{1-40}$  peptides but also alter the final products (oligomers). Indeed, decreasing values of all lifetime parameters  $\tau_i$  and changes in the  $f_i$  contributions observed after the 10th hour of aggregation in the 15  $\mu\text{M}$   $\text{Cu}^{2+}$  sample, may be the result of radical alterations in the immediate environment of the Tyr residues.

We also note, that because adding copper ions affects all  $\tau_i$  and  $f_i$  parameters in a similar manner, a 4-exponential function used in data analysis is unlikely to reflect a 4-rotamer kinetics of Tyr in A $\beta_{1-40}$  but is only a good analytical representation of the decays. Moreover, it is not clear if fluorescence intensity decays collected at one arbitrarily selected detection wavelength efficiently reflect the kinetics of this undoubtedly complicated molecular system.

Therefore, to reveal more information on the underlying kinetics, TRES measurements were performed for A $\beta_{1-40}$  at several stages of aggregation, namely 1, 5, 24, 48, 72, 96 and 168 hrs after sample preparation (the number indicates the age of the sample when the measurement at the first wavelength has been started).

Figure 25 shows the examples of TRES of the 1 hour and 168 hours old samples without (Figure 25a) and with 15  $\mu$ M (Figure 25b) of copper ions. According to Topygin and Brand<sup>129</sup> the fluorescence spectrum of a single fluorescent residue can be expressed as  $\sim v^3 g(v)$ , where  $g(v)$  is the Gaussian distribution function.

Therefore, for the purpose of detailed analysis of the A $\beta_{1-40}$  TRES we modelled the recovered spectra  $I_i(v)$  at the time  $t$  as the sum of  $N$  normalized functions of the type  $\sim v^3 g(v)$  as in equation 49.

In our previous work<sup>143</sup> on aggregation of free A $\beta_{1-40}$  we have identified two peaks in the spectra and explained them by the presence of non-aggregating monomers and aggregating oligomers, both involved in dielectric relaxation at different rates. The analysis of the experimental TRES for the sample with Cu<sup>2+</sup> also demonstrated the presence of two components ( $N=2$ ).

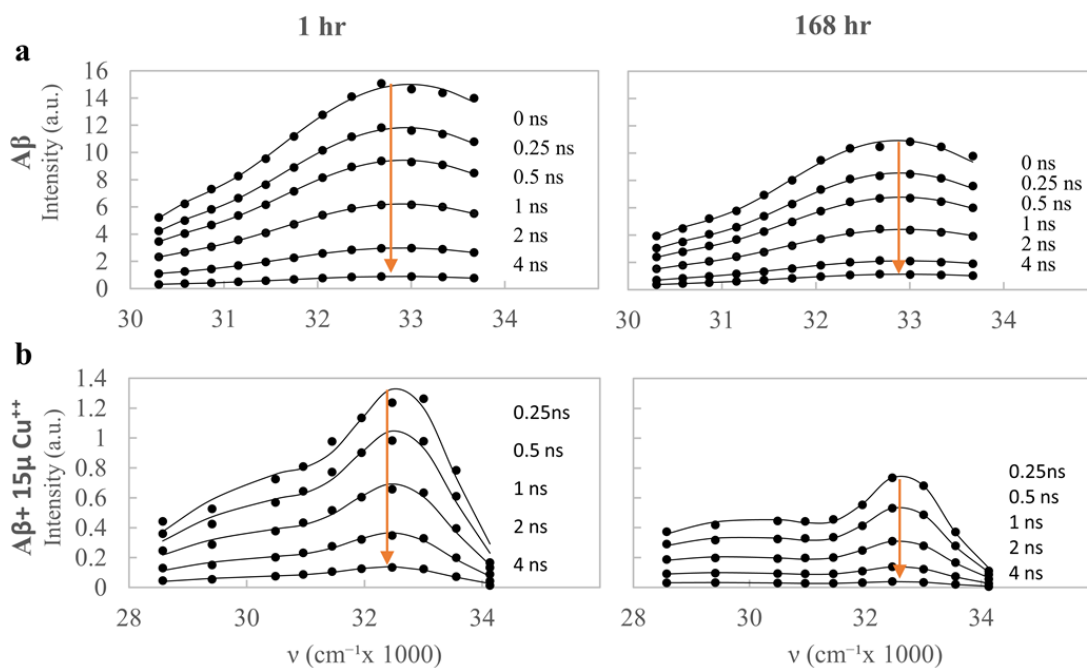


**Figure 25.** Time-resolved emission spectra (TRES) obtained for 50 μM Aβ<sub>1-40</sub> (a) and 50 μM Aβ<sub>1-40</sub> with 15 μM Cu<sup>2+</sup> (b) at two stages of aggregation (1 hr and 168 hr). The solid lines represent the two-Toptygin type functions fits.<sup>153</sup>

Here we compare the fluorescence kinetics of the both samples, one without Cu<sup>2+</sup> and one with 15 μM of Cu<sup>2+</sup> ions by means of the parameters recovered from fitting the model TRES (Equation 49 for N=2) to the experimental data (Figure 26). In the absence of Cu<sup>2+</sup> (Figure 26a) the position of the first peak  $\nu_1(t)$  is located at about 33000 cm<sup>-1</sup> and does not show significant changes over time, which indicates fast dielectric relaxation that is practically completed before fluorescence occurs. Therefore, we attribute this component to the monomers. The second peak starts from an initial value  $\nu_2(0) \approx 30500$  cm<sup>-1</sup> and, for the 1 hr old sample, shows an exponential shift to a lower energy value  $\nu_2(\infty) \approx 29000$  cm<sup>-1</sup> with the dielectric relaxation time  $\tau_R = 6.7$  ns. The relaxation time increases as the sample ages indicating gradual growth in the aggregates size. We associate the second peak with oligomers because it justifies why it initially

appears at a lower energy value ( $30500\text{ cm}^{-1}$ ) due to aggregation and its further red shift due to dielectric relaxation.

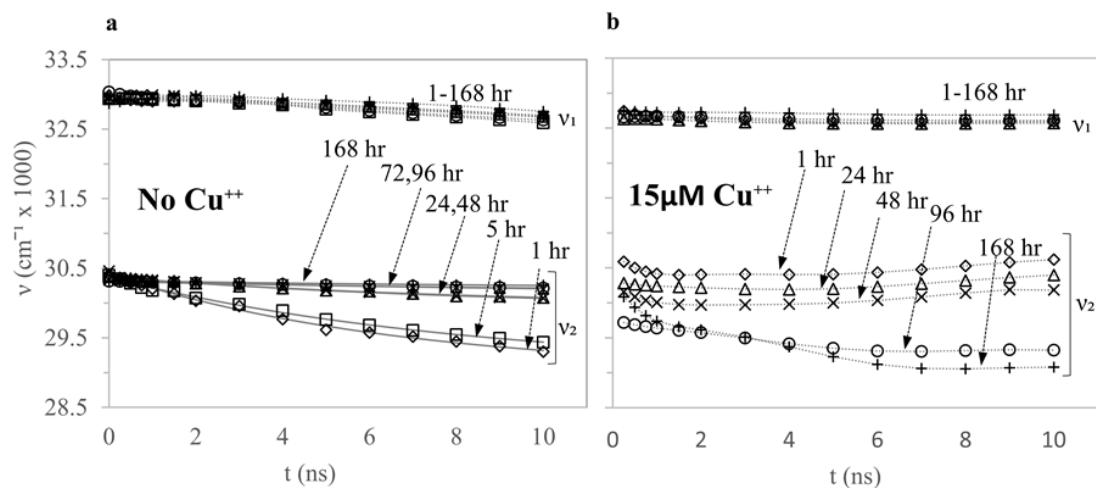


**Figure 26.** Evolution of the peak positions  $v_1(t)$  and  $v_2(t)$  for free  $A\beta_{1-40}$  (a) and  $A\beta_{1-40}$  with  $15\ \mu\text{M}\ \text{Cu}^{2+}$  (b) at different stages of aggregation ( $\diamond$  1hr,  $\square$  5hr,  $\Delta$  24hr,  $\times$  48hr,  $*$  72hr,  $\circ$  96 hr and  $+$  168 hr).<sup>153</sup>

Addition of  $15\ \mu\text{M}\ \text{Cu}^{2+}$  to the sample (Figure 26b) shifts the position of the first peak  $v_1(t)$  from  $33000\text{ cm}^{-1}$  to  $32800\text{ cm}^{-1}$ . No further shift is observed in the position of this peak after excitation and remains unchanged as the sample ages. This is consistent again with fast relaxation of the non-aggregated monomers. The second peak, on the other hand, is sensitive to the stage of aggregation, i.e. the initial positions of the peak gradually shift from around  $30600\text{ cm}^{-1}$  to  $30000\text{ cm}^{-1}$  within 169 hrs. The positions of the peak  $v_2(t)$  of the sample at different ages exhibit an initial decrease followed by an increase after about 6 ns. Such behavior suggests that it represents at least two types of aggregates with each having different peaks of emission spectra and different decay rates. In older samples ( $>96$  hours)  $v_2(t)$  has no increasing stage, which indicates again the fluorescence of one rather than two fluorescent species. This may be explained by larger aggregates having very low fluorescence emission due to reabsorption or by precipitation of the larger fibrils.

The analysis of the  $C_1(t)$  and  $C_2(t)$  functions obtained for both samples (Figure 27) provides additional clues. In the free  $A\beta_{1-40}$  sample the  $C_1(t)$  (monomers, Figure 27a) decays in the

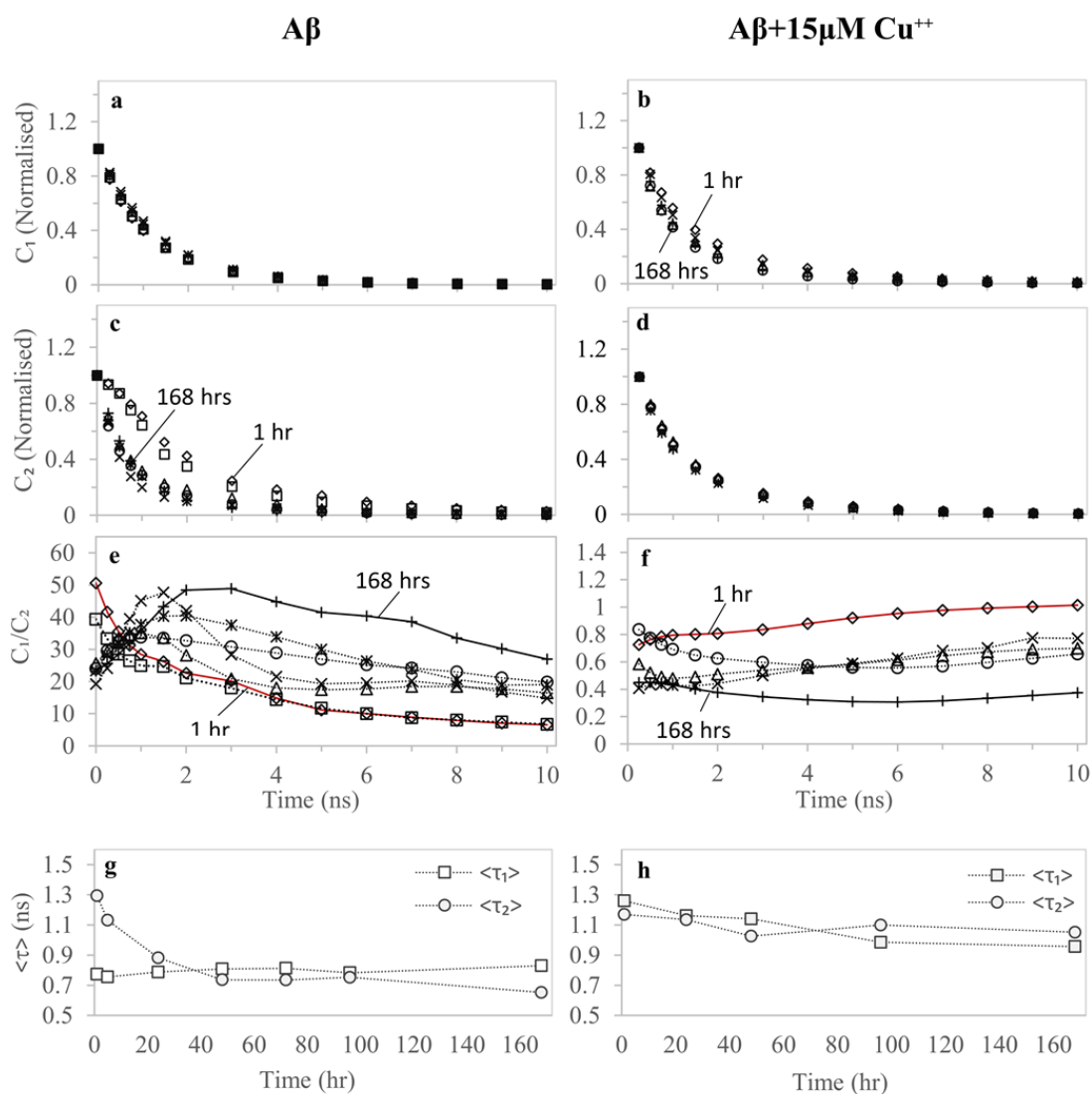


**Figure 27.** Fluorescence intensity decay of the two components  $C_1(t)$  and  $C_2(t)$  for free  $A\beta_{1-40}$  (a,c) and  $A\beta_{1-40}$  with 15  $\mu\text{M}$  of  $\text{Cu}^{2+}$  (b,d); The ratio of the monomer to oligomer contribution  $C_1(t)/C_2(t)$  plotted against time for free  $A\beta_{1-40}$  (e) and  $A\beta_{1-40}$  in the presence of 15  $\mu\text{M}$  of  $\text{Cu}^{2+}$  (f) at different stages of aggregation ( $\diamond$  1hr,  $\square$  5hr,  $\Delta$  24hr,  $\times$  48hr,  $*$  72hr,  $\circ$  96 hr and  $+$  168 hr).<sup>153</sup>

similar way irrespectively of the age of the sample, while the character of the  $C_2(t)$  (oligomers, Figure 27c) alters when sample ages. The initial ratio  $C_1(0)/C_2(0)$  (Figure

27e) demonstrates the domination of the monomer's emission, which decreases as the sample ages due to oligomer formation. We note that the  $C_1(t)/C_2(t)$  plots are highly sensitive to the stage of aggregation, and thus can be used as indicators of A $\beta_{1-40}$  aggregation stage.

The decays  $C_1(t)$  and  $C_2(t)$  in the copper containing sample (Figure 27b, d, and f) show that the character of A $\beta_{1-40}$  aggregation is dominated by the presence of copper ions from the very beginning. The characters of the decays  $C_1(t)$  and  $C_2(t)$  are similar and do not change substantially while the sample ages (Figure 27b and d). The ratio  $C_1(t)/C_2(t)$  is substantially smaller and quite stable as compared to the no-Cu<sup>2+</sup> sample and decreases with sample aging. Moreover, the contribution of the second peak is significantly higher than that observed in free A $\beta_{1-40}$  (Figure 27e, f), which suggests that the formation of A $\beta$  aggregates is intensively triggered by Cu<sup>2+</sup>. The contribution of the second peak slightly increases as the sample ages. This might be a result of large aggregate precipitation or because of their low quantum yields.

### 7.3. Conclusion

To conclude, the time-resolved studies of free Tyr and Tyr in A $\beta$  fragments show that Cu<sup>2+</sup> at  $\mu$ M concentrations does not quench Tyr fluorescence. The formation of Cu<sup>2+</sup>-A $\beta_{1-40}$  complexes, however, substantially accelerates the process of peptide aggregation. TRES measurements show that A $\beta$  aggregates in the presence of Cu<sup>2+</sup>, exhibit considerable shifts in their emission peak during peptide aggregation. Such behavior suggests that A $\beta_{1-40}$  peptides exhibit different aggregation pathways and form different types of aggregates when Cu<sup>2+</sup> is present.

We believe that the observed substantial differences in the A $\beta_{1-40}$  and A $\beta_{1-40}$ -Cu<sup>2+</sup> time-resolved fluorescence responses offer the possibility for identifying different types of

amyloid aggregates induced by the presence of specific factors, e.g. sugars (glycation), environmental conditions, anti-aggregation compounds, etc. The TRES parameters recovered in our approach can be used to propose a possibly broad selection of the potential models of the kinetics. Determining the specific type of aggregates would be then based on the best-fitting kinetic model and values of its parameters. Due to the expected complexity of these models, their numerical solutions would have to be calculated and fitted to the experimental decays. Our preliminary attempts to fit the numerical model solutions to the experimental decay data demonstrate the full feasibility of such an approach. This strategy can be beneficial for all complex biological systems, where the dogmatic use of multi-exponential models of the decays can be inefficient and not insightful

## 8. Detecting beta-amyloid glycation by fluorescence of intrinsic tyrosine

### 8.1. Introduction

Alzheimer's disease (AD) is the most common cause of dementia. Currently there is no general agreement on what activates the progression of AD, multiple triggering events in the early stages of AD have been suggested. They all appear to converge to a few final pathways in the late stages, which lead to the inflammation and neurodegeneration that characterise the condition. The triggering compounds investigated included metal ions (e.g. Cu, Zn and Fe ions)<sup>144,145</sup> and glycation factors (e.g. glucose<sup>154</sup> and fructose<sup>155</sup>).

In this chapter we are mostly concerned with the involvement of advanced glycation end products (AGE) in AD pathogenesis. AGEs relation with brain aging and AD was first proposed in the mid-1990s<sup>156</sup>. AGEs accumulate in cells and tissues, however they are accelerated in the case of AD. Several studies have shown that patients with diabetes show a greater deposition of AGEs in the brain and receptors for AGEs (RAGE)<sup>156,157</sup>. Therefore, it is widely accepted that AGEs are active participants in the progression of AD<sup>158-161</sup>. More importantly, recent studies have demonstrated that glycated beta-amyloids (A $\beta$ ), a naturally occurring peptide capable of binding to sugars and resulting in the formation of AGEs, are more toxic than non-glycated A $\beta$  amyloids<sup>16,162</sup>, i.e. it was found that A $\beta$ -AGE were more active than A $\beta$  in decreasing cell viability (e.g. 8-DIV embryonic hippocampal neurons), increasing cell apoptosis, inducing Tau hyperphosphorylation, and reducing synaptic proteins<sup>16</sup>. In vivo studies performed on rats<sup>162</sup> show that A $\beta$ -AGE exacerbates A $\beta$ -mediated cognitive impairment and neuropathology.

Detecting the aggregation of glycosylated and non-glycosylated A $\beta$  amyloids can be challenging particularly at the early stages of this process. Most techniques that have been used to study A $\beta$  glycation such as atomic force microscopy (AFM)<sup>15,163,164</sup>, electron microscopy<sup>165</sup>, dynamic light scattering (DLS)<sup>15</sup>, circular dichroism (CD)<sup>15,16</sup> and Thioflavin T (ThT)-based fluorometry<sup>100</sup> are evidently sensitive to fibril formation (i.e. the formation of A $\beta$  beta-sheets). However, they lack the specificity to detect A $\beta$  oligomerization. This drawback hinders the progress in understanding of what triggers the progression of AD and how the symptoms associated with the disease can be prevented.

The accepted model describing the aggregation of the most abundant form A $\beta$ <sub>1-40</sub> is the nucleation-dependent polymerization model, which is characterized by two distinct stages: a lag phase, followed by a rapid elongation phase. Conventional methods typically used to study this reaction (i.e. ThT-based fluorimetry) are reporting fibril formation but are not sensitive to events taking place early in the lag phase, promoting the assumption that only A $\beta$  monomers and large oligomers exist at early stages and that the lag time is defined by the primary nucleation rate only. However, the existence of oligomer intermediates prior to fibril formation has been confirmed by AFM, electron microscopy and dynamic DLS<sup>15,154,156,161,162,166-168</sup>. Although the oligomers are considered to be more toxic than mature insoluble fibrils<sup>168,169</sup>, there are only few attempts to quantify the extent of oligomer formation, determine whether they are kinetically competent to form amyloid fibrils or to identify the mechanism by which oligomers trigger neurodegeneration. Here we attempt to address these tasks by using sensing potential of the intrinsic Tyrosine fluorescence.

Most researchers track amyloid- $\beta$  aggregation reactions using extrinsic fluorophores mostly because such a fluorescence capability is available in most laboratories. ThT

fluorescence is commonly used to detect A $\beta$  aggregation even though it cannot detect early oligomer formation<sup>29-31</sup>. Recent reports suggest the usefulness of the fluorophore 1,1'-bis(anilino)-4,4'-bis(naphthalene)-8,8'-disulfonate (bis-ANS) for the detection of A $\beta$  aggregation, however, there is no agreement on whether bis-ANS binds most strongly with oligomers<sup>32</sup> or fibrils<sup>33</sup>. Another disadvantage of using extrinsic fluorophores in amyloid aggregation studies is the fact that the ratio of fluorophore to A $\beta$  can significantly influence the obtained results<sup>33</sup>. Moreover, it has been reported that some extrinsic fluorophores such as bis-ANS<sup>33</sup> and ThT<sup>36</sup> might affect the nucleation rate in some cases, or even prevent aggregation<sup>37</sup>.

In this chapter, we use TRES to investigate the fluorescence of Tyr in A $\beta$ <sub>1-40</sub> in the presence of high glucose concentrations. Our objective was to investigate fluorescence changes caused by both peptide glycation and aggregation to reveal the impact of glycation on A $\beta$ <sub>1-40</sub> oligomerisation. In order to cause aggregation and glycation occurring in the similar time scales, we have chosen higher than physiological concentration of glucose (50 mM).

## **8.2. Results and discussion**

Steady-state fluorescence spectra were obtained for A $\beta$ <sub>1-40</sub> with and without high glucose (Figure 28). The samples were measured using different excitation wavelengths and at different stages of aggregation. The spectra observed at excitation 279 nm (Figure 28a) for both samples is the typical spectrum of Tyr. As the samples age, the fluorescence intensity decreases and the spectrum of the sample with glucose exhibits a considerable change in its shape.

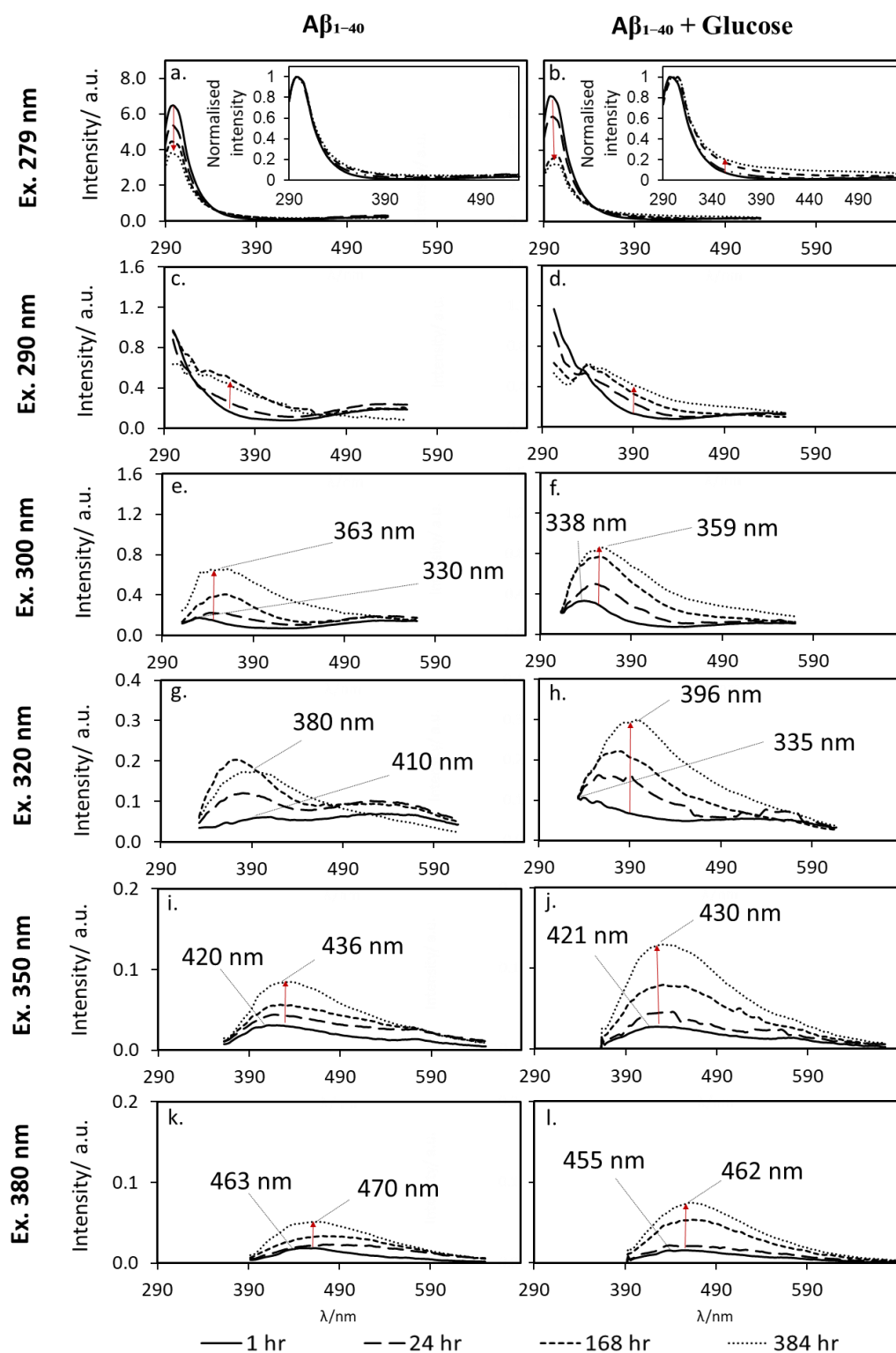


**Figure 28.** Fluorescence spectrum of 50  $\mu$ M  $A\beta_{1-40}$  in PBS buffer (10 mM, pH 7.4) measured in the absence (left) and presence (right) of 50 mM glucose at excitation wavelengths 279 nm (a, b), 290 nm (c, d), 300 nm (e, f), 320 nm (g, h), 350 nm (i, j) and 380 nm (k, l) and after incubation for 1 h (solid), 24 h (long-dash), 168 h (short-dash) and 384 h (dotted). The arrow shows direction of the flow of time (measurements taken at 1 h, 24hrs, 168 h and 386 h after sample preparation). Normalised emission spectra of both samples at excitation wavelength 279 nm are shown in a and b insets. Raman peaks were removed by subtracting a solvent baseline from the emission spectra.<sup>138</sup>

Although Tyr doesn't absorb light at wavelengths above 300 nm, when Tyr in A $\beta$ <sub>1-40</sub> is excited at wavelengths  $\geq 300$  nm fluorescence peaks are observed at higher wavelengths.

Figure 29 shows the emission of A $\beta$ <sub>1-40</sub> in the absence and presence of glucose.

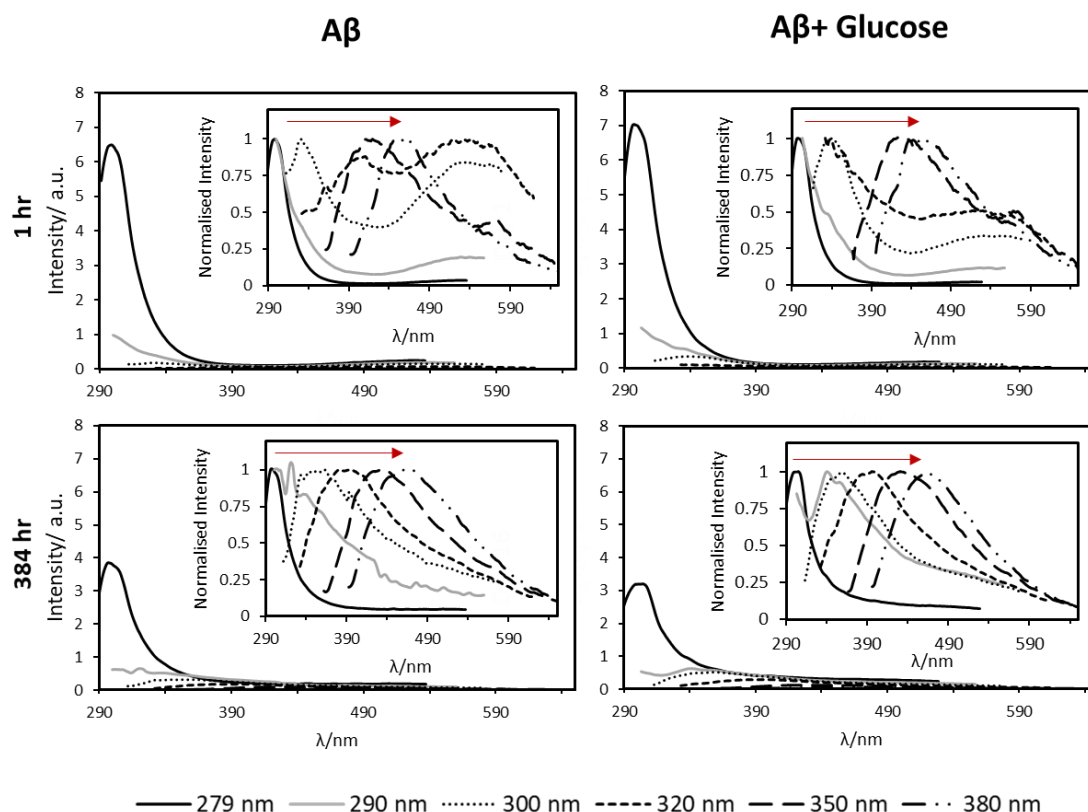


**Figure 29.** Steady-state measurements of 50  $\mu$ M A $\beta$ <sub>1-40</sub> in PBS buffer (10 mM, pH 7.4) in the absence (left) and presence (right) of 50 mM glucose at excitation wavelengths 279 nm (solid black), 290 nm (solid grey), 300 nm (dotted), 320 nm (short-dash), 350 nm (long-dash) and 380 nm (dash-dot-dot) after incubation for 1 h (top) and 384 h (bottom). Insets show the normalised emission spectra. Raman peaks were removed by subtracting a solvent baseline from the emission spectra.<sup>138</sup>

In general, the emission is time and excitation-wavelength dependent. At the excitation wavelengths  $\geq 300$  nm the position of the emission peak increases with the excitation wavelength and the spectrum peak position moves towards red with time. These observations suggest that A $\beta$ 's monomers aggregate and form at least one fluorescent complex within a few hours, and a variety of complexes with a broad distribution of sizes, as evidenced by the excitation wavelength-emission peaks correlation, form within

a few days. This may be explained by the diversity of tyrosine energy levels caused by the gradual formation of small and then larger oligomers, beta-sheets and fibrils. It should also be noted here that there is a possibility of microbial contamination, which might interfere with A $\beta$ 's fluorescence spectra during the aggregation process.

TRES measurements were performed for A $\beta_{1-40}$  (50  $\mu$ M) at several stages of aggregation, namely 1, 5, 24, 48, 72, 96 and 168 hrs after sample preparation (the number indicates the age of the sample when each series of measurements is started).

Figure 30 shows an example of TRES at two stages of aggregation: 1 and 168 hours from sample preparation in the absence and presence of glucose (50 mM). Experimental data were fitted to a model based on the Toptygin and Brand [32] approach, which assumes that the fluorescence spectrum  $I(\nu)$  of a single fluorescent residue can be expressed as  $\sim \nu^3 g(\nu)$ , where  $g(\nu)$  is the Gaussian distribution function. Consequently, the spectrum of a sample with  $N$  fluorescent residues would be described by the sum of  $N$  normalised functions of the type  $\sim \nu^3 g(\nu)$  (Equation 49).

In our previous work<sup>143</sup> we have demonstrated that the spectra of free A $\beta_{1-40}$  can be sufficiently described by two peaks. The presence of non-aggregating monomers and aggregating oligomers in the sample explains this double-peak structure of the spectra. Note that we only study the fluorescence decays of the Tyr residues excited at 279 nm, not the fluorescent products of oligomerisation, which require longer excitation wavelengths and their fluorescence intensities are too low for detecting fluorescence intensity decays using traditional time-correlated single photon counting (TCSPC) instrumentation. The red shifts observed for each peak individually<sup>143</sup> represent two different rates of dielectric relaxation. The TRES of A $\beta_{1-40}$  with glucose also demonstrated the presence of two components ( $N=2$ ). For the purpose of understanding

the underlying fluorescence kinetics of A $\beta$ <sub>1-40</sub> in the presence of 50 mM of glucose, we compared the parameters obtained from fitting the model TRES (Equation (49) for  $N=2$ ) to the experimental data of A $\beta$ <sub>1-40</sub> with glucose with those recovered from the sample without glucose.

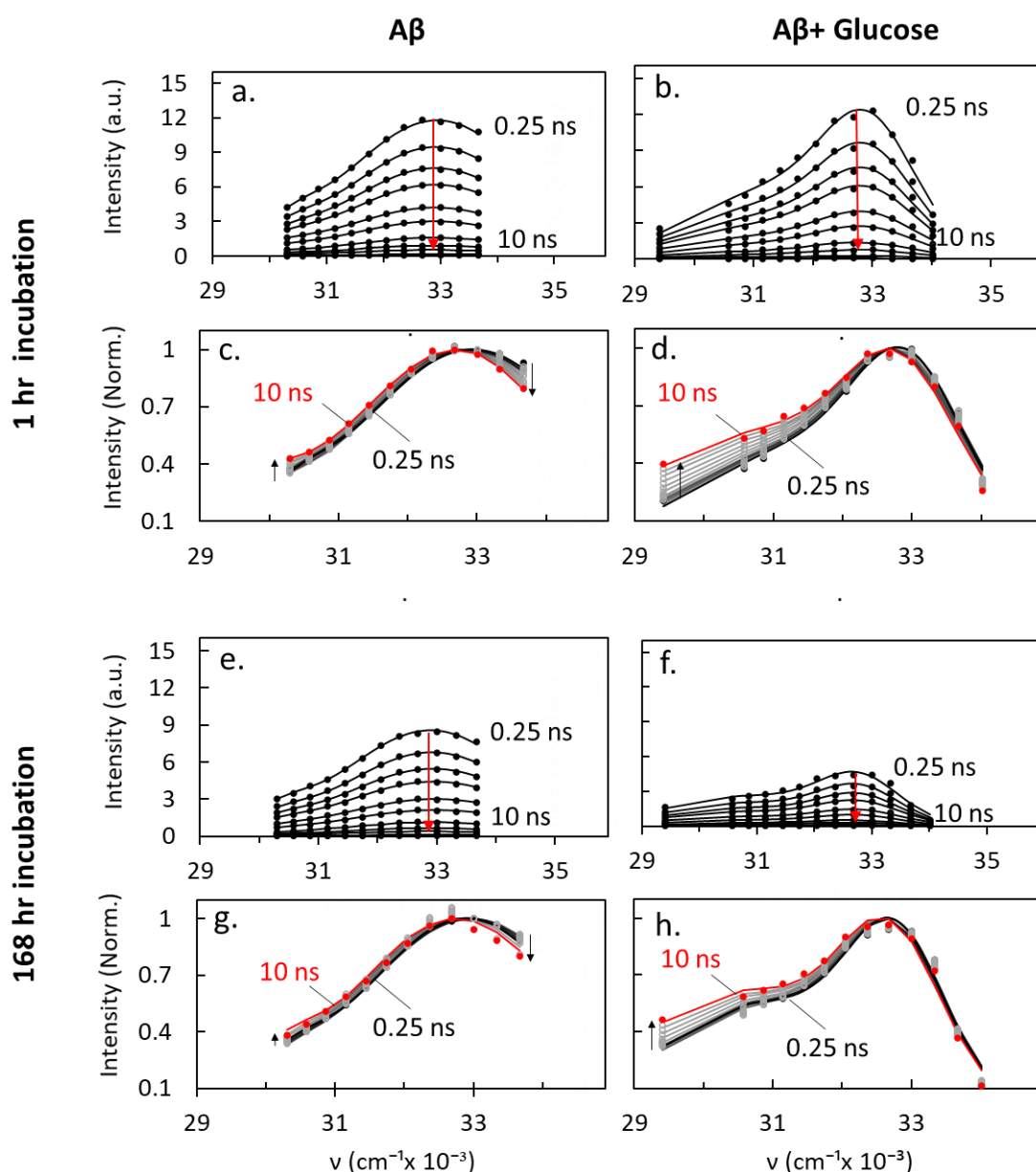


**Figure 30.** Time-resolved emission spectra (TRES) obtained for 50  $\mu$ M A $\beta$ <sub>1-40</sub> in HEPES buffer (0.1  $\mu$ M, pH 7.4) after 1hr of incubation (a) and 168 h of incubation (e). TRES obtained for 50  $\mu$ M A $\beta$ <sub>1-40</sub> in the presence of 50 mM glucose after 1 h of incubation (b) and 168 h of incubation (f). Normalised TRES for A $\beta$ <sub>1-40</sub> in the absence and presence of glucose after 1hr of incubation (c,d) and 168 h of incubation (g,h) The solid lines represent the two-to-typtigin type functions fits.<sup>138</sup>

Figure 31 illustrates the position of the two peaks  $\nu_1(t)$  and  $\nu_2(t)$ , recovered from fitting equation (49) to experimental TRES, in the presence and absence of glucose. Position of the first peak  $\nu_1(t)$  for samples with and without glucose is located at  $\sim 33000 \text{ cm}^{-1}$  at  $t=0$ .  $\nu_1(t)$  in both samples exhibit nearly no changes over 10 ns after excitation, which indicates that dielectric relaxation is very fast, thus nearly completed before fluorescence occurs. The location of the peak in the spectra and the fast dielectric relaxation is consistent with monomers being responsible of this emission. This also demonstrates the characteristic resemblance in the behaviour of this peak in the samples with and without glucose.

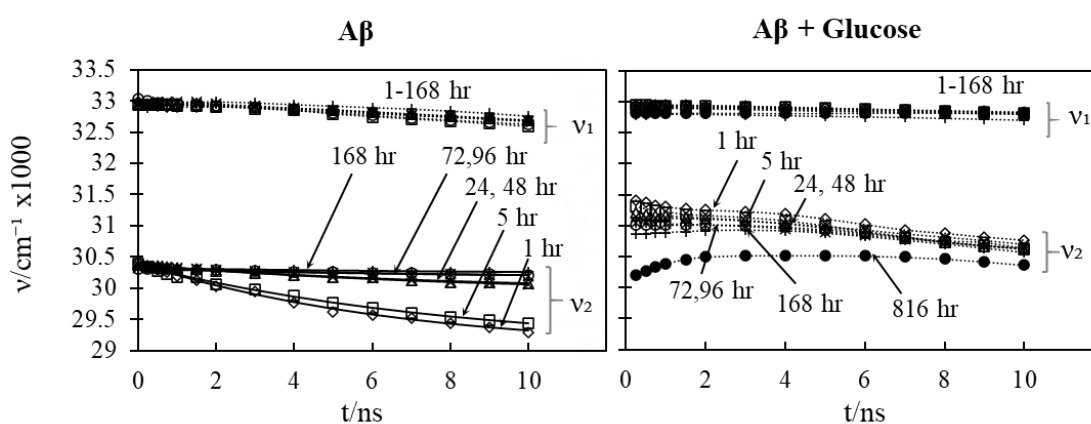


**Figure 31.** Peak's position  $\nu_1(t)$  and  $\nu_2(t)$ , obtained from fitting A $\beta$ 1-40 TRES to equation (49), plotted against time in nanoseconds at different stages of aggregation (1 h, 5 h, 24 h, 48 h, 72 h, 96 h and 168 h) for sample with and without glucose.<sup>138</sup>

The second peak  $\nu_2(t)$  is highly influenced by the presence of glucose as shown in Figure 31. Its position in a no-glucose sample is located at  $\sim 30500 \text{ cm}^{-1}$  at  $t=0$ . The changes observed in the position of  $\nu_2(t)$  during 10 ns after excitation varies depending on the age of the sample. When the sample is 1 hr old, we observe an exponential shift, caused by dielectric relaxation, from  $\nu_2(0) \approx 30500 \text{ cm}^{-1}$  to  $\nu_2(\infty) \approx 29000 \text{ cm}^{-1}$  with the dielectric relaxation time  $\tau_R = 6.7 \text{ ns}$ . As the sample aggregation progresses the relaxation time  $\tau_R$  increases and the red shift decreases, which can be explained by gradual growth in the

size of the aggregates. We attribute this component to oligomers because aggregation explains why the initial position of the peak  $\nu_2(0)$  appears at a substantially lower energy value ( $30500\text{ cm}^{-1}$ ) and explains the red shift after excitation.

In the presence of glucose,  $\nu_2(t)$  behaves in a different manner (Figure 31). The initial position of the second peak  $\nu_2(0) \approx 31500\text{ cm}^{-1}$  for a fresh sample and gradually decreases as the sample ages. The position of the second peak  $\nu_2(t)$  shifts towards lower energies within 10 ns but not exponentially as observed in free  $A\beta_{1-40}$ . This might indicate that this peak represents more than one component where each has its own intensity decay and dielectric relaxation rate. The initial position of the peak and its behaviour in the nano-second time scale might be a result of  $A\beta_{1-40}$  binding to glucose and/or alterations in the  $A\beta_{1-40}$  aggregation pathway caused by the presence of glucose.

Further insights on the development of oligomerisation of both samples can be obtained from the analysis of other parameters extracted from fitting equation (49) to the data. The  $C_1(t)$  and  $C_2(t)$  functions represent the fluorescence intensity decay of each component individually (Figure 32a and b). In the free  $A\beta_{1-40}$  sample,  $C_1(t)$  decays with a characteristic lifetime  $T_1$  regardless of the samples actual age (Figure 32d). This corresponds with our previous assumption that the  $C_1(t)$  component is mostly monomers. The characteristic lifetime  $T_2$  of the decay  $C_2(t)$ , however, decreases with aggregation. The initial value of the ratio  $C_1(0)/C_2(0)$  indicates the dominance of monomer's emission, which then slightly decreases with time, indicating that aggregates are being formed.

The ratio  $C_1(0)/C_2(0)$  cannot be associated directly with the concentration of monomers and oligomers in the sample because it is likely that the quantum yield of Tyr in a monomer is reduced to some extent when the monomers aggregate and form oligomers.

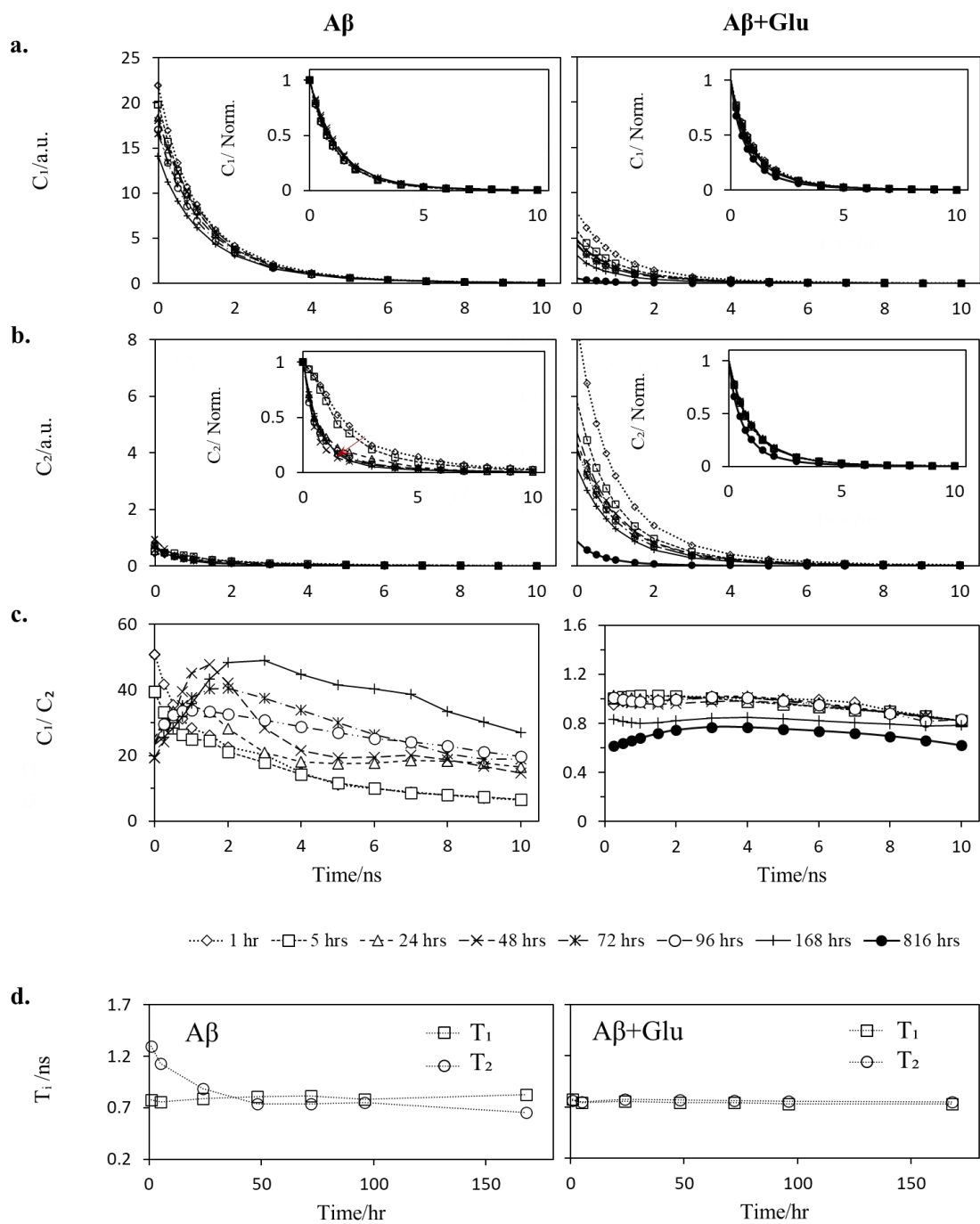


**Figure 32.** The fluorescence intensity decays of the two emitting species; monomers  $C_1(t)$  (a) and oligomers  $C_2(t)$  (b), obtained from fitting TRES to equation (49), and the ratio of monomer to oligomer contribution  $C_1(t)/C_2(t)$  (c) in the absence (left) and presence (right) of glucose. The characteristic fluorescence lifetimes of monomers  $T_1$  and oligomers  $T_2$  (d) in the absence (left) and presence (right) of glucose.<sup>138</sup>

Nevertheless, the  $C_1(t)/C_2(t)$  plot for free  $A\beta_{1-40}$ , shown in Figure (32c), is highly sensitive to the age of the sample and can be used to indicate the stage of  $A\beta_{1-40}$  aggregation.

In the presence of glucose, however,  $C_1(t)$  and  $C_2(t)$  decay with similar and constant rates at least during the first 168 hrs (Figures 32a, b and d). However, when the sample is 816 hr old,  $C_2(t)$  decays much faster. The ratio  $C_1(0)/C_2(0) \approx 1$  indicating that, in the presence of glucose, monomers contribute to only 50% of the emission, which is considerably low compared with the free  $A\beta_{1-40}$ . The ratio of  $C_1(0)/C_2(0)$  in sample with glucose remains constant for the first week then starts to decrease after 168 hrs (Figure 32c). The intensity  $C_1(0)$  and  $C_2(0)$  both decrease as the sample ages (Figures 32a and b). The decrease observed in the  $C_1(0)$  value is mostly because the number of monomers is reduced due to aggregation. The decrease in  $C_2(0)$ , on the other hand, might be a result of Tyr having a constantly changing quantum yield due to glucose-mediated aggregation. Unlike in the free  $A\beta_{1-40}$ , the  $C_1(t)/C_2(t)$  plot is not sensitive to the age of the sample especially during the first 96 hrs (Figure 32c).

### 8.3. Conclusions

Steady state spectra measurements reveal a variety of complexes formed during  $A\beta_{1-40}$  oligomerisation, which also appear in the presence of glucose but at a much faster rate. The decrease observed in the Tyr peak ( $\lambda_{\max} \approx 304$  nm) when excited with 279 nm is most likely a result of the decrease in the concentration of  $A\beta_{1-40}$  monomers over 384 hr. In contrast, the increase observed in peaks ( $\lambda_{\max} \approx 330-445$  nm) excited with wavelengths  $\geq 300$  nm and their shift towards the red within 384 hr indicates the formation of aggregates, which grow in number and size. The peak observed at 540 nm absorbs light between 279 and 320 nm and its location and intensity remain constant for both samples.

We associate this peak with small complexes of  $A\beta_{1-40}$ . TRES measurements show that at excitation 279 nm, free  $A\beta_{1-40}$  exhibits two forms of fluorescent species; monomers and a single type of aggregates that grows gradually and undergoes dielectric relaxation with rates that are basically controlled by the size of the aggregate. In the presence of glucose, we believe that there are more than two fluorescent species: the typical monomers observed in free  $A\beta_{1-40}$ , but at much lower concentrations, and more than one type of oligomers each with its own fluorescence intensity decay and dielectric relaxation rate. This demonstrates that glucose alters the aggregation pathway. These changes are highly relevant to our understanding of the pathophysiology of AD and the implication of AGE and diabetes in these pathways. Such an understanding and disease modelling may aid testing of interventions including pharmacotherapies that may ameliorate disease progression.

## 9. Investigating the effect of quercetin on beta-amyloid aggregation by time resolved emission spectra (TRES)

### 9.1. Introduction

Flavonoids consist of a large group of polyphenolic compounds having a benzo- $\gamma$ -pyrone structure and are ubiquitously present in plants. To date, more than 8000 varieties of flavonoids have been identified<sup>170,171</sup>. One important subclass of flavonoid, the flavonols, and their major representative quercetin are the most prevalent flavonoids in the human diet<sup>172-174</sup>. They occur in many vegetables and fruits such as onions, curly kale, broccoli, blueberries and apples as well as in red wine, tea and cocoa.

Quercetin, has gained much scientific attention due to its antioxidant and metal ion-chelating properties<sup>175-178</sup> and its capacity to inhibit amyloid fibril formation<sup>179</sup>. Many human neurodegenerative diseases such as Alzheimer's and Parkinson's disease are associated with amyloid fibril formation, thus quercetin is widely researched for its therapeutic potential in providing better treatment for neurodegenerative diseases.

Quercetin has been reported to exert antioxidant activity due to the catechol group in the beta ring and the -OH group located in positions 3 and 5 of the AC ring<sup>180</sup> (Figure 33a). It is also suggested that quercetin might indirectly inhibit the formation of A $\beta$  peptides by constraining the activity of the  $\beta$ -site APP cleaving enzyme (BACE-1)<sup>181</sup> (chapter 1). Studies have shown that OH groups and phenolic rings in flavonoids are essential for the non-covalent interactions with  $\beta$ -sheet structures, which are common to all amyloid proteins<sup>182</sup>. Studies on quercetin in particular have pointed out that it has the potential of inhibiting A $\beta$  aggregation by forming hydrophobic interactions and hydrogen bonds with the formed  $\beta$ -sheets<sup>181</sup>. More interestingly, it has been reported that quercetin has the ability to destabilise preformed fibrils in some proteins such as bovine insulin<sup>183</sup>,  $\alpha$ -

Synuclein<sup>184</sup> and A $\beta$ <sub>25-35</sub><sup>185</sup> in a dose-dependent manner, and transform them into amorphous aggregates<sup>183</sup>. The final morphologies of protein assemblies in the presence of quercetin are different and require further examination for better characterisation.

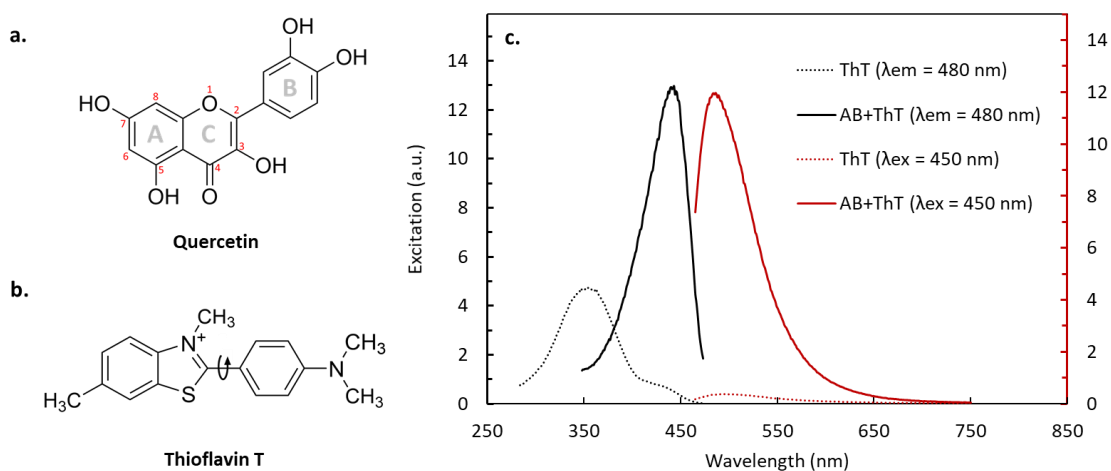


**Figure 33.** The chemical structure of quercetin (a) and Thioflavin T (b). Fluorescence excitation (black) and emission (red) spectra of equal concentrations of ThT alone in HEPES buffer (dotted line) and ThT with A $\beta$ <sub>1-40</sub> in the same buffer (solid line) measured after 72 hr of incubation.

Here we research A $\beta$ <sub>1-40</sub> interactions with Quercetin and its effect on the aggregation pathway using time-resolved intrinsic Tyr<sub>10</sub> fluorescence. This non-invasive technique with sub-nano meter and sub- nano second resolution is uniquely sensitive to early stages of aggregation and can provide further insight on early A $\beta$ <sub>1-40</sub>-Quercetin interactions.

For a broader and more comprehensive understanding of changes observed in Tyr<sub>10</sub> fluorescence intensity decay in A $\beta$ <sub>1-40</sub> we measure TRES, which can sufficiently demonstrate structural changes occurring within nanoseconds after excitation as shown previously (section 6.2).

In order to test the direct effect of quercetin on Tyr in A $\beta$  in the absence of amyloid aggregation, we extended the lifetime measurements to include shorter fragments of the full-length peptide such as A $\beta$ <sub>1-11</sub> and A $\beta$ <sub>1-16</sub>. These peptides contain the single Tyr

residue, but lack the hydrophobic C-terminal of A $\beta$ <sub>1-40</sub>, which is critical in triggering the transformation from  $\alpha$ -helical to  $\beta$ -sheet structure and plays a key role in protein aggregation<sup>186</sup>.

A $\beta$ <sub>1-40</sub> fibril formation was monitored by the Thioflavin T (ThT) binding assay. Thioflavin T (ThT) is currently considered the gold-standard fluorescent probe for the study of amyloid fibril formation. Upon binding to  $\beta$ -sheet-rich structures, ThT gives a strong fluorescence signal at 482 nm when excited at 450 nm. The mechanism by which ThT fluorescence is enhanced upon binding to amyloids has been ascribed to the rotational immobilization of the C–C bond between the benzothiazole and aniline rings<sup>187,188</sup> (Figure 33b), which results in a dramatic shift in the ThT excitation maximum from 350 nm to 450 nm as shown in figure (33c). Although ThT is an efficient reporter of fibril formation, its poor photophysical and binding properties makes it poorly suited for detection of small oligomeric species<sup>33</sup>. Thus, the ThT assay is used here as a complementary technique, but only to confirm the formation of A $\beta$ <sub>1-40</sub> fibrils.

## 9.2. Results and discussion

Steady-state emission spectra and fluorescence lifetime of Tyr in A $\beta$ <sub>1-11</sub> and A $\beta$ <sub>1-16</sub> has been measured with increasing concentration of quercetin (0, 25, 50, 200  $\mu$ M). The objective of these measurements was to determine whether quercetin can affect Tyr emission directly. Steady state results show that increasing the concentration of quercetin up to 200  $\mu$ M in a 50  $\mu$ M A $\beta$ <sub>1-11</sub> sample slightly reduces the intensity of Tyr emission (Figure 34a). The emission of the 50  $\mu$ M A $\beta$ <sub>1-16</sub> sample, on the other hand, remains relatively constant with increase in quercetin concentration from 0 to 50  $\mu$ M. However, at extremely high concentrations of quercetin (200  $\mu$ M ) the emission of A $\beta$ <sub>1-16</sub> is considerably reduced (Figure 34b).

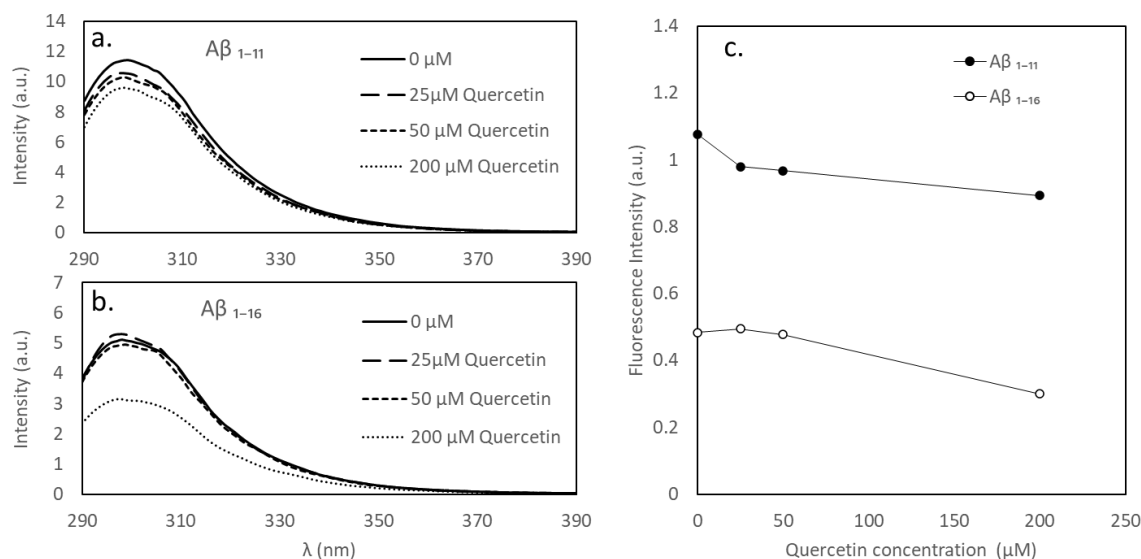


**Figure 34.** Emission spectra of Aβ<sub>1-11</sub> (a) and Aβ<sub>1-16</sub> (b) in the absence (solid line) and presence of 25 μM (long dash) , 50 μM (short dash) and 200 μM (dotted) of quercetin. Maximum fluorescence intensity of Aβ<sub>1-11</sub> (black circle) and Aβ<sub>1-16</sub> (white circle) as function of quercetin concentration (c).

Fluorescence intensity decays of both Aβ<sub>1-11</sub> and Aβ<sub>1-16</sub> were best fitted to a 3-exponential model. Parameters obtained from fitting the model are shown in figure (35) the decay times  $\tau_1$ ,  $\tau_2$  and  $\tau_3$  and their respective percentage contributions  $f_1$ ,  $f_2$  and  $f_3$  for Tyr in both the Aβ<sub>1-11</sub> and Aβ<sub>1-16</sub> sample showed no significant change with increase in quercetin concentration. This suggest that the decrease in Aβ<sub>1-11</sub> and Aβ<sub>1-16</sub> emission is due to inner filter effects caused by high concentration of quercetin. To avoid such effects, quercetin was kept at concentrations below 50 μM.

TRES were obtained for a sample of Aβ<sub>1-40</sub> in the absence and presence of 15 and 50 μM quercetin. Figure (36) shows TRES measured after 1hr and 142 hr of incubation at 37 °C. comparing our current sample with previous Aβ<sub>1-40</sub> TRES measurements we believe that our current sample (Batch 2) contains a considerable amount of preformed aggregates.

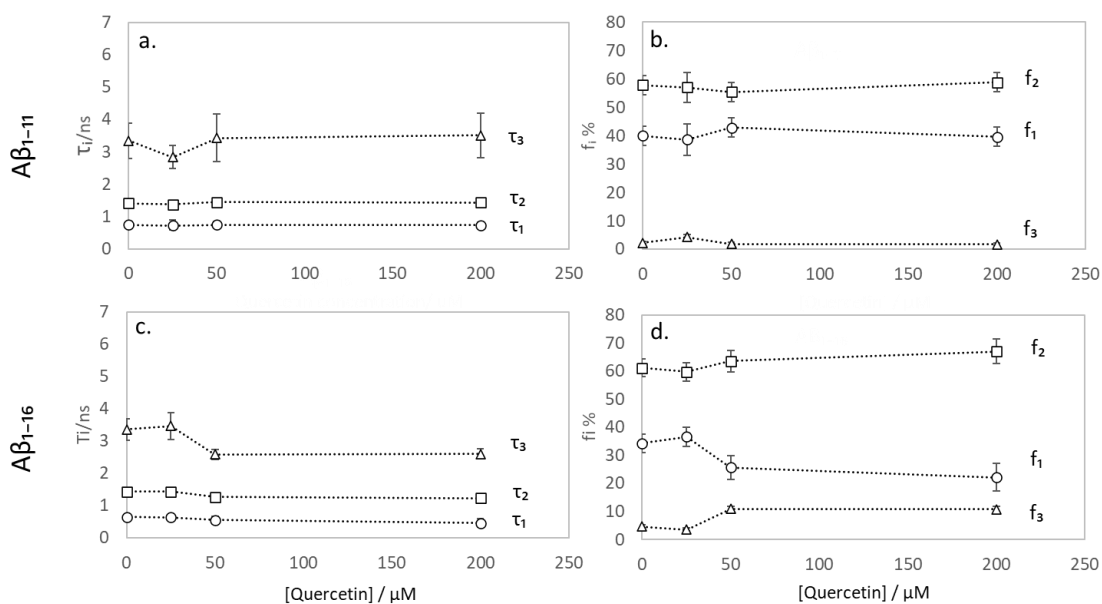


**Figure 35.** Parameters obtained from fitting Tyr's fluorescence decay in a 50  $\mu\text{M}$   $\text{A}\beta_{1-11}$  (a,b) and  $\text{A}\beta_{1-16}$  (c,d) solution to a three-exponential decay model plotted against Quercetin concentration: Tyr fluorescence decay times  $\tau_1$ ,  $\tau_2$  and  $\tau_3$  in  $\text{A}\beta_{1-11}$  (a) and  $\text{A}\beta_{1-16}$  (c), percentage contributions  $f_1, f_2$  and  $f_3$  in  $\text{A}\beta_{1-11}$  (b) and  $\text{A}\beta_{1-16}$  (d). Error bars represent 3 x standard deviation.

TRES of  $\text{A}\beta_{1-40}$  were sufficiently represented by two peaks in our previous studies (Batch 1). Each peak assumingly corresponds to either monomers or oligomers while its height or area corresponds to its relative fluorescence emission. TRES of the current  $\text{A}\beta_{1-40}$  sample (Batch 2) also demonstrated the presence of two components ( $N=2$ ).

Adding 15 or 50  $\mu\text{M}$  of quercetin to the  $\text{A}\beta_{1-40}$  sample had no significant impact on the double-peak structure of the spectra. The model TRES (Equation (49) for  $N=2$ ) seems to fit the experimental data of the current sample of  $\text{A}\beta_{1-40}$ , with or without quercetin, well. Parameters obtained from fitting this model to the experimental data of  $\text{A}\beta_{1-40}$  in the absence and presence of Quercetin may provide useful information that could help understand the underlying fluorescence kinetics of  $\text{A}\beta_{1-40}$  in the presence of quercetin.

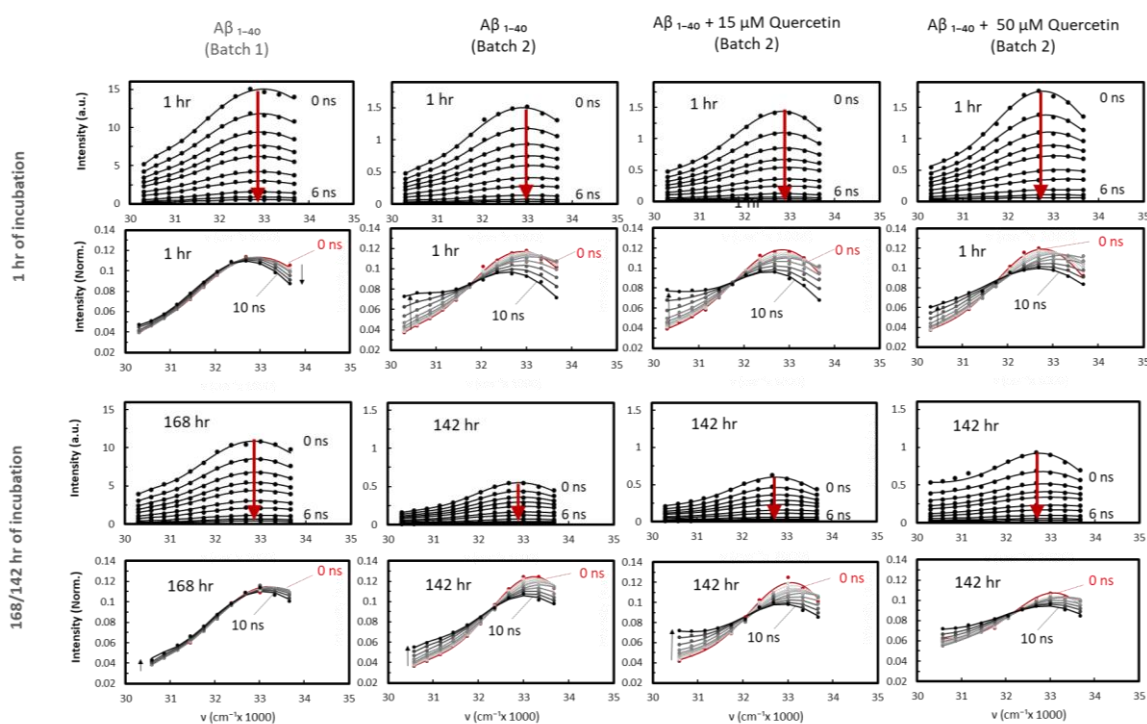


**Figure 36.** Time-resolved emission spectra (TRES) obtained for 50  $\mu\text{M}$   $\text{A}\beta_{1-40}$  in HEPES buffer (pH 7.4) in the absence (batch 1 and 2) and presence of two different concentrations of quercetin 15 and 50  $\mu\text{M}$  (batch 2) after 1 hr of incubation and 142/168 hr of incubation. The solid lines represent the two-Toptygin type functions fits.

In our previous work we have demonstrated that dielectric relaxation is one of the factors determining the excited-state kinetics and affects the time resolved fluorescence spectrum and that it can be observed on a ns time scale. All these processes can be detected by means of the evolution of TRES.

Figure (37) shows the position of the two peaks  $v_1(t)$  and  $v_2(t)$ , recovered from fitting equation (49) to experimental TRES of  $\text{A}\beta_{1-40}$  sample starting from a monomer solution (Figure 37a) and an  $\text{A}\beta_{1-40}$  sample containing preformed aggregates (Figure 37b) in the absence and presence of two different concentrations of quercetin; 15 and 50  $\mu\text{M}$  (Figure 37c, d). We associate the peak located at  $\sim 33000 \text{ cm}^{-1}$  at  $t=0$  with monomers. The position of this peak  $v_1(t)$  exhibits nearly no changes in the sample of  $\text{A}\beta_{1-40}$  with no preformed aggregates, which indicates weak dielectric relaxation effects. In this case the

$A\beta_{1-40}$  peptide is small in size and exposed to water molecules, thus the dielectric relaxation process is fast and nearly completed when fluorescence occurs.

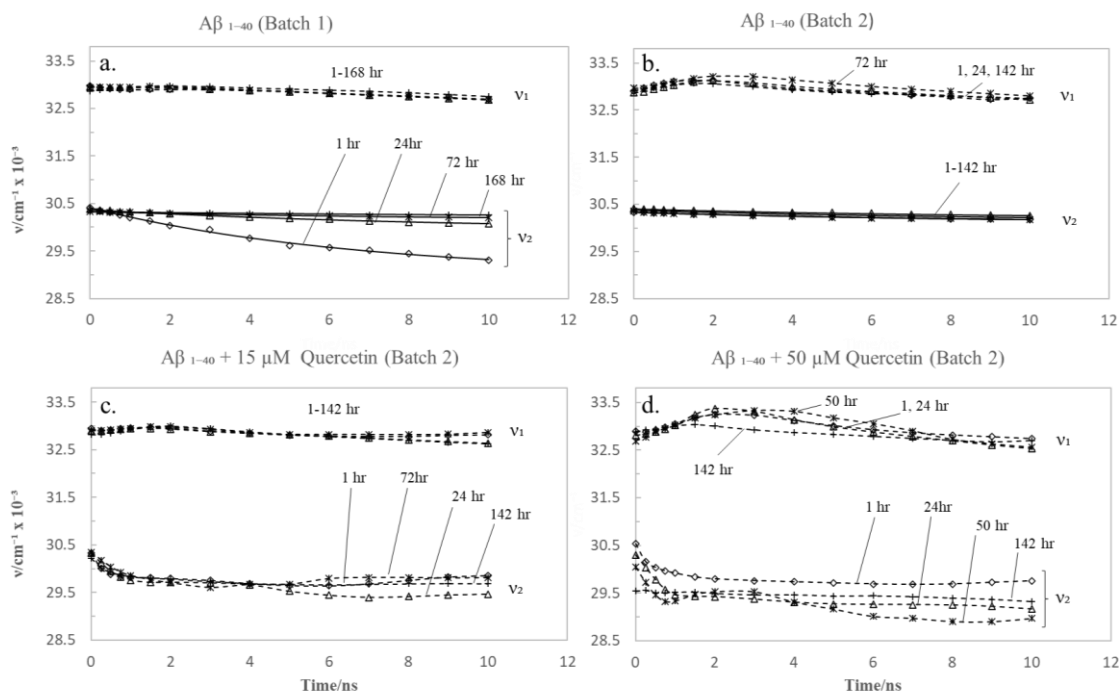


**Figure 37.** Peaks position  $v_1(t)$  and  $v_2(t)$ , obtained from fitting  $A\beta_{1-40}$  TRES to equation (49), plotted against time in nanoseconds at different stages of aggregation for sample with and without quercetin.

The position of the peak  $v_1(t)$  in the sample with preformed aggregates (Figure 37b) exhibits an initial shift towards higher wavenumbers followed by a shift towards lower wavenumbers. This shift towards higher wavenumbers is unusual in relaxation processes. This behaviour is also observed in the presence of quercetin (Figure 37c,d). One possible explanation for such behaviour is that the peak is representing, in addition to monomers, a contribution of very small oligomers, which have a slightly different fluorescence decay rate and are perhaps influenced by dielectric relaxation.

The position of the second peak  $v_2(t)$  is located at  $\sim 30500 \text{ cm}^{-1}$  at  $t=0$  for all  $A\beta_{1-40}$  samples. Plots show that changes in the position  $v_2(t)$  over 10 ns is highly influenced by

the presence of preformed  $A\beta_{1-40}$  aggregates and the concentration of quercetin, it is also influenced by the age of the sample. The position of  $\nu_2(t)$  1hr after sample preparation, in the  $A\beta_{1-40}$  sample free of preformed aggregates, shifts exponentially from  $\nu_2(0) \approx 30500 \text{ cm}^{-1}$  to  $\nu_2(\infty) \approx 29000 \text{ cm}^{-1}$  with the dielectric relaxation time  $\tau_R = 6.7 \text{ ns}$ . As the sample ages the relaxation time  $\tau_R$  increases and the shift towards the red is reduced, which is probably an indication of gradual growth in the size of the aggregates. The position  $\nu_2(t)$  in the sample containing preformed aggregates of  $A\beta_{1-40}$  (Figure 37b) exhibits a relatively small exponential shift with dielectric relaxation time  $\tau_R = 8.7$  after one hour of incubation. As seen in the previous sample the relaxation time  $\tau_R$  increases with time of incubation, which can be explained by gradual growth in the aggregates size. The initial state of this sample indicates that indeed it contains large preformed aggregates as its behaviour is similar to the sample from Figure 37a observed at later times.

Adding  $15 \mu\text{M}$  quercetin to the sample of  $A\beta_{1-40}$  with preformed large aggregates has significantly changed  $\nu_2(t)$  behaviour during the 10 ns after excitation.  $\nu_2(t)$  shifts rapidly towards lower wavenumbers. The shift is not exponential, thus cannot be attributed solely to dielectric relaxation. In addition,  $\nu_2(t)$  exhibits more or less the same behaviour after 24, 72 and 142 hr of incubation, which suggests that aggregates formed might have reached stability. Both of these facts are perhaps a result of quercetin forming a complex with  $A\beta_{1-40}$  aggregates, which leads to the rapid shift of the peak and prevents any further aggregation.

Increasing quercetin concentration to  $50 \mu\text{M}$  significantly impacts  $\nu_2(t)$  behaviour within 10 ns following excitation. 1 hr after excitation  $\nu_2(t)$  shifts rapidly but not exponentially towards lower wavenumbers. the rate and the extent of the shift is similar to that

observed in the 15  $\mu\text{M}$  quercetin sample. However,  $\nu_2(t)$  shifts become complex and sensitive to the time of incubation. This suggests that the module assuming two components is too simplified for  $\text{A}\beta_{1-40}$  in the presence of quercetin. There is possibly however that a variety of aggregates each exhibiting a distinct dielectric relaxation and fluorescence lifetime. Interestingly, after 142 hr of incubation the initial position of the peak  $\nu_2(0)$  appears at a substantially lower energy value  $\nu_2(0) \approx 29500 \text{ cm}^{-1}$  and remains constant over 10 ns after excitation. The initial position of the peak indicates that a different form of  $\text{A}\beta_{1-40}$  aggregates has been developed. The lack of shifts in the position  $\nu_2(t)$  suggest that the dielectric relaxation time of Tyr in this form of aggregate is too slow for detection or that the rotational freedom of Tyr has become limited.

The fluorescence intensity decay of each component is represented by the  $C_1(t)$  and  $C_2(t)$  functions obtained from fitting equation (49) to the experimental TRES data. The initial percentage contribution of fluorescence intensity of the two emitting species; monomers  $C_1(0)$  and oligomers  $C_2(0)$  are shown in figure 38 (b, e, h and k). After 1 hr of incubation, 98 % of fluorescence emission comes from monomers in the  $\text{A}\beta_{1-40}$  sample starting from monomers (Figure 38b), and as the sample ages the percentage contribution of monomers  $C_1(0)$  slightly decreases to about 95 % indicating that monomers are aggregating and forming larger structures. In the presence of preformed  $\text{A}\beta_{1-40}$  aggregates the percentage contribution of monomers to fluorescence emission is reduced to about 95% after 1h of incubation and continues to decrease with time of incubation until it reaches 86% of fluorescence emission after 72 hr. However, the percentage contribution of monomers increases after 142 hr to about 89 % due to the decrease in oligomers emission  $C_2(0)$ . The reduction observed in oligomers intensity could be a result of the decrease in the Tyr quantum yield as its peptide becomes involved in

forming larger oligomers. Therefore  $C_1(0)$  and  $C_2(0)$  cannot be associated directly with the concentration of monomers and oligomers in the sample.

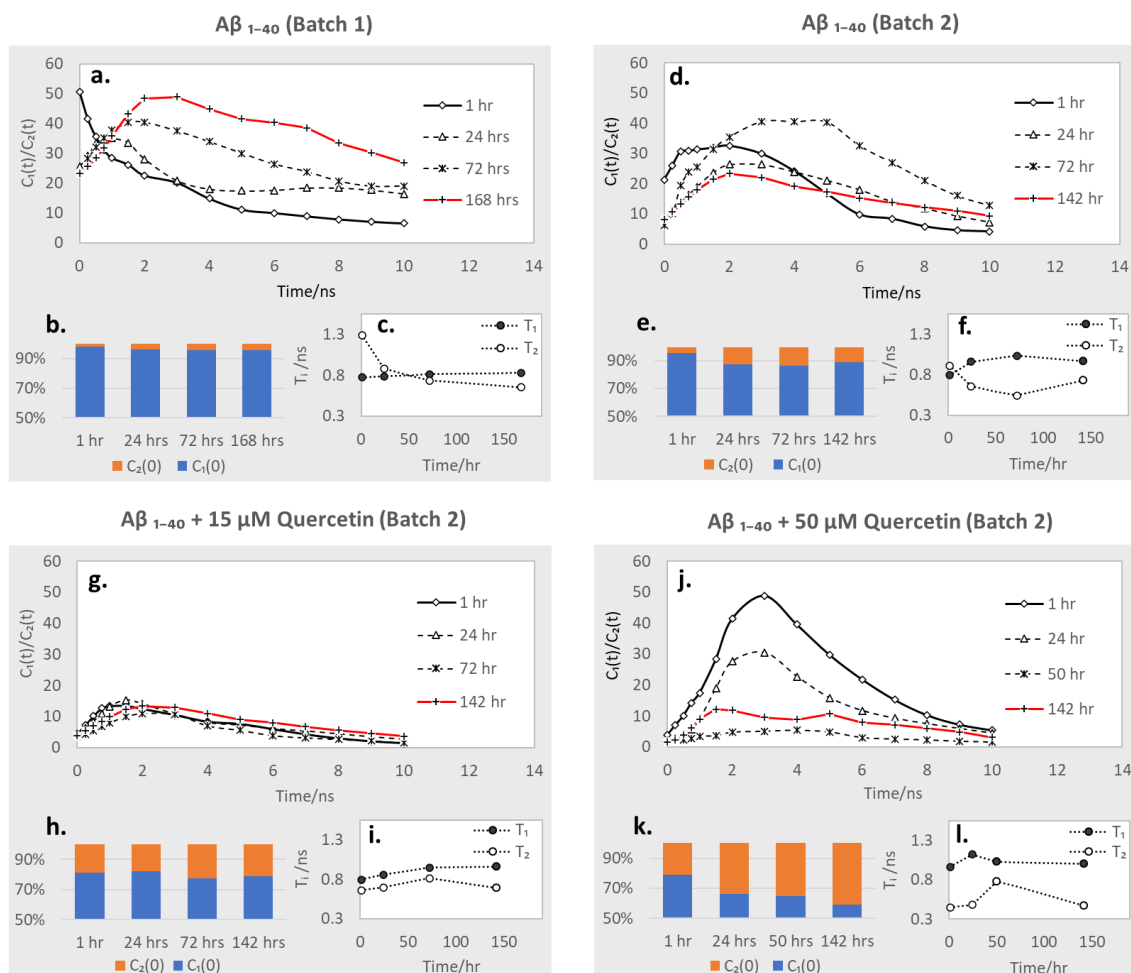


**Figure 38.** The initial percentage contribution of fluorescence intensity of the two-emitting species; monomers  $C_1(0)$  and oligomers  $C_2(0)$  attained from fitting equation (49) to the measured TRES of  $A\beta_{1-40}$  (batch 1) (b) and  $A\beta_{1-40}$  (batch 2) in the absence (e) and presence of two concentrations of quercetin 15  $\mu\text{M}$  (h) and 50  $\mu\text{M}$  (k). The ratio of monomer to oligomer contribution  $C_1(t)/C_2(t)$  of  $A\beta_{1-40}$  (batch 1) (a) and  $A\beta_{1-40}$  (batch 2) in the absence (d) and presence of quercetin 15  $\mu\text{M}$  (g) and 50  $\mu\text{M}$  (j). The characteristic fluorescence lifetimes of monomers  $T_1$  and oligomers  $T_2$  for  $A\beta_{1-40}$  (batch 1) (c) and  $A\beta_{1-40}$  (batch 2) in the absence (f) and presence of quercetin 15  $\mu\text{M}$  (i) and 50  $\mu\text{M}$  (l).

Adding 15  $\mu\text{M}$  to the  $A\beta_{1-40}$  sample containing preformed aggregates reduces the percentage contribution of monomers to about 80% after 1 hr of incubation (Figure 38h). No clear trend is observed after that in the percentage contribution of monomers  $C_1(0)$  and oligomers  $C_2(0)$  as the sample progresses. Increasing the quercetin concentration to 50  $\mu\text{M}$  demonstrates the same effect 15  $\mu\text{M}$  had on the percentage contribution of

monomers after 1 hr of incubation (Figure 38k). However, the contribution of monomers then significantly decreases to 60 % after 142 hr of incubation.

The  $C_1(t)/C_2(t)$  ratio for free  $A\beta_{1-40}$ , shown in figure (38a), is highly sensitive to the age of the sample and can be used to reveal the stage of  $A\beta_{1-40}$  aggregation. Figure (38d) shows the  $C_1(t)/C_2(t)$  ratio of the  $A\beta_{1-40}$  sample with preformed  $A\beta_{1-40}$  aggregates.

The shape of the curve, after 1 hr of incubation, indicates that aggregates are quite mature in comparison with the sample starting from monomers. In the presence of 15  $\mu\text{M}$  quercetin the  $C_1(t)/C_2(t)$  ratio is no longer sensitive to the stage of aggregation (Figure 38g), which is probably an indication of stability in the sample. Interestingly, adding 50  $\mu\text{M}$  highly influences the sensitivity of  $C_1(t)/C_2(t)$  (Figure 38j).

Previously we have demonstrated that in the  $A\beta_{1-40}$  sample, starting from mostly monomers,  $C_1(t)$  decays with a characteristic lifetime  $T_1 \approx 0.8$  ns regardless of the samples actual age (Figure 38c). This corresponds with the assumption that the  $C_1(t)$  component is mostly monomers. However, in the presence of preformed aggregates  $T_1$  increases with time of incubation from 0.8 to about 1 ns (Figure 38f). This is an indication that  $C_1(t)$  does not represent monomers only, which is also consistent with the unusual behaviour of  $v_1(t)$  indicated earlier. In the presence of 15  $\mu\text{M}$  quercetin,  $T_1$  gradually increases from about 0.8 ns to 1 ns (Figure 38i). When 50  $\mu\text{M}$  of quercetin is introduced to the sample  $T_1 \approx 1$  ns Initially and shows no significant changes over 142 hr (Figure 38l).

The characteristic lifetime  $T_2$  of the decay  $C_2(t)$ , which we associate with oligomers, decreases from 1.3 to 0.7 ns as the  $A\beta_{1-40}$  sample ages (Figure 38c). In the presence of preformed  $A\beta_{1-40}$  aggregates the initial value of  $T_2$  is reduced to about 0.9 ns and continues to decrease over time (Figure 38f). Adding quercetin to the  $A\beta_{1-40}$  sample

reduces the initial value of  $T_2$  to 0.7 and 0.5 ns at concentrations 15 and 50  $\mu\text{M}$  respectively (Figure 38i, l). the values of  $T_2$  then slightly increases as the samples age.

Parameters obtained from fitting equation (49) to data collectively suggest that aggregation progresses differently in the presence of quercetin due to the formation of  $\text{A}\beta$ -Quercetin complexes, which possibly prevent further  $\text{A}\beta$  aggregation. To further examine the nature of  $\text{A}\beta_{1-40}$  aggregates in the presence of quercetin, the aggregation process was monitored by the ThT binding assay in the absence and presence of 50  $\mu\text{M}$  quercetin (Figure 39). Results show that  $\text{A}\beta_{1-40}$  starts forming beta-sheet rich aggregates within  $\sim 21$  hr. A rapid elongation phase then begins and after 50 hours the saturation phase occurs. Adding quercetin slows down the nucleation process and significantly reduces the amount of amyloid fibrils. Thus, we conclude that quercetin alters the aggregation pathway leading to fibril formation.

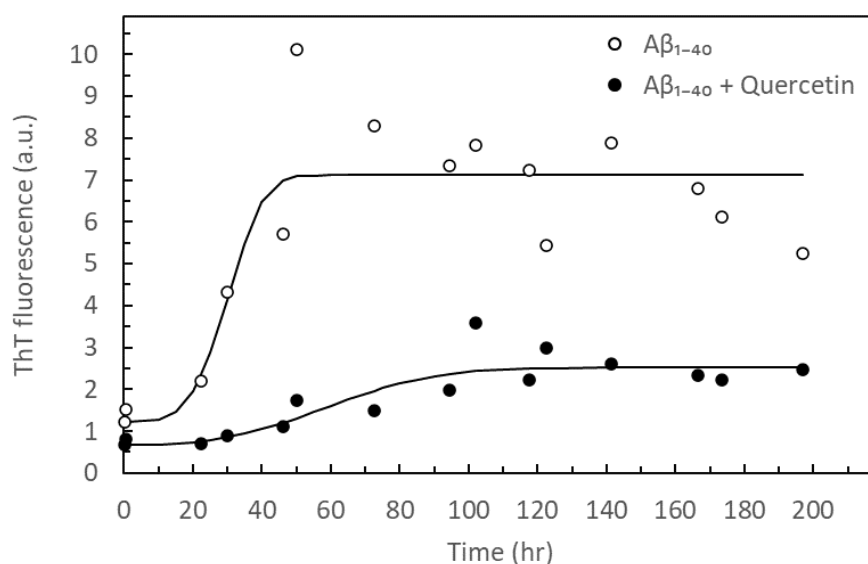


**Figure 39.** Time-dependent Th T fluorescence curves for 50  $\mu\text{M}$   $\text{A}\beta_{1-40}$  (batch 2) in the absence (○) and presence of 50  $\mu\text{M}$  Quercetin (●). The solid line is a guide to the eye.

### 9.3. Conclusion

TRES measurements show a clear difference between the two batches of A $\beta$ <sub>1-40</sub>. We attribute this difference to the presence of pre-formed aggregates in the second batch. This has been confirmed by nanoparticle tracking analysis (NTA) in section 11.3. The presence of such aggregates affects the lag time for fibril formation. It may also have an impact on quercetin's ability to alter the aggregation pathway.

Fitting the model, which assumes two fluorescent components (equation 49, N=2) to TRES data suggests that the actual kinetics of A $\beta$ <sub>1-40</sub> in the presence of quercetin is in fact more complex. Possibly due to the interactions between A $\beta$ <sub>1-40</sub> aggregates and Quercetin, and the existence of more than two fluorescent species. The shifts observed in the position of both peaks  $v_1(t)$  and  $v_2(t)$  indicate the existence of numerous fluorescent species. More interestingly, the fluorescence intensity percentage contribution of oligomers  $C_2(0)$  at  $t=0$  increases with quercetin concentration. At a molar ratio of 1:1 (A $\beta$ <sub>1-40</sub> : Quercetin) the percentage contribution of oligomers  $C_2(0)$  continues to increase with time of incubation, which suggests an increase in the number of small oligomers. Moreover,  $C_2(0)$  does not exhibit the usual reduction observed in the free A $\beta$ <sub>1-40</sub> sample at late stages of aggregation, which suggests that small aggregates are growing in number rather than size. This assumption was confirmed by the ThT binding assay. Thus, quercetin experiments clearly show early formation of the A $\beta$ -Quercetin complexes, which seem to inhibit further A $\beta$  aggregation. This fact, combined with quercetin being a natural non-toxic substance capable of crossing the blood-brain barrier, makes it a potential nutrient helping to prevent the development of Alzheimer's disease.

Nonetheless, a more complex model is required to fit the data efficiently. but given the number of experimental points obtained for TRES, the results of fitting data to a more complex model cannot be statistically significant.

## 10. Fluorescence anisotropy: a method for early detection of beta-amyloid aggregation

### 10.1. Introduction

Time-resolved fluorescence anisotropy measurements are widely used to study the dynamics of the various processes that can lead to the depolarisation of fluorescence emission following excitation with polarised light<sup>189</sup>. The most common reasons for depolarisation include the energy transfer from a donor to an acceptor with a different orientation or the molecular rotation caused by the Brownian motion. Molecular motion is naturally affected by the size of the molecule and some local environmental factors, such as viscosity and molecular confinement. Therefore, fluorescence anisotropy can be efficiently used as a tool to obtain information about molecular size and mobility. A number of studies have reported that the fluorescence anisotropy technique can be utilized efficiently to monitor protein conformational changes<sup>190</sup>, protein-protein interaction<sup>191</sup> and protein aggregation<sup>192–194</sup> based on the accompanying changes in anisotropy.

Fluorescence anisotropy measurements have been used to study the aggregation of the A $\beta$ <sub>1-40</sub> peptide<sup>195,196</sup>. Most A $\beta$ <sub>1-40</sub> anisotropy measurements involve the use of extrinsic probes, which, however, may alter the aggregation pathway<sup>197</sup>. Here we probe the suitability of using intrinsic Tyr fluorescence anisotropy to avoid perturbing the native structure of the A $\beta$ <sub>1-40</sub> peptide with extrinsic probes. Anisotropy responses of free A $\beta$ <sub>1-40</sub> were compared with those obtained for A $\beta$ <sub>1-40</sub> in the presence of quercetin and glucose.

## 10.2. Results and discussion

Intensity decays  $I_{VV}(t)$  and  $I_{VH}(t)$  were obtained using the TCSPC method (as described in section 4.4) at excitation wavelength 279 nm and detection wavelength 315 nm. Decays were analyzed by separate analysis of the sum  $S(t)$  and difference  $D(t)$  decays (equations 44 and 45). Figure (40) shows the decay parameters obtained from fitting  $S(t)$  to a 4-exponential model. The large number of counts present in  $S(t)$  makes it difficult to fit, thus the  $\chi^2$  values are larger than usual. fluorescence decay times  $\tau_1$ ,  $\tau_2$ ,  $\tau_3$  and  $\tau_4$  in free  $A\beta_{1-40}$  are shown in figure (40a). the changes observed in the decay times with time of incubation are in agreement with previous fluorescence intensity decay measurements obtained for  $A\beta_{1-40}$ .  $\tau_1$ ,  $\tau_2$  and  $\tau_3$  are more or less constant during the time of aggregation while  $\tau_4$  exhibits a substantial decrease from about 10 ns to 4 ns within 72 hr. The change observed in the value of  $\tau_4$  is greatly influenced by the presence of preformed  $A\beta_{1-40}$  aggregates (seeds). The existence of such aggregates accelerates the decrease in the value of  $\tau_4$ . The percentage contributions of the decay components  $f_1$ ,  $f_2$ ,  $f_3$  and  $f_4$  are especially sensitive to the early stages of aggregation (Figure 40b). During the first 72 hr the percentage contribution of the long-lived components  $f_3$  and  $f_4$  increase while  $f_2$  decreases, then they remain constant for the rest of the time.

In the presence of 50  $\mu$ M of quercetin the decay times are almost identical to those obtained for the free  $A\beta_{1-40}$  sample after around 72 hrs (Figure 40c). the decay times slightly decrease after 22 hrs and remain constant afterwards. The initial values of the decay times are perhaps a consequence of quercetin attachment to  $A\beta_{1-40}$  structures. The percentage contribution of the decay components clearly indicates a different form of  $A\beta_{1-40}$  aggregates in the presence of quercetin (Figure 40d).

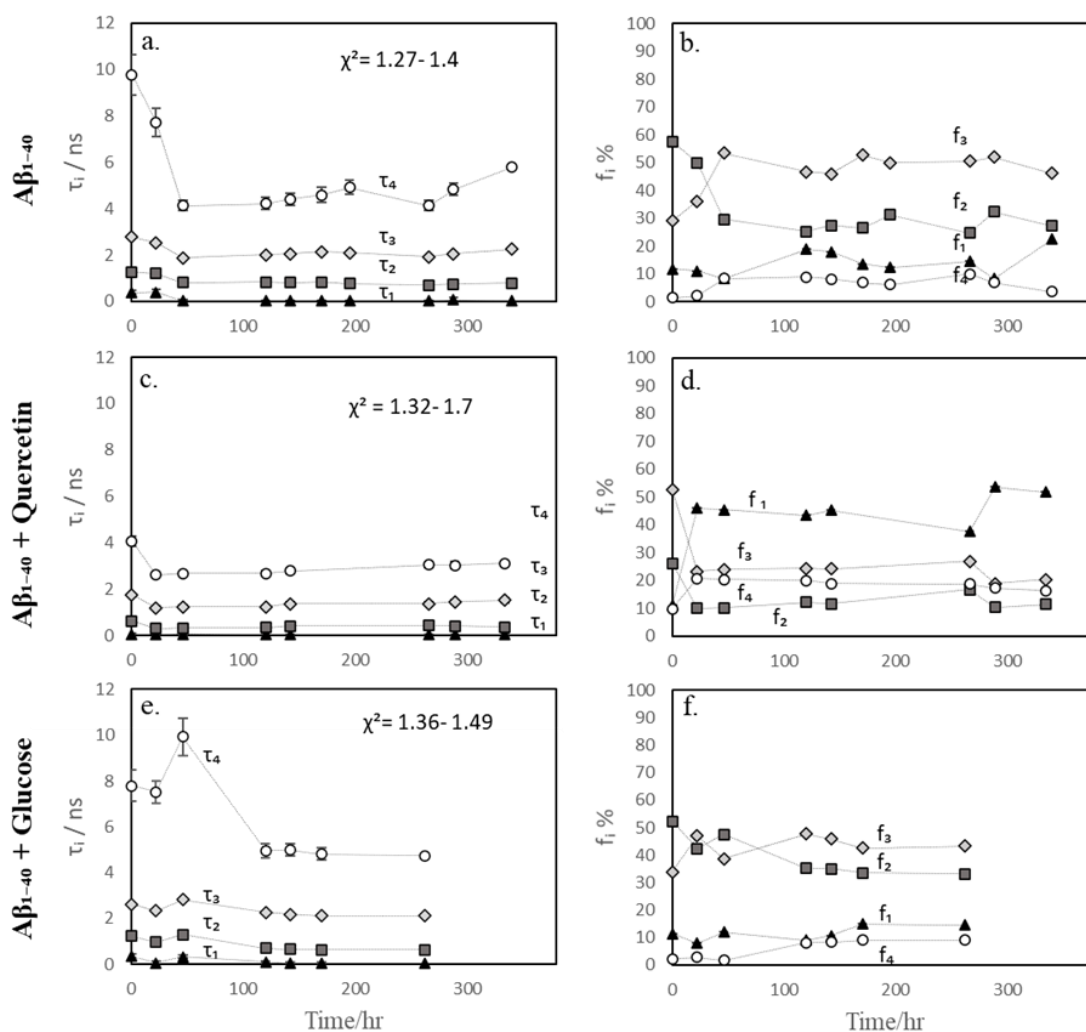


**Figure 40.** Parameters obtained from fitting a four-exponential decay model to the total fluorescence decay ( $I_{VV} + 2G I_{VH}$ ) of Tyr in a 50  $\mu\text{M}$   $\text{A}\beta_{1-40}$  solution obtained at different moments in time: Tyr fluorescence decay times  $\tau_1$ ,  $\tau_2$ ,  $\tau_3$  and  $\tau_4$  in free  $\text{A}\beta_{1-40}$  (a), in the presence of 50  $\mu\text{M}$  Quercetin (c) and 50 mM Glucose (e), percentage contributions of the decay components  $f_1$ ,  $f_2$ ,  $f_3$  and  $f_4$  in free  $\text{A}\beta_{1-40}$  (b), in the presence of Quercetin (d) and Glucose (f). Error bars represent  $3\times$  the standard deviation.

In the presence of 50 mM glucose, the initial values of the decay times  $\tau_1$ ,  $\tau_2$  and  $\tau_3$  are similar to those obtained for free  $\text{A}\beta_{1-40}$  and they remain constant during the time of experiment (Figure 40e).  $\tau_4$  decays from about 8 ns to 4 ns within 120 hrs and remains constant afterwards. The Percentage contribution of the decay components also exhibit a similar behavior to that observed in the free  $\text{A}\beta_{1-40}$  sample (Figure 40f).

The parameters recovered from the sum analysis are held constant during the analysis of  $D(t)$  as described in section 4.4. Two rotational correlation times  $\tau_{C1}$  and  $\tau_{C2}$  are recovered from fitting the difference data of  $A\beta_{1-40}$  in the absence (Figure 41a) and presence of quercetin (Figure 41d) and glucose (Figure 41g). In a freshly prepared sample of  $A\beta_{1-40}$ , the first rotational correlation time  $\tau_{C1}$  is equal to  $0.67 \pm 0.05$  ns, whereas the second rotational correlation time ( $\tau_{C2} < 0.027$  ns) is too fast to be measured accurately using the TCSPC instrument. As the sample ages,  $\tau_{C1}$  gradually increases to  $1.90 \pm 0.76$  ns within 195 hrs. The value of  $\tau_{C2}$  remains  $< 0.05$  ns for 172 hrs then suddenly increases to  $0.47 \pm 0.12$  ns at  $t=195$  hr. Both  $\tau_{C1}$  and  $\tau_{C2}$  reach their maximum at  $t=195$  hr and start to decrease afterwards. The increase in the value of the rotational correlation time is typically an indication of an increase in the size of the particle, however,  $A\beta_{1-40}$  aggregates are more elliptical than spherical, thus the precise size of the aggregates cannot be determined using equation 29. The elliptical shape, however, provides a reasonable explanation for the existence of two rotational correlation times, since the elliptical particle takes more time to rotate around its minor-axis,  $\tau_{C1}$ , than to rotate around its major axis,  $\tau_{C2}$ . Based on this assumption we can say that the size of the major axis is much more affected with aggregation than the minor axis. The unexpected decrease in the value of  $\tau_{C1}$  and  $\tau_{C2}$  after  $\sim 200$  hr is perhaps due to the decreased fluorescence quantum yield induced by aggregation. Thus, when aggregates grow to a certain size they can no longer be observed because of their weak emission and only small aggregates are detected. This is supported by the usual drop in fluorescence total intensity with time of sample incubation.

The fractional contributions  $b_1$  and  $b_2$  of the rotational correlation times  $\tau_{C1}$  and  $\tau_{C2}$  respectively are more or less constant during aggregation with an exception at times 0.25, 22 and 288 hr (Figure 41b). At these particular moments  $d_2$  is exceptionally high

and  $r_0$  is larger than 0.4 (Figure 41c). In general, if the measured anisotropy exceeds 0.4 in a randomly oriented sample, one can confidently infer the presence of scattered light in addition to fluorescence<sup>112</sup>.

In the presence of quercetin,  $\tau_{C1}$  almost immediately increases from  $0.67 \pm 0.095$  ns to about 1.3 ns and remains constant for the rest of the time of experiment (Figure 41d). The sudden increase is probably a result of quercetin binding to  $A\beta_{1-40}$  aggregates. Apparently, this form of binding stabilizes the size of  $A\beta_{1-40}$  aggregates to some extent. In the presence of Glucose  $\tau_{C1}$  gradually increases from  $0.73 \pm 0.06$  ns to  $2.3 \pm 0.67$  ns, which indicates that the size of the aggregates is growing (Figure 41g).

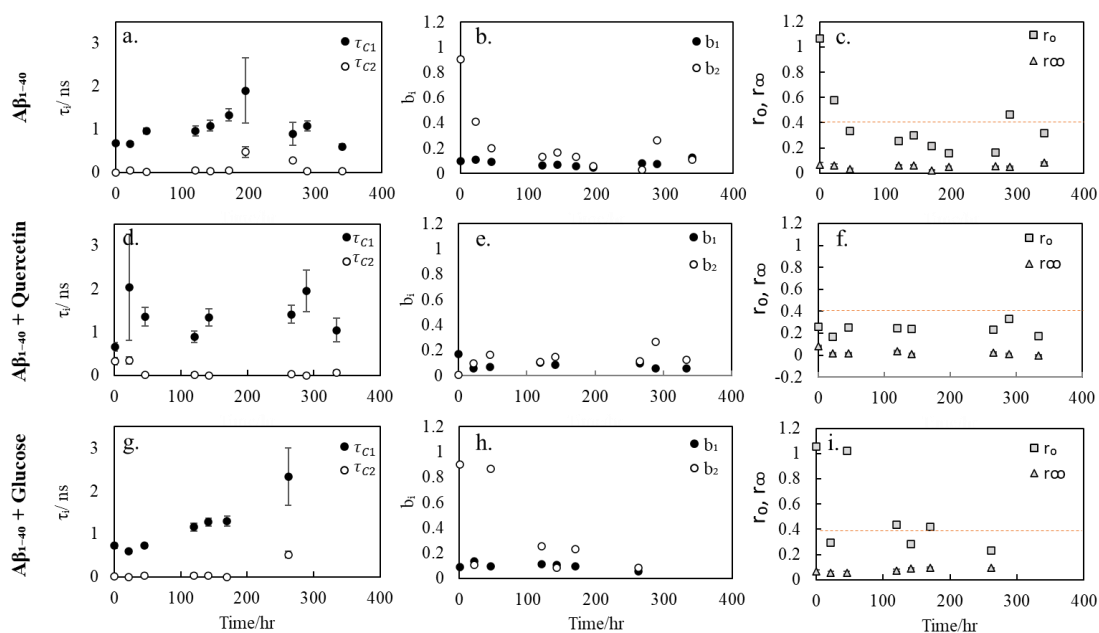


**Figure 41.** Parameters obtained from fitting experimental data of  $50 \mu\text{M } A\beta_{1-40}$  in HEPES buffer (pH 7.4) to equation (47) as aggregation proceeds: the rotational correlation times  $\tau_{C1}$  and  $\tau_{C2}$  in free  $A\beta_{1-40}$  (a), in the presence of  $50 \mu\text{M}$  Quercetin (d) and  $50 \text{ mM}$  Glucose (g); the fractional contributions  $b_1$  and  $b_2$  of the rotational correlation times  $\tau_{C1}$  and  $\tau_{C2}$  respectively in free  $A\beta_{1-40}$  (b), in the presence of  $50 \mu\text{M}$  Quercetin (e) and  $50 \text{ mM}$  Glucose (h);  $r_0$  (square) and  $r_\infty$  (triangles) in free  $A\beta_{1-40}$  (c), in the presence of  $50 \mu\text{M}$  Quercetin (f) and  $50 \text{ mM}$  Glucose (i). Error bars represent the standard deviation.

$\tau_{C2}$ , which we associate with the rotation around the aggregate's major-axis, is fairly constant during the first 170 hr of incubation at about 0.02 ns.  $\tau_{C2}$  then increases to

$0.52 \pm 0.08$  ns at  $t = 262$  hr. Beyond 262 hours, measurements could not be carried out due to the weak fluorescence signal. The fractional contributions  $b_1$  and  $b_2$  are equal and constant at  $\sim 0.1$  during aggregation with exceptions at 0.25, 46, 120 and 170 hr where  $b_2$  is substantially higher (Figure 41h). The value of  $r_0$  at these particular moments in time is  $> 0.4$ , suggesting that light scatter is the cause of that increase (Figure 41i). The residual anisotropy  $r_\infty$  exhibits a slight increase from about 0.06 to 0.095 (Figure 41i). This implies that the rotational motion of Tyr has become more restricted over time.

### 10.3. Conclusion

Anisotropy measurements using the intrinsic Tyr allow detection of small  $A\beta_{1-40}$  aggregates. As aggregates grow in size their quantum yields are reduced and they become untraceable. Because there is usually high level of scattered light in this type of experiments, care should be taken when processing data.

$A\beta_{1-40}$  anisotropy decays appear to be sensitive to quercetin interactions with  $A\beta_{1-40}$ . The quercetin- $A\beta_{1-40}$  aggregates reach their maximum size within 22 hr and then stop developing. Since these particles are stable, they most likely will not contribute to fibril formation. This is in agreement with studies reporting quercetin's inhibitory effect on amyloid fibril formation<sup>181</sup>.

The presence of glucose had no significant effect on the anisotropy measurement. The initial size of aggregates and the subsequent gradual growth with time of incubation is almost identical to that observed for free  $A\beta_{1-40}$ . This is probably because the glycation processes typically take few weeks. Unfortunately the reduction in fluorescence intensity does not allow measurements after  $\sim 260$  hr. Thus, glycation effects cannot be monitored using this technique.

## 11. Nanoparticle tracking analysis (NTA) for the detection of beta-amyloid aggregates

Nanoparticle Tracking Analysis is one of the few techniques that allows for visualizing and analysing of nanoparticles in suspension based on the rate of the Brownian motion, which is related to the particle size. The optical configuration employed in this technique enables simultaneous tracking and analysis of particles on an individual basis, which makes it ideal for real-time analysis of polydisperse systems such as protein aggregates. NTA operates for nanoparticles in the range of 10 to 1000 nm, depending on the type of the particle. Therefore, it is not possible to trace the early stages of oligomerization using NTA, but rather aggregates that appear in the later stages of the aggregation process. Here we are looking to see whether there is any correlation between the information on A $\beta$ <sub>1-40</sub> aggregation recovered from the molecular-level fluorescence technique and the method based on the analysis of Brownian motion.

### 11.1. Physical principle underlying NTA

**Brownian motion and diffusion:** Brownian motion is the random motion of particles suspended in a medium (liquid or gas), caused by the random molecular bombardment of tiny particles by the liquid/gas molecules. It was named after the botanist Robert Brown, who first observed this phenomenon in 1827<sup>198</sup>. The statistical laws explaining the Brownian motion were derived afterward by Einstein in 1905<sup>199-201</sup>. They relate the translational diffusion coefficient,  $D_t$ , or rotational diffusion coefficient,  $D_r$ , to the friction experienced by the particle and the heat bath  $k_B T$  ( $k_B$  is the Boltzmann constant and  $T$  is the absolute temperature), by:

$$D_t = \frac{K_B T}{f_t} = \frac{K_B T}{6\pi\eta R} \quad 51$$

$$D_r = \frac{K_B T}{f_r} = \frac{K_B T}{8\pi\eta R^3} \quad 52$$

Where  $f_t = 6\pi\eta R$  and  $f_r = 8\pi\eta R^3$  are the Stokes' hydrodynamic expressions for the translational and rotational friction of a spherical particle of radius  $R$  in a solvent of viscosity  $\eta$ .

The mean square displacement (MSD) travelled by a particle in a given time interval,  $t$ , is related to the diffusion coefficient,  $D$ , by an expression that depends primarily on the number of dimensions as follows<sup>202</sup>:

$$\langle x^2 \rangle = 2Dt \quad 53$$

$$\overline{\langle x, y \rangle^2} = 4Dt \quad 54$$

$$\overline{\langle x, y, z \rangle^2} = 6Dt \quad 55$$

measuring the diffusion coefficient and using it to derive the size of the particle is commonly used in Light scattering methods for particle size analysis such as Nanoparticle tracking analysis (NTA) and dynamic light scattering (DLS).

## 11.2. The Nanoparticle Tracking Analysis technique

The NTA system (Nanosight LM10) makes practical use of the properties of both light scattering and Brownian motion so as to obtain the size distribution of nanoparticles in liquid suspension. It works by passing a laser beam (405 nm) through the sample chamber and monitoring the image generated by the scattered light from the particles by

means of a 20x magnification microscope onto which is mounted a light sensitive CCD camera (Figure 42b). The camera records a video file of the motion of the particles in the field of view (approximately  $100\ \mu\text{m} \times 80\ \mu\text{m} \times 10\ \mu\text{m}$ ) at roughly 30 frames per second. A Nanosight NTA 3.0 software is then used to analyse the recorded data. The software tracks the particles frame by frame in two dimensions (Figure 42a) and uses the registered path of each particle to calculate the MSD, which is connected to the diffusion coefficient and the hydrodynamic radius by equations ( 51 and 54 ). Thus, one can determine simultaneously the size distribution of the sample and concentration.

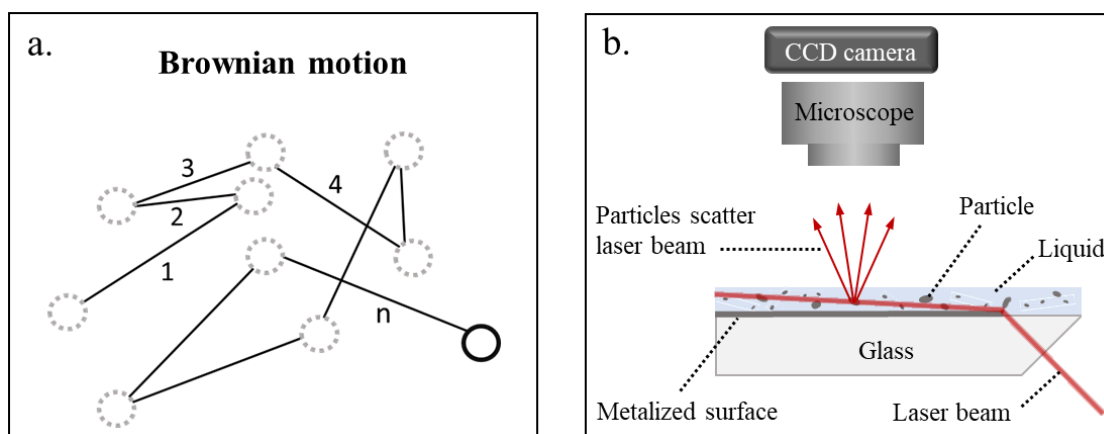


**Figure 42.** Graphical representation of a Particle undergoing Brownian motion in two dimensions (a). Schematic of the optical configuration used in NTA (b).

Before taking NTA measurements one must optimize the image first. This includes setting up the camera level, which is crucial to attaining valid results. The camera level must be increased until the image of all existing particles is visualised, but no more than 20% are saturated. Another important measure is the concentration of the sample. The NanoSight instrument can only work with particle concentrations ranging from about  $10^7$  to  $10^9$  particles/ml, which is roughly 20-100 particles in the field of view. At concentrations  $> 10^9$  particles/ml the field of view becomes crowded and particles cross over. In such conditions, the tracking software cannot distinguish which is which and

therefore stops tracking both to avoid false tracking. Because the incidence of particle crossover is very high at concentrations  $> 10^9$ , there is insufficient time to determine the diffusion coefficient and consequently size. At concentrations below  $10^7$  particles/ml the number of particles in the field of view becomes very low, thus the number of particles that can be analysed during the typical analysis time of 30-60 seconds is very small, which leads to errors of a statistical nature. Once the proper settings are found a number of 60-seconds video captures are recorded. Processing the data requires setting the detection threshold, which governs the minimum brightness of pixels to be considered for tracking. Lowering the detection threshold ensures that small particles are included. However, if it is too low, noise might be tracked.

NTA currently operates for particle size from about 10 to 1000 nm in diameter, depending on the physical nature and properties of the investigated particles. the lower size limit of this method is primarily dependent upon the amount of light scattered by the particles. This value in turn is influenced by the size and shape of the particle, the contrast between the refractive index of the particles and that of the solution, the illumination power and wavelength. The scattering of light by particles smaller than the wavelength of the light is called Rayleigh scattering and can be described by the formula<sup>203</sup>:

$$\frac{I}{I_{in}} = \frac{16 \pi^4 R^6}{d^2 \lambda^4} \left( \frac{n^2 - 1}{n^2 + 2} \right) \sin^2 \psi \quad 56$$

Where  $I$  is the scattered power per unit area,  $I_{in}$  is the incident power per unit area,  $R$  is the particle radius,  $d$  is the distance from the scattering object,  $\lambda$  is the wavelength of light,  $n$  is the relative refractive index and  $\psi$  is the angle between input polarization and scattering direction.

Hence the total light scattered ( $P_{scat}$ ) into an aperture of collection angle  $\Theta$  (i.e. Numerical aperture =  $\sin\Theta$ ) would be:

$$P_{scat} = \frac{64 \pi^4 R^6}{\lambda^4} \left( \frac{n^2 - 1}{n^2 + 2} \right) \eta_0 I_{in} \quad 57$$

Where  $\eta_0 = \frac{1 - \cos \theta}{4} + \frac{1 - \cos^3 \theta}{12}$

The NTA system has a fixed aperture and detection angle as well as a fixed laser wavelength and power, thus the lower limit of detection depends primarily on the particle size and the refractive index of the particles. As a consequence, particles with a high refractive index, such as gold and silver can be readily analysed down to 10 nm in diameter<sup>204,205</sup>, whereas particles with lower refractive index, such as protein particles are difficult to detect at such sizes<sup>206</sup>.

The upper size limit of the NTA technique is constrained by the limited Brownian motion of large particles. Particles larger than 1000 nm in diameter move very slowly and therefore the precision of the analysis starts to diminish. The viscosity of the solvent also plays a part in defining the upper size limit of the system as it too effects the particles movement.

### 11.3. Detection of beta-amyloid aggregates by NTA

#### 11.3.1. Introduction

Considering the extent to which amyloid fibril formation is related to neurodegenerative diseases, many researchers have put much effort in developing kinetic models that can explain the mechanism of amyloid fibril formation<sup>207–209</sup>. However, mechanistic-based kinetic models can be reliably determined only if both the size distribution and concentration of the aggregates are obtained<sup>210</sup>. Ideally

experimental methods should be non-destructive, non-invasive, label-free and flexible to a variety of solution conditions. ThT fluorescence is one of the most common methods used to detect amyloid fibril formation. It provides information on the relative mass concentration of fibrillar aggregates but cannot determine the size or number concentration of fibrils. Microscopic techniques such as atomic force microscopy, AFM, and transmission electron microscopy, TEM, provide valuable and detailed information about the dimensions and morphological characteristics of aggregates<sup>10-12</sup>. Yet quantitation of the total population of aggregates is challenging. Another method commonly used is dynamic light scattering (DLS), which is a rapid, user-friendly and non-invasive technique. Nevertheless, DLS cannot provide the number concentration of particles, and only averaged properties can be determined. Moreover, DLS measurements of polydisperse samples are usually biased towards larger particles within the sample<sup>211</sup>.

NTA is another light scattering technique. it was first mentioned in 2006 as a commercial set-up that has the unique ability to track individual particles, so that one can obtain both a size distribution as well as a number concentration, and not just a mean size<sup>206,212</sup>. Since then, NTA has been utilized in many applications in different research and industry fields.<sup>213-217</sup> It is challenging, however, to measure small particles by NTA; the minimum size limit depends on the refractive index of the sample. proteins for example cannot be detected at sizes smaller than 60 nm in diameter<sup>218</sup>.

Determining the size and size distribution of A $\beta$ <sub>1-40</sub> aggregates accurately is not trivial, as protein aggregates are usually very heterogeneous, with sizes ranging from a few nanometers to several micro-meters<sup>219</sup>. The NTA technique is shown to be a useful

complementary technique to visualize and measure the size of aggregates in the range 50 -1000 nm. Therefore, NTA measurements were carried out for A $\beta$ <sub>1-40</sub> samples in the presence and absence of Quercetin.

### 11.3.2. Results and discussion

Polystyrene or latex beads are commonly used as calibration standards for size measurements. Therefore, standard polystyrene beads of 50 nm, 100 nm and 400 nm in diameter were prepared (see section 5.6.) and analysed using the NanoSight system. The instrument could not detect the 50 nm beads. The 100 nm beads were visible as shown in Figure (43a).

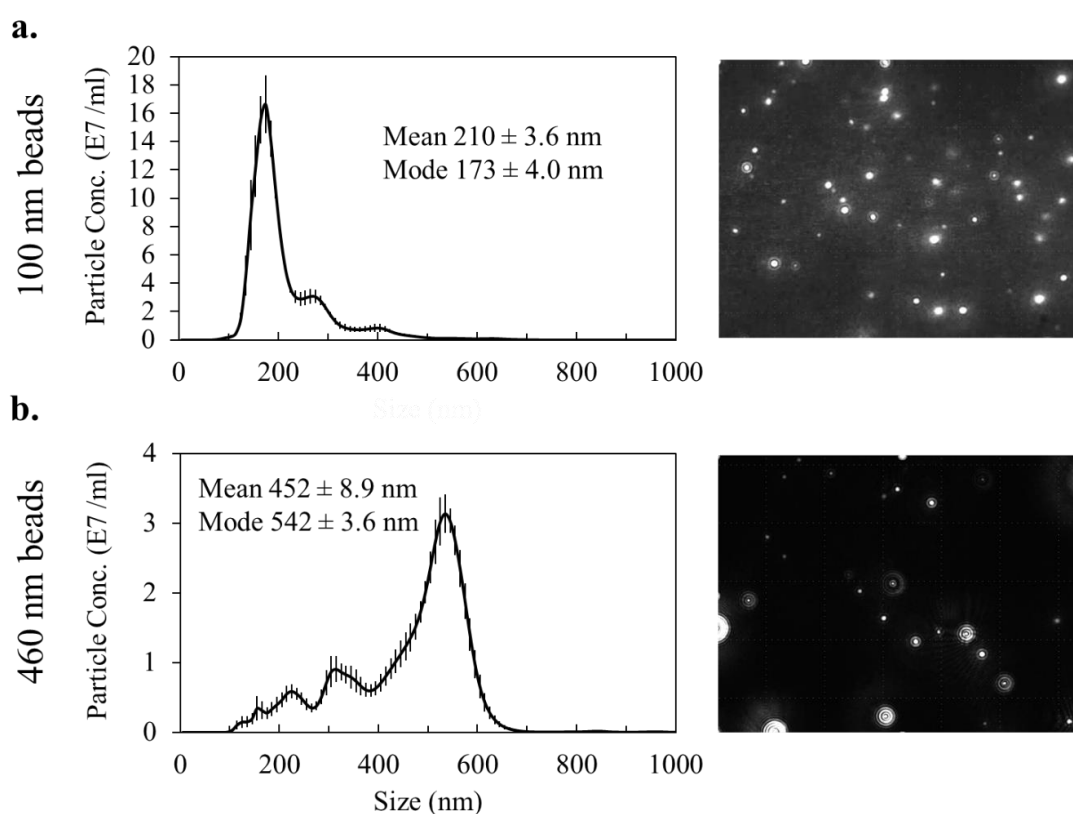


**Figure 43.** Size distribution from NTA measurements of monodisperse polystyrene beads, with the corresponding NTA video frame. a) 100 nm beads; b) 460 nm beads. Error bars represent standard errors obtained from ten measurements of the same sample

However, the mean size obtained was  $210 \pm 3.6$  nm. Such error is expected knowing that the intensity of light scattered by the 50 nm beads is not detectable and that intensity of scattered light scales with the particle diameter to the sixth power (equation 57). The size distribution of the 100 nm beads (Figure 43a) suggests that particles  $< 100$  nm cannot be detected with this instrument. Figure (43b) shows the particle size distribution of the 460 nm beads. The mean diameter obtained from that distribution was  $452 \pm 8.9$  nm, which is close to the expected value.

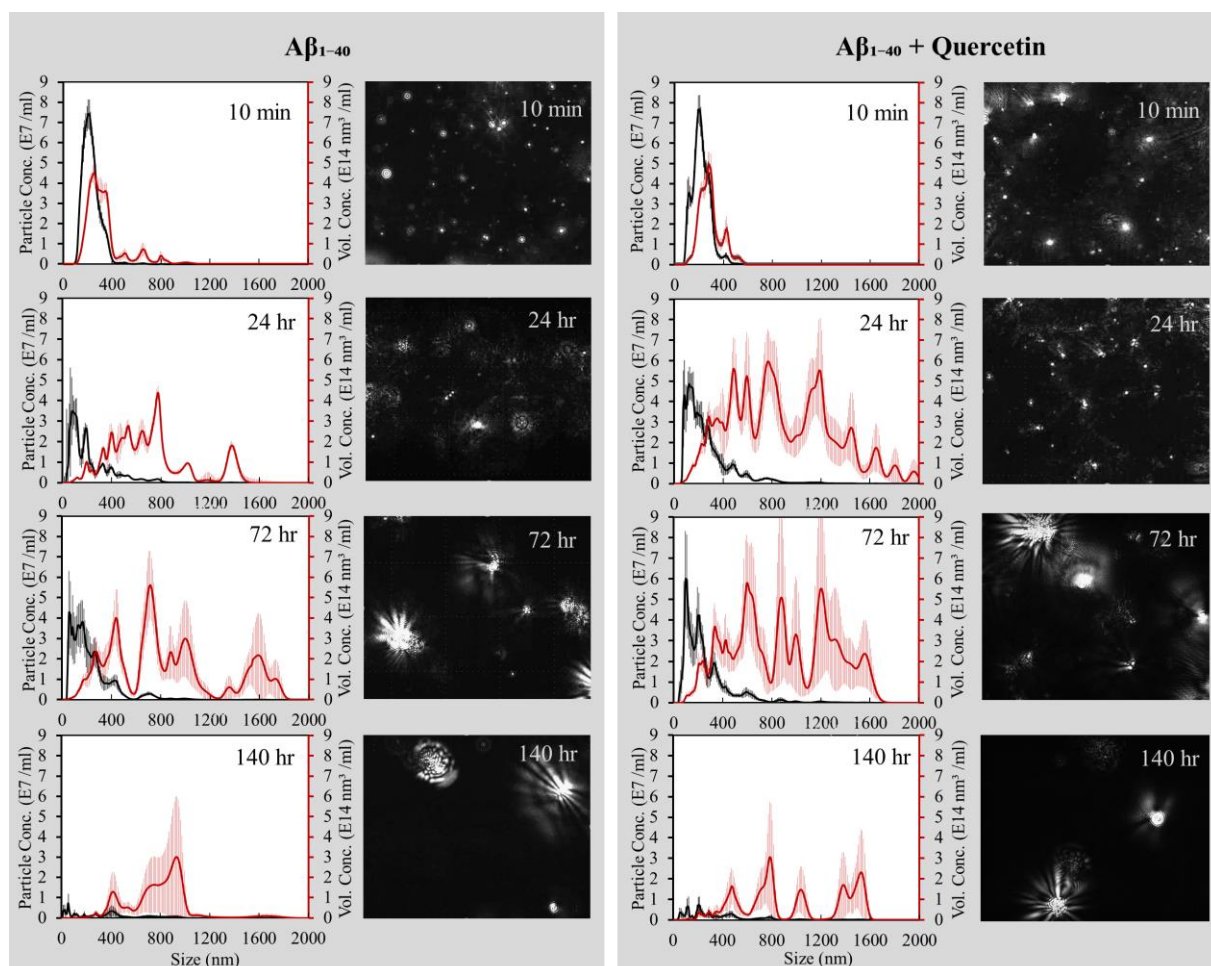


**Figure 44.** Nano tracking analysis (NTA) showing Size distribution of A $\beta$ 1-40 aggregates in the absence (left) and presence of quercetin (right) measured after 10 min, 24 hr, 72 hr and 140 hr of incubation in terms of number concentration (black line) and volume concentration (red line), with accompanying NTA video screen shots. Error bars represent standard errors obtained from ten measurements of the same sample.

NTA measurements were obtained for samples of A $\beta$ <sub>1-40</sub> ( 50  $\mu$ M ) incubated in HEPES buffer (pH 7.4) with and without Quercetin (15  $\mu$ M) at 37°C. Before measurement, A $\beta$ <sub>1-40</sub> samples were diluted to 25  $\mu$ M and were allowed about 30 min to thermally stabilize at 20 °C. Figure (44) shows the Size distribution of A $\beta$ <sub>1-40</sub> aggregates in the absence and presence of quercetin measured after 10 min, 24 hr, 72 hr and 140 hr of incubation, with accompanying NTA video screen shots. The size distribution of A $\beta$ <sub>1-40</sub> aggregates, produced by the NanoSight NTA 3.0 software, is expressed in terms of particle number concentration (black). results were then transformed from number concentration to volume concentration (red). This is important because the presence of even a low number of large aggregates can represent a significant proportion of the total A $\beta$ <sub>1-40</sub> peptides in the sample.

The number-weighted distribution of A $\beta$ <sub>1-40</sub> measured after 10 min from sample preparation exhibits a peak at around 200 nm. This confirms the existence of pre-formed aggregates in the prepared sample. Nearly the same distribution is observed in the presence of Quercetin.

Measurements obtained after 24 hr of incubation show a slight difference between samples in the absence and presence of Quercetin. The recorded images show that the size of aggregates is larger in the absence of quercetin. The number-weighted distribution of A $\beta$ <sub>1-40</sub> in the absence of quercetin shows a decrease in the number of small particles (100-300 nm) offset by the appearance of a small number of large particles (400-800 nm). The volume-weighted distribution has become wider and has shifted towards larger sizes. Which means that the number of peptides involved in the formation of large aggregates far exceeds those involved in the formation of smaller ones. The same behaviour is observed in the presence of quercetin, although there is

a significant difference in the number of particles. This may be due to aggregates growing at a faster rate in the absence of quercetin. When aggregates grow to a certain size, they lose their spherical shape and the software can no longer find the aggregate's centre to track it. Therefore, such aggregates are usually not included in the analysis.

The images recorded after 72 hr of incubation clearly show that aggregates are growing in size in both samples although the number/volume distribution does not reflect that. This confirms that aggregates above a certain size cannot be detected by this method. After 140 hr of incubation aggregates are too large for detection in both samples.

### **11.3.3. Conclusion**

The NTA technique as used in this study allows one to visualise and measure monodispersed particles in the size range ~ 100-1000 nm. However, highly polydisperse samples such as  $A\beta_{1-40}$  aggregates are challenging and the choice of parameter settings (e.g. camera level or detection threshold) can influence the result significantly. Thus, measurements should be acquired in uniform conditions by an experienced and skilled user.

NTA measurements obtained for  $A\beta_{1-40}$  samples in the absence and presence of quercetin suggest that the samples contain pre-formed aggregates. The volume-weighted distribution clearly shows an increase in the size of  $A\beta_{1-40}$  aggregates. In the presence of 15  $\mu\text{M}$  quercetin, the rate of the aggregation process is slightly reduced. Higher concentrations of quercetin might have a stronger effect on aggregation and should be investigated. In addition, the presence of pre-formed  $A\beta_{1-40}$  aggregates in the sample may prevent us from knowing the true impact quercetin has

over the aggregation process. Therefore, repeating the experiment with an  $A\beta_{1-40}$  sample free of pre-formed aggregates is of great importance.

Another challenge one faces when using this technique to analyse  $A\beta_{1-40}$  aggregates is related to tracking large particles that usually have no clear centre. Such particles are not included in the analysis. Therefore, the concentration of particles calculated by the software is usually not representative of the actual concentration in the sample.

## 12. Conclusion

The multifarious decay of the single intrinsic Tyr in the A $\beta$  peptide carries a variety of information on peptide activity and conformation. It has been confirmed that Tyr fluorescence decay responds to the changes in its environment induced by peptide oligomerization at its earliest stages. But like most intrinsic fluorophores in proteins, Tyr exhibits complex fluorescence decay kinetics. Such complexity precludes any straightforward interpretation of the time-resolved fluorescence data. The use of TRES in this case provides additional information that can help understand the underlying kinetics of this complex system.

The changes observed in the TRES of A $\beta$ <sub>1-40</sub> during aggregation indicate at least two different sub-systems of fluorescent tyrosine: one originating from Tyr in monomers and the other from Tyr in oligomers. The latter decay is highly influenced by the dielectric relaxation process and the continuous distribution of fluorescence parameters of oligomers formed in the sample, thus can be used to determine the extent of aggregation. Therefore, kinetic models combining both dielectric relaxation and heterogeneity of the fluorescence residues should be considered to properly represent the fluorescence characteristics of the heterogenic molecular system.

Most fluorescence methods are evidently sensitive to fibril formation (i.e. the formation of A $\beta$  beta-sheets), but lack the specificity to detect A $\beta$  oligomerization. Thus, our method of using TRES of the intrinsic Tyr is unique in its ability of detecting oligomerization at its earliest stages without perturbing the native structure with extrinsic probes, as well as providing valuable information that can help understand the underlying kinetics of this complicated molecular system.

Substantial differences are observed in A $\beta$ <sub>1-40</sub> time-resolved fluorescence responses in the presence of specific factors like copper ions and glucose as well as anti-aggregation

compounds like quercetin. Thus, we believe that this approach offers the possibility for identifying different types of amyloid aggregates induced by the presence of particular factors.

Time resolved spectroscopy show that the formation of  $\text{Cu}^{2+}$ - $\text{A}\beta_{1-40}$  complexes substantially accelerate the process of peptide aggregation. TRES measurements obtained for  $\text{A}\beta_{1-40}$  in the presence of  $\text{Cu}^{2+}$  show that the emission peak of  $\text{A}\beta_{1-40}$  aggregates shift substantially with time of incubation, which indicates a different  $\text{A}\beta_{1-40}$  aggregation pathway leading to the formation of different types of aggregates induced by the presence of  $\text{Cu}^{2+}$ .

TRES measurements of  $\text{A}\beta_{1-40}$  in the presence of glucose indicate the existence of more than two fluorescent species: the typical monomers observed in free  $\text{A}\beta_{1-40}$ , but at much lower concentrations, and more than one type of oligomers each with its own fluorescence intensity decay and dielectric relaxation rate. The overall changes observed in TRES indicate that glucose alters the aggregation pathway.

TRES data obtained for  $\text{A}\beta_{1-40}$  in the presence of quercetin suggests that the actual kinetics of the system is more complex than that observed for free  $\text{A}\beta_{1-40}$ . Possibly due to the interactions between  $\text{A}\beta_{1-40}$  aggregates and Quercetin, and the existence of more than two fluorescent species. At a molar ratio of 1:1 ( $\text{A}\beta_{1-40}$  : Quercetin) aggregates increase in number rather than size, which suggests that the early formation of  $\text{A}\beta$ -Quercetin complexes somehow inhibit further  $\text{A}\beta$  aggregation.

In spite of the amount of information provided by the obtained TRES measurements, there is still room to improve these findings by using a pulsed light source with a much higher repetition rate (10-100 MHz DeltaDiode; HORIBA, UK), a high-speed detector and ultra-low deadtime electronics (DeltaFlex TCSPC system; HORIBA, UK). This would significantly reduce the time needed to measure the fluorescence decays, which

would enhance the number of decays that can be measured across the fluorophores spectrum for each TRES measurement, which would in turn improve the validity of the results. It would also allow for TRES measurements of fluorescent species with very weak emission such as those observed for A $\beta$ <sub>1-40</sub> at wavelengths between 330-445 nm (see section 8.2).

The fluorescence anisotropy decay technique was also used to study A $\beta$ <sub>1-40</sub> aggregation in the absence and presence of glucose and quercetin in an effort to explore the synergy of combining different experimental techniques. Anisotropy decay measurements using the intrinsic Tyr allow detection of small A $\beta$ <sub>1-40</sub> aggregates. Larger aggregates, on the other hand, are untraceable due to their low quantum yields. Thus, the gradual growth in the size of A $\beta$ <sub>1-40</sub> aggregates with time of incubation reaches maximum after 195 hr. In the presence of quercetin, A $\beta$ <sub>1-40</sub> aggregates reach their maximum size within 22 hr and then stop developing, which is consistent with results obtained from TRES and the ThT binding assay confirming quercetin's inhibitory effect on amyloid fibril formation. Anisotropy decay measurements of A $\beta$ <sub>1-40</sub> in the presence of glucose are almost identical to those obtained for free A $\beta$ <sub>1-40</sub> during the first 200 hr of incubation. Given that glycation processes typically take few weeks and that the fluorescence intensity of Tyr in A $\beta$ <sub>1-40</sub> aggregates is significantly reduced after ~260 hr, glycation effects cannot be monitored using this technique.

The NTA technique as used in this study allows one to visualize and measure monodispersed particles in the size range ~100-1000 nm. It is used as a complementary technique to study the effect of quercetin on A $\beta$ <sub>1-40</sub> fibril formation, particularly for late stages of the aggregation process, without perturbing the native structure with extrinsic probes. Results show that quercetin slightly reduces the rate of the aggregation process. The effect of quercetin is limited in this case probably because of the small

Quercetin:A $\beta_{1-40}$  molar ratio (3:10) and/or the presence of preformed A $\beta_{1-40}$  aggregates in the sample (Batch 2 previously discussed in section 9.2). Another drawback of this technique is related to tracking large A $\beta_{1-40}$  aggregates that usually appear as particles with no clear centre. Such particles cannot be processed by the software and are not included in the analysis. Therefore, the concentration of particles calculated by the software is usually not representative of the actual concentration in the sample.

The TRES technique is unique in its sensitivity to A $\beta_{1-40}$  aggregation at its earliest stages and in providing information that can help understand the underlying kinetics of the molecular system. It can be used to possibly identify and study different types of amyloid aggregates induced by the presence of specific factors that either enhance (e.g. sugars, metal ions) or inhibit (e.g. flavonoids) the aggregation process. It can also be applied on other types of proteins containing intrinsic fluorophores such as Tau and Alpha-synuclein, which are two aggregation-prone species involved in Alzheimer's disease and Parkinson disease respectively.

In future work, it would be beneficial to improve the data acquisition time for TRES measurements through the use of a pulsed light source with a much higher repetition rate (10-100 MHz DeltaDiode; HORIBA, UK), a high-speed detector and ultra-low deadtime electronics (DeltaFlex TCSPC system; HORIBA, UK). Another approach is to measure the series of fluorescence intensity decays simultaneously rather than sequentially by using a 192x128 time correlated SPAD camera<sup>220</sup>, which can be adapted to collect simultaneously fluorescence intensity decays at different wavelengths. However, the SPAD camera can only operate in the detection range ~400-900 nm. Accordingly, we cannot use the intrinsic fluorophores Trp, Tyr and Phe in this approach, which necessitates the use of extrinsic probes.

Another area that could be investigated in future work is the possible interactions (FRET) between intrinsic Phe and Tyr in A $\beta$ <sub>1-40</sub> as aggregation progresses, which might provide further insight on the underlying kinetics of this complex system.

In addition, the experimentally measured TRES can be used to verify an unlimited number of kinetic models that are established from the numerical modelling of excited-state kinetics.

## References

1. He, W., Goodkind, D. & Kowal, P. R. An aging world: 2015. (2016).
2. Hou, Y. *et al.* Ageing as a risk factor for neurodegenerative disease. *Nat. Rev. Neurol.* **15**, 565–581 (2019).
3. Watremez, W. *et al.* Stabilized Low-n Amyloid- $\beta$  Oligomers Induce Robust Novel Object Recognition Deficits Associated with Inflammatory, Synaptic, and GABAergic Dysfunction in the Rat. *J. Alzheimer's Dis.* **62**, 213–226 (2018).
4. Lacor, P. N. Advances on the understanding of the origins of synaptic pathology in AD. *Curr. Genomics* **8**, 486–508 (2007).
5. Ferreira, S. T. & Klein, W. L. The A $\beta$  oligomer hypothesis for synapse failure and memory loss in Alzheimer's disease. *Neurobiol. Learn. Mem.* **96**, 529–543 (2011).
6. Lesné, S. *et al.* A specific amyloid- $\beta$  protein assembly in the brain impairs memory. *Nature* **440**, 352–357 (2006).
7. Caughey, B. & Lansbury Jr, P. T. Protofibrils, pores, fibrils, and neurodegeneration: separating the responsible protein aggregates from the innocent bystanders. *Annu. Rev. Neurosci.* **26**, 267–298 (2003).
8. Kim, T. *et al.* Human LILRB2 is a  $\beta$ -amyloid receptor and its murine homolog PirB regulates synaptic plasticity in an Alzheimer's model. *Science* (80-. ). **341**, 1399–1404 (2013).
9. Murphy, M. & LeVine III, H. Alzheimer's disease and the  $\beta$ -amyloid peptide. *J Alzheimers Dis* **19**, 311–323 (2010).
10. Norlin, N. *et al.* Aggregation and fibril morphology of the Arctic mutation of

- Alzheimer's A $\beta$  peptide by CD, TEM, STEM and in situ AFM. *J. Struct. Biol.* **180**, 174–189 (2012).
11. Bartolini, M. *et al.* Kinetic characterization of amyloid-beta 1–42 aggregation with a multimethodological approach. *Anal. Biochem.* **414**, 215–225 (2011).
  12. Adamcik, J. & Mezzenga, R. Study of amyloid fibrils via atomic force microscopy. *Curr. Opin. Colloid Interface Sci.* **17**, 369–376 (2012).
  13. Marion, D. An introduction to biological NMR spectroscopy. *Mol. Cell. Proteomics* **12**, 3006–3025 (2013).
  14. Fawzi, N. L., Ying, J., Ghirlando, R., Torchia, D. A. & Clore, G. M. Atomic-resolution dynamics on the surface of amyloid- $\beta$  protofibrils probed by solution NMR. *Nature* **480**, 268–272 (2011).
  15. Chen, K., Maley, J. & Yu, P. H. Potential implications of endogenous aldehydes in  $\beta$ -amyloid misfolding, oligomerization and fibrillogenesis. *J. Neurochem.* **99**, 1413–1424 (2006).
  16. Li, X. H. *et al.* Glycation exacerbates the neuronal toxicity of  $\beta$ -amyloid. *Cell Death Dis.* **4**, e673 (2013).
  17. Kaye, R. *et al.* Fibril specific, conformation dependent antibodies recognize a generic epitope common to amyloid fibrils and fibrillar oligomers that is absent in prefibrillar oligomers. *Mol. Neurodegener.* **2**, 1–11 (2007).
  18. Perchiacca, J. M., Ladiwala, A. R. A., Bhattacharya, M. & Tessier, P. M. Structure-based design of conformation- and sequence-specific antibodies against amyloid  $\beta$ . *Proc. Natl. Acad. Sci.* **109**, 84–89 (2012).
  19. Tsien, R. Y. Building and breeding molecules to spy on cells and tumors. *FEBS Lett.*

- 579, 927–932 (2005).
20. Kobayashi, H., Ogawa, M., Alford, R., Choyke, P. L. & Urano, Y. New strategies for fluorescent probe design in medical diagnostic imaging. *Chem. Rev.* **110**, 2620–2640 (2010).
  21. W Bertoncini, C. & Soledad Celej, M. Small molecule fluorescent probes for the detection of amyloid self-assembly in vitro and in vivo. *Curr. Protein Pept. Sci.* **12**, 206–220 (2011).
  22. Shahzad, A., Edetsberger, M. & Koehler, G. Fluorescence spectroscopy: An emerging excellent diagnostic tool in medical sciences. *Appl. Spectrosc. Rev.* **45**, 1–11 (2010).
  23. Drezek, R. A. *et al.* Understanding the contributions of NADH and collagen to cervical tissue fluorescence spectra: modeling, measurements, and implications. *J. Biomed. Opt.* **6**, 385–396 (2001).
  24. Pires, L., Nogueira, M. S., Pratavieira, S., Moriyama, L. T. & Kurachi, C. Time-resolved fluorescence lifetime for cutaneous melanoma detection. *Biomed. Opt. Express* **5**, 3080–3089 (2014).
  25. Miller, J. P., Habimana-Griffin, L., Edwards, T. S. & Achilefu, S. Multimodal fluorescence molecular imaging for in vivo characterization of skin cancer using endogenous and exogenous fluorophores. *J. Biomed. Opt.* **22**, 66007 (2017).
  26. Batzli, K. M. & Love, B. J. Agitation of amyloid proteins to speed aggregation measured by ThT fluorescence: a call for standardization. *Mater. Sci. Eng. C* **48**, 359–364 (2015).
  27. Guo, J., Yu, L., Sun, Y. & Dong, X. Kinetic insights into Zn<sup>2+</sup>-induced amyloid  $\beta$ -protein aggregation revealed by stopped-flow fluorescence spectroscopy. *J. Phys.*

- Chem. B* **121**, 3909–3917 (2017).
28. Girych, M. *et al.* Combined thioflavin T–Congo red fluorescence assay for amyloid fibril detection. *Methods Appl. Fluoresc.* **4**, 34010 (2016).
  29. Amaro, M., Birch, D. J. S. & Rolinski, O. J. Beta-amyloid oligomerisation monitored by intrinsic tyrosine fluorescence. *Phys. Chem. Chem. Phys.* **13**, 6434–6441 (2011).
  30. Wu, J. W. *et al.* Fibrillar oligomers nucleate the oligomerization of monomeric amyloid  $\beta$  but do not seed fibril formation. *J. Biol. Chem.* **285**, 6071–6079 (2010).
  31. Chen, W.-T., Liao, Y.-H., Yu, H.-M., Cheng, I. H. & Chen, Y.-R. Distinct effects of  $Zn^{2+}$ ,  $Cu^{2+}$ ,  $Fe^{3+}$ , and  $Al^{3+}$  on amyloid- $\beta$  stability, oligomerization, and aggregation: amyloid- $\beta$  destabilization promotes annular protofibril formation. *J. Biol. Chem.* **286**, 9646–9656 (2011).
  32. Sengupta, U., Nilson, A. N. & Kaye, R. The role of amyloid- $\beta$  oligomers in toxicity, propagation, and immunotherapy. *EBioMedicine* **6**, 42–49 (2016).
  33. Younan, N. D. & Viles, J. H. A comparison of three fluorophores for the detection of amyloid fibers and prefibrillar oligomeric assemblies. ThT (thioflavin T); ANS (1-anilinonaphthalene-8-sulfonic acid); and bisANS (4, 4'-dianilino-1, 1'-binaphthyl-5, 5'-disulfonic acid). *Biochemistry* **54**, 4297–4306 (2015).
  34. Mishra, R., Sjölander, D. & Hammarström, P. Spectroscopic characterization of diverse amyloid fibrils in vitro by the fluorescent dye Nile red. *Mol. Biosyst.* **7**, 1232–1240 (2011).
  35. Wu, C., Scott, J. & Shea, J.-E. Binding of Congo red to amyloid protofibrils of the Alzheimer A $\beta$ 9–40 peptide probed by molecular dynamics simulations. *Biophys. J.* **103**, 550–557 (2012).

36. D'Amico, M. *et al.* Thioflavin T promotes A $\beta$  (1–40) amyloid fibrils formation. *J. Phys. Chem. Lett.* **3**, 1596–1601 (2012).
37. Amaro, M. *et al.* Inhibition of beta-amyloid aggregation by fluorescent dye labels  
Inhibition of beta-amyloid aggregation by fluorescent dye labels. *Appl. Phys. Lett.* **104**, 063704 (2014).
38. Seubert, P. *et al.* Isolation and quantification of soluble Alzheimer's beta-peptide from biological fluids. *Nature* **359**, 325–327 (1992).
39. Kontush, A. Amyloid-B : An antioxidant that becomes a pro-oxidant and critically contributes to Alzheimer's disease. *Free Radic. Biol. Med.* **31**, 1120–1131 (2001).
40. Hou, L. *et al.* Solution NMR Studies of the A $\beta$ (1-40) and A $\beta$ (1-42) Peptides Establish that the Met35 Oxidation State Affects the Mechanism of Amyloid Formation. *J. Am. Chem. Soc.* **126**, 1992–2005 (2004).
41. Hardy, J. & Selkoe, D. J. The Amyloid Hypothesis of Alzheimer ' s Disease : Progress and Problems on the Road to Therapeutics. *Science (80- )*. **297**, 353–356 (2002).
42. Mori, H., Takio, K., Ogawara, M. & Selkoe, D. J. Mass spectrometry of purified amyloid beta protein in Alzheimer's disease. *J. Biol. Chem.* **267**, 17082–17086 (1992).
43. García-Viñuales, S. *et al.* Trehalose conjugates of silybin as prodrugs for targeting toxic A $\beta$  aggregates. *ACS Chem. Neurosci.* **11**, 2566–2576 (2020).
44. Greenberg, S. M. *et al.* Cerebral amyloid angiopathy and Alzheimer disease—One peptide, two pathways. *Nat. Rev. Neurol.* **16**, 30–42 (2020).
45. Rolinski, O. J., Wellbrock, T., Birch, D. J. S. & Vyshemirsky, V. Tyrosine Photophysics during the Early Stages of B-Amyloid Aggregation Leading to Alzheimer's. *J. Phys. Chem. Lett.* **6**, 3116–3120 (2015).

46. Rolinski, O. J., Amaro, M. & Birch, D. J. S. Early detection of amyloid aggregation using intrinsic fluorescence. *Biosens. Bioelectron.* **25**, 2249–2252 (2010).
47. Sipe, J. D. *et al.* Amyloid fibril proteins and amyloidosis: chemical identification and clinical classification International Society of Amyloidosis 2016 Nomenclature Guidelines. *Amyloid* **23**, 209–213 (2016).
48. Iadanza, M. G., Jackson, M. P., Hewitt, E. W. & Ranson, N. A. A new era for understanding amyloid. *Nat. Rev. Mol. Cell Biol.* **19**, (2018).
49. Westermark, P. Localized AL amyloidosis : A suicidal neoplasm ? *Ups. J. Med. Sci.* **117**, 244–250 (2012).
50. Sipe, J. D. *et al.* Amyloid fibril proteins and amyloidosis : chemical identification and clinical classification International Society of Amyloidosis 2016 Nomenclature Guidelines Amyloid fibril proteins and amyloidosis : chemical identification and clinical classification I. *Amyloid* **23**, 209–213 (2016).
51. Fitzpatrick, A. W. P., Debelouchina, G. T., Bayro, M. J., Clare, D. K. & Caporini, M. A. Atomic structure and hierarchical assembly of a cross-  $\beta$  amyloid fibril. *Proc. Natl. Acad. Sci.* **201219476**, (2013).
52. Gremer, L. *et al.* Fibril structure of amyloid- b (1 – 42) by cryo – electron microscopy. *Science (80-. ).* **358**, 116–119 (2017).
53. Colvin, M. T. *et al.* High Resolution Structural Characterization of A  $\beta$  42 Amyloid Fibrils by Magic Angle Spinning NMR. *J. Am. Chem. Soc.* **137**, 7509–7518 (2015).
54. Tycko, R. Solid-State NMR Studies of Amyloid Fibril Structure. *Annu. Rev. Phys. Chem.* **62**, 279–299 (2011).
55. Ferrone, F. [17] Analysis of protein aggregation kinetics. *methods Enzymol.* **309**, 256–

- 274 (1999).
56. Cohen, S. I. A., Vendruscolo, M., Dobson, C. M. & Knowles, T. P. J. From Macroscopic Measurements to Microscopic Mechanisms of Protein Aggregation. *J. Mol. Biol.* **421**, 160–171 (2012).
  57. Glabe, C. G. Common mechanisms of amyloid oligomer pathogenesis in degenerative disease. *Neurobiol. Aging* **27**, 570–575 (2006).
  58. Meisl, G. *et al.* Molecular mechanism of protein aggregation from global fitting of kinetic models. *Nat. Protoc.* **11**, 252 (2016).
  59. Enserink, M. First Alzheimer's diagnosis confirmed. (1998).
  60. Glenner, G. G. & Wong, C. W. Alzheimer's disease: initial report of the purification and characterization of a novel cerebrovascular amyloid protein. *Biochem. Biophys. Res. Commun.* **120**, 885–890 (1984).
  61. Grundke-Iqbal, I. *et al.* Abnormal phosphorylation of the microtubule-associated protein tau (tau) in Alzheimer cytoskeletal pathology. *Proc. Natl. Acad. Sci.* **83**, 4913–4917 (1986).
  62. Cheignon, C. *et al.* Oxidative stress and the amyloid beta peptide in Alzheimer's disease. *Redox Biol.* **14**, 450–464 (2018).
  63. Dent, E. W. & Baas, P. W. Microtubules in neurons as information carriers. *J. Neurochem.* **129**, 235–239 (2014).
  64. Giraldo, E., Lloret, A., Fuchsberger, T. & Viña, J. A $\beta$  and tau toxicities in Alzheimer's are linked via oxidative stress-induced p38 activation: protective role of vitamin E. *Redox Biol.* **2**, 873–877 (2014).

65. Bao, F. *et al.* Different  $\beta$ -amyloid oligomer assemblies in Alzheimer brains correlate with age of disease onset and impaired cholinergic activity. *Neurobiol. Aging* **33**, 825-e1 (2012).
66. Esparza, T. J. *et al.* Amyloid-beta oligomerization in Alzheimer dementia versus high-pathology controls. *Ann. Neurol.* **73**, 104–119 (2013).
67. Rachakonda, V., Pan, T. H. & Le, W. D. Biomarkers of neurodegenerative disorders: how good are they? *Cell Res.* **14**, 349–358 (2004).
68. Sjögren, M., Andreasen, N. & Blennow, K. Advances in the detection of Alzheimer's disease—use of cerebrospinal fluid biomarkers. *Clin. Chim. Acta* **332**, 1–10 (2003).
69. Mapstone, M. *et al.* Plasma phospholipids identify antecedent memory impairment in older adults. *Nat. Med.* **20**, 415–418 (2014).
70. Agrawal, M. & Biswas, A. Molecular diagnostics of neurodegenerative disorders. *Front. Mol. Biosci.* **2**, 54 (2015).
71. Lue, L.-F., Guerra, A. & Walker, D. G. Amyloid beta and tau as Alzheimer's disease blood biomarkers: promise from new technologies. *Neurol. Ther.* **6**, 25–36 (2017).
72. Kaneko, N., Yamamoto, R., Sato, T.-A. & Tanaka, K. Identification and quantification of amyloid beta-related peptides in human plasma using matrix-assisted laser desorption/ionization time-of-flight mass spectrometry. *Proc. Japan Acad. Ser. B* **90**, 104–117 (2014).
73. Moreira, P. I. *et al.* The key role of oxidative stress in Alzheimer's disease. *Oxidative Stress Neurodegener. Disord.* **451**, 466 (2007).
74. Atwood, C. S. *et al.* Amyloid- $\beta$ : a chameleon walking in two worlds: a review of the trophic and toxic properties of amyloid- $\beta$ . *Brain Res. Rev.* **43**, 1–16 (2003).

75. Johns, P. *Clinical Neuroscience E-Book*. (Elsevier Health Sciences, 2014).
76. Selkoe, D. J. Alzheimer ' s Disease : Genes , Proteins , and Therapy. *Physiol. Rev.* **81**, 741–766 (2001).
77. Dulin, F. *et al.* p3 peptide, a truncated form of A $\beta$  devoid of synaptotoxic effect, does not assemble into soluble oligomers. *FEBS Lett.* **582**, 1865–1870 (2008).
78. Walsh, D. M. *et al.* Naturally secreted oligomers of amyloid  $\beta$  protein potently inhibit hippocampal long-term potentiation in vivo. *Nature* **416**, 535–539 (2002).
79. Benilova, I., Karran, E. & De Strooper, B. The toxic A $\beta$  oligomer and Alzheimer's disease: an emperor in need of clothes. *Nat. Neurosci.* **15**, 349 (2012).
80. Danev, R., Yanagisawa, H. & Kikkawa, M. Cryo-electron microscopy methodology: current aspects and future directions. *Trends Biochem. Sci.* **44**, 837–848 (2019).
81. Chiti, F. & Dobson, C. M. Protein misfolding, amyloid formation, and human disease: a summary of progress over the last decade. *Annu. Rev. Biochem.* **86**, 27–68 (2017).
82. Li, H. *et al.* Amyloids and protein aggregation—Analytical methods. *Encycl. Anal. Chem. Appl. Theory Instrum.* (2006).
83. Oboroceanu, D., Wang, L., Brodkorb, A., Magner, E. & Auty, M. A. E. Characterization of  $\beta$ -lactoglobulin fibrillar assembly using atomic force microscopy, polyacrylamide gel electrophoresis, and in situ Fourier transform infrared spectroscopy. *J. Agric. Food Chem.* **58**, 3667–3673 (2010).
84. Ovenall, D. W. & Peaker, F. W. A light scattering instrument for molecular weight measurements. *Die Makromol. Chemie Macromol. Chem. Phys.* **33**, 222–236 (1959).
85. Uskoković, V. Dynamic light scattering based microelectrophoresis: main prospects

- and limitations. *J. Dispers. Sci. Technol.* **33**, 1762–1786 (2012).
86. Eshel, G., Levy, G. J., Mingelgrin, U. & Singer, M. J. Critical evaluation of the use of laser diffraction for particle-size distribution analysis. *Soil Sci. Soc. Am. J.* **68**, 736–743 (2004).
  87. Berne, B. J. & Pecora, R. *Dynamic light scattering: with applications to chemistry, biology, and physics*. (Courier Corporation, 2000).
  88. Berova, N., Nakanishi, K. & Woody, R. W. *Circular dichroism: principles and applications*. (John Wiley & Sons, 2000).
  89. Liang, J. N. & Chylack Jr, L. T. Change in the protein tertiary structure with non-enzymatic glycosylation of calf alpha-crystallin. *Biochem. Biophys. Res. Commun.* **123**, 899–906 (1984).
  90. Selling, G. W., Hamaker, S. A. H. & Sessa, D. J. Effect of solvent and temperature on secondary and tertiary structure of zein by circular dichroism. *Cereal Chem.* **84**, 265–270 (2007).
  91. Greenfield, N. J. Using circular dichroism spectra to estimate protein secondary structure. *Nat. Protoc.* **1**, 2876 (2006).
  92. Khrapunov, S. Circular dichroism spectroscopy has intrinsic limitations for protein secondary structure analysis. *Anal. Biochem.* **389**, 174–176 (2009).
  93. Fink, A. L. Protein aggregation: folding aggregates, inclusion bodies and amyloid. *Fold. Des.* **3**, R9–R23 (1998).
  94. Krimm, S. & Bandekar, J. in *Advances in protein chemistry* **38**, 181–364 (Elsevier, 1986).

95. Zandomenighi, G., Krebs, M. R. H., McCammon, M. G. & Fändrich, M. FTIR reveals structural differences between native  $\beta$ -sheet proteins and amyloid fibrils. *Protein Sci.* **13**, 3314–3321 (2004).
96. Hawe, A., Sutter, M. & Jiskoot, W. Extrinsic fluorescent dyes as tools for protein characterization. *Pharm. Res.* **25**, 1487–1499 (2008).
97. Kato, A. & Nakai, S. Hydrophobicity determined by a fluorescence probe method and its correlation with surface properties of proteins. *Biochim. Biophys. Acta (BBA)-Protein Struct.* **624**, 13–20 (1980).
98. Sirangelo, I., Bismuto, E., Tavassi, S. & Irace, G. Apomyoglobin folding intermediates characterized by the hydrophobic fluorescent probe 8-anilino-1-naphthalene sulfonate (ANS). *Biochim. Biophys. Acta (BBA)-Protein Struct. Mol. Enzymol.* **1385**, 69–77 (1998).
99. Naiki, H., Higuchi, K., Hosokawa, M. & Takeda, T. Fluorometric determination of amyloid fibrils in vitro using the fluorescent dye, thioflavine T. *Anal. Biochem.* **177**, 244–249 (1989).
100. LeVine III, H. in *Methods in enzymology* **309**, 274–284 (Elsevier, 1999).
101. Khurana, R. *et al.* Mechanism of thioflavin T binding to amyloid fibrils. *J. Struct. Biol.* **151**, 229–238 (2005).
102. Klunk, W. E. *et al.* Uncharged thioflavin-T derivatives bind to amyloid-beta protein with high affinity and readily enter the brain. *Life Sci.* **69**, 1471–1484 (2001).
103. Elson, E. L. & Magde, D. Fluorescence correlation spectroscopy. I. Conceptual basis and theory. *Biopolym. Orig. Res. Biomol.* **13**, 1–27 (1974).
104. Tian, Y., Martinez, M. M. & Pappas, D. Fluorescence correlation spectroscopy: a

- review of biochemical and microfluidic applications. *Appl. Spectrosc.* **65**, 115A–124A (2011).
105. Guan, Y. *et al.* Real-Time Monitoring of Alzheimer's-Related Amyloid Aggregation via Probe Enhancement–Fluorescence Correlation Spectroscopy. *ACS Chem. Neurosci.* **6**, 1503–1508 (2015).
  106. Tiiman, A., Jarvet, J., Gräslund, A. & Vukojević, V. Heterogeneity and turnover of intermediates during amyloid- $\beta$  (A $\beta$ ) peptide aggregation studied by fluorescence correlation spectroscopy. *Biochemistry* **54**, 7203–7211 (2015).
  107. Nandi, S. *et al.* Amyloid beta peptides inside a reconstituted cell-like liposomal system: aggregation, FRET, fluorescence oscillations and solvation dynamics. *Phys. Chem. Chem. Phys.* **18**, 30444–30451 (2016).
  108. Hudson, S. A., Ecroyd, H., Kee, T. W. & Carver, J. A. The thioflavin T fluorescence assay for amyloid fibril detection can be biased by the presence of exogenous compounds. *FEBS J.* **276**, 5960–5972 (2009).
  109. Procházka, K. *Fluorescence studies of polymer containing systems.* **16**, (Springer, 2016).
  110. Wardle, B. *Principles and applications of photochemistry.* (John Wiley & Sons, 2009).
  111. Atkins, P. W. & Friedman, R. S. *Molecular quantum mechanics.* (Oxford university press, 2011).
  112. Lakowicz, J. R. *Principles of Fluorescence Spectroscopy.* (2000).
  113. del Valle, J. C. & Catalán, J. Kasha's rule: a reappraisal. *Phys. Chem. Chem. Phys.* **21**, 10061–10069 (2019).

114. McNaught, A. D. & Wilkinson, A. *Compendium of chemical terminology*. **1669**, (Blackwell Science Oxford, 1997).
115. Lakowicz, J. R. *Principles of Fluorescence Spectroscopy* Joseph R . Lakowicz.
116. Kaletunc, G. & Breslauer, K. J. *Characterization of Cereals and Flours: Properties, Analysis And Applications*. (CRC Press, 2003).
117. Andrews, D. L. *Photonics, Volume 4: Biomedical Photonics, Spectroscopy, and Microscopy*. (Wiley, 2015).
118. Kautsky, H. Quenching of luminescence by oxygen. *Trans. Faraday Soc.* **35**, 216–219 (1939).
119. Phillips, S. R., Wilson, L. J. & Borkman, R. F. Acrylamide and iodide fluorescence quenching as a structural probe of tryptophan microenvironment in bovine lens crystallins. *Curr. Eye Res.* **5**, 611–620 (1986).
120. Lehrer, S. S. & Leavis, P. C. in *Methods in enzymology* **49**, 222–236 (Elsevier, 1978).
121. Weber, G. The quenching of fluorescence in liquids by complex formation. Determination of the mean life of the complex. *Trans. Faraday Soc.* **44**, 185–189 (1948).
122. Eftink, M. R. in *Topics in fluorescence spectroscopy* 1–15 (Springer, 2002).
123. Petrich, J. W., Chang, M. C., McDonald, D. B. & Fleming, G. R. On the origin of nonexponential fluorescence decay in tryptophan and its derivatives. *J. Am. Chem. Soc.* **105**, 3824–3832 (1983).
124. Szabo, A. G. & Rayner, D. M. Fluorescence Decay of Tryptophan Conformers in aqueous solution. *J. Am. Chem. Soc.* **102**, 554–563 (1980).

125. Dahms, T. E. S., Willis, K. J. & Szabo, A. G. Conformational Heterogeneity of Tryptophan in a Protein Crystal. *J. Am. Chem. Soc.* **117**, 2321–2326 (1995).
126. Amaro, M., Birch, D. J. S. & Rolinski, O. J. Beta-amyloid oligomerisation monitored by intrinsic tyrosine fluorescence. 6434–6441 (2011). doi:10.1039/c0cp02652b
127. Lakowicz, J. R. On Spectral Relaxation in Proteins†¶¶. *Photochem. Photobiol.* **72**, 421–437 (2000).
128. Pan, C., Mui, P. L., Barkley, M. D. & Callis, P. R. Correlation of Tryptophan Fluorescence Spectral Shifts and Lifetimes Arising Directly from Heterogeneous Environment. *J. Phys. Chem. B* **115**, 3245–3253 (2011).
129. Toptygin, D. & Brand, L. Spectrally-and time-resolved fluorescence emission of indole during solvent relaxation: a quantitative model. *Chem. Phys. Lett.* **322**, 496–502 (2000).
130. Lakowicz, J. R. & Gryczynski, I. in *Topics in fluorescence spectroscopy* 293–335 (Springer, 2002).
131. Prendergast, F. G. Time-resolved fluorescence techniques: methods and applications in biology. *Curr. Opin. Struct. Biol.* **1**, 1054–1059 (1991).
132. Philip, J. & Carlsson, K. Theoretical investigation of the signal-to-noise ratio in fluorescence lifetime imaging. *JOSA A* **20**, 368–379 (2003).
133. Eaton, D. F. Recommended methods for fluorescence decay analysis. *Pure Appl. Chem.* **62**, 1631–1648 (1990).
134. Hungerford, G. & Birch, D. J. S. Single-photon timing detectors for fluorescence lifetime spectroscopy. *Meas. Sci. Technol.* **7**, 121 (1996).

135. Scientific, H. Time-resolved fluorescence lifetime measurements. Available at: [https://static.horiba.com/fileadmin/Horiba/Products/Scientific/Molecular\\_and\\_Microanalysis/DeltaFlex/TechNote-1b-Time-resolved\\_fluorescence\\_lifetime\\_measurements.pdf](https://static.horiba.com/fileadmin/Horiba/Products/Scientific/Molecular_and_Microanalysis/DeltaFlex/TechNote-1b-Time-resolved_fluorescence_lifetime_measurements.pdf). (Accessed: 13th August 2021)
136. Ware, W. R., Lee, S. K., Brant, G. J. & Chow, P. P. Nanosecond time-resolved emission spectroscopy: spectral shifts due to solvent-excited solute relaxation. *J. Chem. Phys.* **54**, 4729–4737 (1971).
137. McGuinness, C. D., Sagoo, K., Mcloskey, D. & Birch, D. J. S. A new sub-nanosecond LED at 280 nm : *Meas. Sci. Technol.* **15**, L19-22 (2004).
138. Alghamdi, A., Forbes, S., Birch, D. J. S., Vyshemirsky, V. & Rolinski, O. J. Detecting beta-amyloid glycation by intrinsic fluorescence-Understanding the link between diabetes and Alzheimer’s disease. *Arch. Biochem. Biophys.* **704**, 108886 (2021).
139. Stine, W. B., Dahlgren, K. N., Krafft, G. A. & LaDu, M. J. In vitro characterization of conditions for amyloid- $\beta$  peptide oligomerization and fibrillogenesis. *J. Biol. Chem.* **278**, 11612–11622 (2003).
140. Amaro, M., Kubiak-ossowska, K., Birch, D. J. S. & Rolinski, O. J. Initial stages of beta-amyloid A  $\beta$  1 – 40 and A  $\beta$  1 – 42 oligomerization observed using fluorescence decay and molecular dynamics analyses of tyrosine. *Methods Appl. Fluoresc.* **1**, 015006 (2013).
141. Rolinski, O. J. & Vyshemirsky, V. Fluorescence kinetics of tryptophan in a heterogeneous environment. *Methods Appl. Fluoresc.* **2**, 045002 (2014).
142. Rolinski, O. J., McLaughlin, D., Birch, D. J. S. & Vyshemirsky, V. Resolving environmental microheterogeneity and dielectric relaxation in fluorescence kinetics of

- protein. *Methods Appl. Fluoresc.* **4**, 024001 (2016).
143. Alghamdi, A., Vyshemirsky, V., Birch, D. J. S. & Rolinski, O. J. Detecting beta-amyloid aggregation from time-resolved emission spectra. *Methods Appl. Fluoresc.* **6**, 24002 (2018).
144. Bush, A. I. The metallobiology of Alzheimer's disease. *Trends Neurosci.* **26**, 207–214 (2003).
145. Adlard, P. A. & Bush, A. I. Metals and Alzheimer's disease. *J. Alzheimer's Dis.* **10**, 145–163 (2006).
146. Minicozzi, V. *et al.* Identifying the minimal copper- and zinc-binding site sequence in amyloid- $\beta$  peptides. *J. Biol. Chem.* **283**, 10784–10792 (2008).
147. Hureau, C. Coordination of redox active metal ions to the amyloid precursor protein and to amyloid- $\beta$  peptides involved in Alzheimer disease. Part 1: An overview. *Coord. Chem. Rev.* **256**, 2164–2174 (2012).
148. Faller, P. & Hureau, C. Bioinorganic chemistry of copper and zinc ions coordinated to amyloid- $\beta$  peptide. *Dalt. Trans.* 1080–1094 (2009).
149. Dong, J. *et al.* Metal binding and oxidation of amyloid- $\beta$  within isolated senile plaque cores: Raman microscopic evidence. *Biochemistry* **42**, 2768–2773 (2003).
150. Borghesani, V., Alies, B. & Hureau, C. Cu (II) binding to various forms of amyloid- $\beta$  peptides. Are they friends or foes? *Eur. J. Inorg. Chem.* **2018**, 7 (2018).
151. Branch, T., Girvan, P., Barahona, M. & Ying, L. Introduction of a Fluorescent Probe to Amyloid- $\beta$  to Reveal Kinetic Insights into Its Interactions with Copper (II). *Angew. Chemie* **127**, 1243–1246 (2015).

152. Pedersen, J. T. *et al.* Rapid formation of a preoligomeric peptide–metal–peptide complex following copper (II) binding to amyloid  $\beta$  peptides. *Angew. Chemie* **123**, 2580–2583 (2011).
153. Alghamdi, A., Wellbrock, T., Birch, D. J. S., Vyshemirsky, V. & Rolinski, O. J.  $\text{Cu}^{2+}$  Effects on Beta-Amyloid Oligomerisation Monitored by the Fluorescence of Intrinsic Tyrosine. *ChemPhysChem* **20**, 3181–3185 (2019).
154. Vitek, M. P. *et al.* Advanced glycation end products contribute to amyloidosis in Alzheimer disease. *Proc. Natl. Acad. Sci.* **91**, 4766–4770 (1994).
155. Münch, G. *et al.* Influence of advanced glycation end-products and AGE-inhibitors on nucleation-dependent polymerization of  $\beta$ -amyloid peptide. *Biochim. Biophys. Acta (BBA)-Molecular Basis Dis.* **1360**, 17–29 (1997).
156. Srikanth, V. *et al.* Advanced glycation endproducts and their receptor RAGE in Alzheimer's disease. *Neurobiol. Aging* **32**, 763–777 (2011).
157. Coker, L. H. & Wagenknecht, L. E. Advanced glycation end products, diabetes, and the brain. (2011).
158. Smith, M. A., Vitek, M. P., Monnier, V. M. & Perry, G. Early AGEing and Alzheimer's. *Nature* **374**, 316 (1995).
159. Yaffe, K. *et al.* Advanced glycation end product level, diabetes, and accelerated cognitive aging. *Neurology* **77**, 1351–1356 (2011).
160. Sasaki, N. *et al.* Advanced glycation end products in Alzheimer's disease and other neurodegenerative diseases. *Am. J. Pathol.* **153**, 1149–1155 (1998).
161. Takeuchi, M. & Yamagishi, S. Possible involvement of advanced glycation end-products (AGEs) in the pathogenesis of Alzheimer's disease. *Curr. Pharm. Des.* **14**,

- 973–978 (2008).
162. Chen, C. *et al.* A $\beta$ -AGE aggravates cognitive deficit in rats via RAGE pathway. *Neuroscience* **257**, 1–10 (2014).
  163. Chaney, M. O. *et al.* RAGE and amyloid beta interactions: atomic force microscopy and molecular modeling. *Biochim. Biophys. Acta (BBA)-Molecular Basis Dis.* **1741**, 199–205 (2005).
  164. Chen, K., Kazachkov, M. & Yu, P. H. Effect of aldehydes derived from oxidative deamination and oxidative stress on  $\beta$ -amyloid aggregation; pathological implications to Alzheimer's disease. *J. Neural Transm.* **114**, 835–839 (2007).
  165. Pike, C. J., Overman, M. J. & Cotman, C. W. Amino-terminal deletions enhance aggregation of  $\beta$ -amyloid peptides in vitro. *J. Biol. Chem.* **270**, 23895–23898 (1995).
  166. Luchsinger, J. A., Tang, M.-X., Stern, Y., Shea, S. & Mayeux, R. Diabetes mellitus and risk of Alzheimer's disease and dementia with stroke in a multiethnic cohort. *Am. J. Epidemiol.* **154**, 635–641 (2001).
  167. Lee, J., Culyba, E. K., Powers, E. T. & Kelly, J. W. Amyloid- $\beta$  forms fibrils by nucleated conformational conversion of oligomers. *Nat. Chem. Biol.* **7**, 602 (2011).
  168. Ono, K. & Yamada, M. Low-n oligomers as therapeutic targets of Alzheimer's disease. *J. Neurochem.* **117**, 19–28 (2011).
  169. Gadad, B. S., Britton, G. B. & Rao, K. S. Targeting oligomers in neurodegenerative disorders: lessons from  $\alpha$ -synuclein, tau, and amyloid- $\beta$  peptide. *J. Alzheimer's Dis.* **24**, 223–232 (2011).
  170. Ferrer, J.-L., Austin, M. B., Stewart Jr, C. & Noel, J. P. Structure and function of enzymes involved in the biosynthesis of phenylpropanoids. *Plant Physiol. Biochem.*

- 46**, 356–370 (2008).
171. Jan, S. & Abbas, N. *Himalayan Phytochemicals: Sustainable Options for Sourcing and Developing Bioactive Compounds*. (Elsevier, 2018).
  172. Kay, C. & Cassidy, A. *Encyclopedia of Human Nutrition: Phytochemicals: Classification and Occurrence*. (2013).
  173. Pastor-Villaescusa, B., Rodriguez, E. S. & Rangel-Huerta, O. D. in *Obesity* 213–239 (Elsevier, 2018).
  174. Di Matteo, V., Pierucci, M., Di Giovanni, G. & Esposito, E. in *Oxidative stress and neurodegenerative disorders* 621–661 (Elsevier, 2007).
  175. Lesjak, M. M. *et al.* Phytochemical composition and antioxidant, anti-inflammatory and antimicrobial activities of *Juniperus macrocarpa* Sibth. et Sm. *J. Funct. Foods* **7**, 257–268 (2014).
  176. Echeverría, F., Ortiz, M., Valenzuela, R. & Videla, L. A. Hydroxytyrosol and cytoprotection: A projection for clinical interventions. *Int. J. Mol. Sci.* **18**, 930 (2017).
  177. Molina, M. F., Sanchez-Reus, I., Iglesias, I. & Benedi, J. Quercetin, a flavonoid antioxidant, prevents and protects against ethanol-induced oxidative stress in mouse liver. *Biol. Pharm. Bull.* **26**, 1398–1402 (2003).
  178. Leopoldini, M., Russo, N., Chiodo, S. & Toscano, M. Iron chelation by the powerful antioxidant flavonoid quercetin. *J. Agric. Food Chem.* **54**, 6343–6351 (2006).
  179. Kim, H. *et al.* Effects of naturally occurring compounds on fibril formation and oxidative stress of  $\beta$ -amyloid. *J. Agric. Food Chem.* **53**, 8537–8541 (2005).
  180. Heijnen, C. G. M., Haenen, G. R. M. M., Minou Oostveen, R., Stalpers, E. M. & Bast,

- A. Protection of flavonoids against lipid peroxidation: the structure activity relationship revisited. *Free Radic. Res.* **36**, 575–581 (2002).
181. Zaplatic, E., Bule, M., Shah, S. Z. A., Uddin, M. S. & Niaz, K. Molecular mechanisms underlying protective role of quercetin in attenuating Alzheimer's disease. *Life Sci.* **224**, 109–119 (2019).
182. Porat, Y., Abramowitz, A. & Gazit, E. Inhibition of amyloid fibril formation by polyphenols: structural similarity and aromatic interactions as a common inhibition mechanism. *Chem. Biol. Drug Des.* **67**, 27–37 (2006).
183. Wang, J.-B., Wang, Y.-M. & Zeng, C.-M. Quercetin inhibits amyloid fibrillation of bovine insulin and destabilizes preformed fibrils. *Biochem. Biophys. Res. Commun.* **415**, 675–679 (2011).
184. Zhu, M., Han, S. & Fink, A. L. Oxidized quercetin inhibits  $\alpha$ -synuclein fibrillization. *Biochim. Biophys. Acta (BBA)-General Subj.* **1830**, 2872–2881 (2013).
185. Jiménez-Aliaga, K., Bermejo-Bescós, P., Benedí, J. & Martín-Aragón, S. Quercetin and rutin exhibit antiamyloidogenic and fibril-disaggregating effects in vitro and potent antioxidant activity in APPswe cells. *Life Sci.* **89**, 939–945 (2011).
186. Chen, G. *et al.* Amyloid beta: structure, biology and structure-based therapeutic development. *Acta Pharmacol. Sin.* **38**, 1205–1235 (2017).
187. Srivastava, A. *et al.* Identifying the bond responsible for the fluorescence modulation in an amyloid fibril sensor. *Chem. Eur. J.* **16**, 9257–9263 (2010).
188. Stsiapura, V. I. *et al.* Thioflavin T as a molecular rotor: fluorescent properties of thioflavin T in solvents with different viscosity. *J. Phys. Chem. B* **112**, 15893–15902 (2008).

189. Smith, T. A. & Ghiggino, K. P. A review of the analysis of complex time-resolved fluorescence anisotropy data. *Methods Appl. Fluoresc.* **3**, 22001 (2015).
190. Otsu, T., Nishimoto, E. & Yamashita, S. Multiple conformational state of human serum albumin around single tryptophan residue at various pH revealed by time-resolved fluorescence spectroscopy. *J. Biochem.* **147**, 191–200 (2010).
191. Zorrilla, S., Rivas, G. & Lillo, M. P. Fluorescence anisotropy as a probe to study tracer proteins in crowded solutions. *J. Mol. Recognit.* **17**, 408–416 (2004).
192. Sabaté, R. & Saupe, S. J. Thioflavin T fluorescence anisotropy: an alternative technique for the study of amyloid aggregation. *Biochem. Biophys. Res. Commun.* **360**, 135–138 (2007).
193. Deprez, E. *et al.* Oligomeric states of the HIV-1 integrase as measured by time-resolved fluorescence anisotropy. *Biochemistry* **39**, 9275–9284 (2000).
194. Wang, Y. & Goodson, T. Early aggregation in prion peptide nanostructures investigated by nonlinear and ultrafast time-resolved fluorescence spectroscopy. *J. Phys. Chem. B* **111**, 327–330 (2007).
195. Allsop, D. *et al.* Fluorescence anisotropy: a method for early detection of Alzheimer  $\beta$ -peptide (A $\beta$ ) aggregation. *Biochem. Biophys. Res. Commun.* **285**, 58–63 (2001).
196. Jiang, B. *et al.* Monitoring the formation of amyloid oligomers using photoluminescence anisotropy. *J. Am. Chem. Soc.* **141**, 15605–15610 (2019).
197. Bataglioli, J. C. *et al.* Modification of amyloid-beta peptide aggregation via photoactivation of strained Ru (ii) polypyridyl complexes. *Chem. Sci.* (2021).
198. Ford, B. J. Brownian movement in clarkia pollen: a reprise of the first observations. *Microsc. THEN CHICAGO-* **40**, 235 (1992).

199. Einstein, A. Zur theorie der brownschen bewegung. *Ann. Phys.* **324**, 371–381 (1906).
200. Einstein, A. *Investigations on the Theory of the Brownian Movement*. (Courier Corporation, 1956).
201. Lavalette, D., Hink, M. A., Tourbez, M., Tetreau, C. & Visser, A. J. Proteins as micro viscosimeters: Brownian motion revisited. *Eur. Biophys. J.* **35**, 517–522 (2006).
202. Berg, H. C. *Random walks in biology*. (Princeton University Press, 2018).
203. Bohren, C. F. & Huffman, D. R. *Absorption and scattering of light by small particles*. (John Wiley & Sons, 2008).
204. Kubo, S. *et al.* Tunability of the refractive index of gold nanoparticle dispersions. *Nano Lett.* **7**, 3418–3423 (2007).
205. Kharat, S. N. & Mendhulkar, V. D. Synthesis, characterization and studies on antioxidant activity of silver nanoparticles using Elephantopus scaber leaf extract. *Mater. Sci. Eng. C* **62**, 719–724 (2016).
206. Gross, J., Sayle, S., Karow, A. R., Bakowsky, U. & Garidel, P. Nanoparticle tracking analysis of particle size and concentration detection in suspensions of polymer and protein samples: Influence of experimental and data evaluation parameters. *Eur. J. Pharm. Biopharm.* **104**, 30–41 (2016).
207. Powers, E. T. & Powers, D. L. Mechanisms of protein fibril formation: nucleated polymerization with competing off-pathway aggregation. *Biophys. J.* **94**, 379–391 (2008).
208. Pallitto, M. M. & Murphy, R. M. A mathematical model of the kinetics of  $\beta$ -amyloid fibril growth from the denatured state. *Biophys. J.* **81**, 1805–1822 (2001).

209. Garai, K. & Frieden, C. Quantitative analysis of the time course of A $\beta$  oligomerization and subsequent growth steps using tetramethylrhodamine-labeled A $\beta$ . *Proc. Natl. Acad. Sci.* **110**, 3321–3326 (2013).
210. Bernacki, J. P. & Murphy, R. M. Model discrimination and mechanistic interpretation of kinetic data in protein aggregation studies. *Biophys. J.* **96**, 2871–2887 (2009).
211. Fissan, H., Ristig, S., Kaminski, H., Asbach, C. & Epple, M. Comparison of different characterization methods for nanoparticle dispersions before and after aerosolization. *Anal. Methods* **6**, 7324–7334 (2014).
212. Ling, T. Y., Wang, J. & Pui, D. Y. H. Comparison of the aerosolization and nanoparticle tracking (Nanosight LM10) techniques for size and concentration measurements of colloidal suspensions and its application in determining retention of nanoparticles in liquids. in *2006 International Aerosol Conference, Sept 10–15th* Abstract Number: 1284 (2006).
213. Sanchís, J., Bosch-Orea, C., Farré, M. & Barceló, D. Nanoparticle tracking analysis characterisation and parts-per-quadrillion determination of fullerenes in river samples from Barcelona catchment area. *Anal. Bioanal. Chem.* **407**, 4261–4275 (2015).
214. Kramberger, P., Ciringer, M., Štrancar, A. & Peterka, M. Evaluation of nanoparticle tracking analysis for total virus particle determination. *Viol. J.* **9**, 1–10 (2012).
215. James, A. E. & Driskell, J. D. Monitoring gold nanoparticle conjugation and analysis of biomolecular binding with nanoparticle tracking analysis (NTA) and dynamic light scattering (DLS). *Analyst* **138**, 1212–1218 (2013).
216. Van Der Pol, E., Coumans, F. A. W., Sturk, A., Nieuwland, R. & van Leeuwen, T. G. Refractive index determination of nanoparticles in suspension using nanoparticle

- tracking analysis. *Nano Lett.* **14**, 6195–6201 (2014).
217. Dragovic, R. A. *et al.* Sizing and phenotyping of cellular vesicles using Nanoparticle Tracking Analysis. *Nanomedicine Nanotechnology, Biol. Med.* **7**, 780–788 (2011).
218. Yang, D. T., Lu, X., Fan, Y. & Murphy, R. M. Evaluation of nanoparticle tracking for characterization of fibrillar protein aggregates. *AIChE J.* **60**, 1236–1244 (2014).
219. Philo, J. S. A critical review of methods for size characterization of non-particulate protein aggregates. *Curr. Pharm. Biotechnol.* **10**, 359–372 (2009).
220. Henderson, R. K. *et al.* A  $192 \times 128$  Time Correlated SPAD Image Sensor in 40-nm CMOS Technology. *IEEE J. Solid-State Circuits* **54**, 1907–1916 (2019).
221. NIH, 2016. Healthy Brain and Severe AD Brain [Online]. USA. Available from: <https://www.flickr.com/photos/132318516@N08/24239522109> [Accessed 6 August 2021].
222. OpenClipart-Vector, n.d. Axon Brain Cell [Online]. Available from: <https://pixabay.com/vectors/axon-brain-cell-dendrites-nerve-1294021/> [Accessed 13 September 2021].